

**REACTIVITY AND STABILITY OF PLATINUM AND PLATINUM ALLOY
CATALYSTS TOWARD THE OXYGEN REDUCTION REACTION**

A Dissertation

by

SERGIO RAFAEL CALVO

Submitted to the Office of Graduate Studies of
Texas A&M University
in partial fulfillment of the requirements for the degree of

DOCTOR OF PHILOSOPHY

December 2007

Major Subject: Chemical Engineering

**REACTIVITY AND STABILITY OF PLATINUM AND PLATINUM ALLOY
CATALYSTS TOWARD THE OXYGEN REDUCTION REACTION**

A Dissertation

by

SERGIO RAFAEL CALVO

Submitted to the Office of Graduate Studies of
Texas A&M University
in partial fulfillment of the requirements for the degree of

DOCTOR OF PHILOSOPHY

Approved by:

Chair of Committee,	Perla B. Balbuena
Committee Members,	Tahir Cagin
	D. Wayne Goodman
	Victor Ugaz
Head of Department,	Michael Pishko

December 2007

Major Subject: Chemical Engineering

ABSTRACT

Reactivity and Stability of Platinum and Platinum Alloy Catalysts Toward the Oxygen Reduction Reaction. (December 2007)

Sergio Rafael Calvo, B.S., Universidad Nacional de Ingenieria

Chair of Advisory Committee: Dr. Perla B. Balbuena

Density functional theory (DFT) is used to study the reactivity of Pt and Pt-M (M: Pd, Co, Ni, V, and Rh) alloy catalysts towards the oxygen reduction reaction (ORR) as a function of the alloy overall composition and surface atomic distribution and compared to that on pure Pt surfaces. Reactivity is evaluated on the basis of the adsorption strength of oxygenated compounds which are intermediate species of the four-electron oxygen reduction reaction, separating the effect of the first electron-proton transfer from that of the three last electron-proton transfer steps.

It is found that most homogeneous distribution Pt_xM catalysts thermodynamically favor the dissociation of adsorbed OOH in comparison with pure Platinum and adsorb strongly O and OH due to the strong oxyphilicity of the M elements. On the other hand, in all cases skin Platinum surfaces catalysts do not favor the dissociation of adsorbed OOH and do favor the reduction of M-O and M-OH with respect to Platinum. Considering the overall pathway of the reactions to catalyze the ORR most of the skin Platinum monolayer catalysts provide more negative free energy changes and should behave at least in a similar way than Platinum in following order: Pt_3V (skin Pt) > Pt_3Co (skin Pt) > Pt_3Ni (skin Pt) > Pt > PtPd (skin) > Pt_4Rh (skin Pt) > $PtPd_3$ (skin). In all cases, the reactivity is shown to be not only sensitive to the overall composition of the catalyst, but most importantly to the surface atomic distribution.

Proposed electrochemical dissolution reactions of the catalyst atoms are also analyzed for the ORR catalysts, by computing the free energy changes of Platinum and bimetallic Pt-X (X: Co, Pd, Ni, and Rh) catalysts. It is found that Platinum is thermodynamically more stable than Pt-alloys in Pt_3Co , Pt_3Pd , Pt_3Ni and Pt_4Rh .

To my parents

ACKNOWLEDGEMENTS

First of all I would like to thank my supervisor Perla Balbuena, who gave me the opportunity to join her group. Her permanent support has been invaluable to me, and discussions with her have helped me during these years. I wish to thank many people in the group for our interesting discussions covering many subjects.

Also I would like to thank my family for their help and support during all these years. Thanks to my mother, father and sister for their encouragement and motivation, and to my girlfriend for her patience and love.

TABLE OF CONTENTS

	Page
ABSTRACT	iii
DEDICATION	iv
ACKNOWLEDGEMENTS	v
TABLE OF CONTENTS	vi
LIST OF FIGURES.....	ix
LIST OF TABLES	xii
 CHAPTER	
I INTRODUCTION	1
II COMPUTATIONAL TECHNIQUES.....	13
Introduction	13
Born-Oppenheimer Approximation	14
Pauli Principle	15
The Orbital Model	16
Variational Method for the Schrödinger Equation	16
The Hartree-Fock Method	18
Density Functional Theory (DFT)	19
Pseudopotentials.....	22
Projector Augmented Wave Pseudopotential.....	23
Periodic Density Functional Theory	25
III METHODOLOGY AND COMPUTATIONAL DETAILS	27
DFT Calculations for the Reactivity of Pt and Pt-M (M: Pd, Co, Ni, V, and Rh) Catalyst Models	27
DFT Calculations for Hydrated Metal Cations $M(H_2O)_6^{2+}$ (M: Pt, Pd, Co, Ni, and Rh).....	28
Transition State Calculations (CI-NEB Method)	29

CHAPTER	Page	
IV	CHEMICAL REACTIVITY OF PT AND PT-PD ALLOY CATALYSTS.....	30
	Introduction	30
	Lattice Constant and Slab Structures of Pt-Pd Catalysts.....	31
	Binding Energies of ORR Intermediates on Pt(111) Surfaces and Structural Characteristics.....	32
	Binding Energies and Structural Characteristics of ORR Intermediates on Pt-Pd(111) Surfaces	33
	d-Population Analysis	37
	Thermodynamic Reactivity of Pt-Pd Catalysts	39
	Correlation Between the Surface d-band Center and the ORR Intermediates	42
	Transition State Calculations of the OOH Dissociation on Pt(111) and Pt ₃ Pd(111).....	47
	Summary	50
V	CHEMICAL REACTIVITY OF PT ₃ CO, PT ₃ NI, PT ₃ V, AND PT ₄ RH ALLOY CATALYSTS	52
	Introduction	52
	Lattice Constant and Slab Structures of Pt and Pt-X Catalysts (X: Co, Ni, V, and Rh)	53
	Binding Energies of ORR Intermediates on Pt(111) and Pt-X(111) Surfaces (X: Co, Ni, V, and Rh) and Structural Characteristics	54
	d-Population Analysis	57
	Thermodynamic Reactivity of Pt, Pt ₃ Co, Pt ₃ Ni, Pt ₃ V, and Pt ₄ Rh Catalysts	59
	Correlation Between the Surface d-band Center and the ORR Intermediates	64
	Summary	67

CHAPTER	Page
VI	CHEMICAL REACTIVITY IN STEPPED PT AND PT-NI SURFACES 68
	Introduction 68
	Thermodynamic Reactivity of Pt(211) and Pt ₃ Ni (211) Catalysts 69
	Atomic Oxygen Adsorption on Pt(111), Pt(211), Pt(331), and Pt(320) 72
	Summary 74
VII	CHEMICAL STABILITY OF PT ₃ CO, PT ₃ NI, PT ₃ PD, AND PT ₄ RH ALLOY CATALYSTS 75
	Introduction 75
	Thermodynamic Trends of the Dissolution of Pt, Co, Ni, and Rh on Pt and Pt-X (X: Co, Ni, Pd, and Rh) Catalysts 77
	Thermodynamic Trends of Pt Dissolution on Pt and Pt-X (X: Co, Ni, Pd, and Rh) Catalysts 79
	Thermodynamic Trends of Pt Dissolution on Pt and Skin Pt Monolayers of Pt ₃ Co, Pt ₃ Ni, Pt ₃ Pd, and Pt ₄ Rh Catalysts 82
	Composition and Atomic Distribution Effects on Catalyst Surface Stability 85
	Summary 85
VIII	CONCLUSIONS AND RECOMMENDATIONS 87
	REFERENCES 90
	VITA 97

LIST OF FIGURES

FIGURE		Page
1.1	Schematic representation of a hydrogen-air fuel cell operation.....	2
1.2	Plot of relative Gibbs free energies (eV), $\Delta\Delta G_4/3$ vs $\Delta\Delta G_1$. The metals (M) in region A have vacant valence d orbitals and are able to more efficiently enhance thermodynamically the formation of M-OOH, whereas the valence d orbitals for the metals (M') in region B are fully occupied and the metals M' favor the reductions of M-O and M-OH. ⁽⁵⁰⁾	11
2.1	Comparison of a wavefunction in the Coulomb potential of the nucleus (dashed line) to the one in the pseudopotential (continues line). The real and the pseudo wavefunction and potentials match above a certain cutoff radius r_c	22
3.1	Extended surface approach. Left: The unit cell includes 16 metal atoms and the vacuum space. Right: Top view of the surface and a few of its periodic images.....	28
4.1	Binding energies of OOH adsorbed on Pt(111) and Pt-Pd(111) alloys (top Pt sites). OOH is adsorbed with the O atom on top of Pt atoms (the most favorable site). The inset shows the structures of OOH adsorbed on Pt(111) (top site), with Pt (blue), O (red), and H (light blue) and the adsorption of OOH on Pt ₃ Pd(111) (Pt top site). The three surfaces at the left of Pt have increasing amounts of Pd and show the strongest binding to OOH (even though adsorption is on Pt sites, see Table 4.2), whereas the four Pt-skin surfaces show reduced binding strength.....	34
4.2	Average electronic d-population on the surface and in the four-layer slab. The skin slabs are skin Pt/Pd and skin Pd/Pt respectively.....	36
4.3	Binding energies of OH adsorbed on Pt(111) and Pt-Pd(111) alloys (top sites). OH is adsorbed on Pt top sites, except in the Pd-skin surface.	36
4.4	Binding energies of atomic oxygen adsorbed on Pt(111) and Pt-Pd(111) alloys (fcc hollow sites).....	37

FIGURE	Page	
4.5	Average electronic d-population on the surface and in the four-layer slab after adsorption of OH. The skin slabs are skin Pt/Pd and skin Pd/Pt respectively.	38
4.6	Reaction free energy changes for equations 1.3-1.6 (ΔE_1 , ΔE_2 , ΔE_3 , and ΔE_4) of Pt and Pt-Pd alloy catalysts.	40
4.7	Relative free energies (eV) according to equations 1.3 and 1.6 for Pt and Pt-Pd alloys with respect to pure Pt.	42
4.8	Partial density of states of d-electrons for Pt(111). $E_{d\text{-band center}}(\text{Pt}) = -2.16$ eV.	44
4.9	Comparison of the partial density of states of d-electrons for Pd in Pt-Pd alloys. (a) Pd in PtPd ₃ ($E_{d\text{-band center}} = -1.765$ eV), (b) Pd in PtPd ($E_{d\text{-band center}} = -1.825$ eV), and (c) Pd in Pt ₃ Pd ($E_{d\text{-band center}} = -1.906$ eV)	46
4.10	Binding energies of O as a function of the surface d-band center for Pt, Pt ₃ Pd, PtPd, PtPd ₃ , skin Pt/Pd, skin Pd/Pt, skin Pt/Pt ₃ Pd, skin Pt/PtPd, and skin Pt/PtPd ₃	47
4.11	Transition state pathway for the OOH dissociation on Pt(111) (red line) and elongation distance O-O (green line).	49
4.12	Transition state pathway for the OOH dissociation on Pt ₃ Pd(111) (red line) and elongation distance O-O (green line).	50
5.1	Distribution layer by layer for top adsorption sites of OOH and OH on skin Pt monolayer of Pt ₃ Co, Pt ₃ Ni, Pt ₃ V, and Pt ₄ Rh	53
5.2	Initial (a) and final (b) structures (after optimization) for the OOH adsorption on Vanadium atom in Pt ₃ V slab.	56
5.3	Average electronic d-population on the surface and in the four-layer slab for Pt, Pt ₃ Co, Pt ₃ Ni, Pt ₃ V, and Pt ₄ Rh (cases A and B).	56
5.4	Reaction free energy changes for equations 1.3-1.6 (ΔE_1 , ΔE_2 , ΔE_3 , and ΔE_4) of Pt, Pt ₃ Co, Pt ₃ Ni, Pt ₃ V, and Pt ₄ Rh (case B) and their respective skin Pt monolayers (case A).	60

FIGURE	Page
5.5	Relative energies (eV) according to equations 1.3 and 1.6 for Pt, Pt ₃ Co, Pt ₃ Ni, Pt ₃ V, and Pt ₄ Rh alloys with respect to pure Pt. 63
5.6	Gibbs free energy profile for the ORR on Pt ₄ Rh (skin Pt). The data in parenthesis are for pure Pt 64
5.7	Binding energies of OOH, OH, and O as a function of the d-band center of the slab cluster for Pt, Pt ₃ Co, Pt ₃ Ni, Pt ₃ V, and Pt ₄ Rh (cases A and B). 66
5.8	Binding energies of OOH, OH, and O as a function of the surface d-band center of the slab cluster for Pt, Pt ₃ Co, Pt ₃ Ni, Pt ₃ V, and Pt ₄ Rh (cases A and B)..... 66
6.1	Extended surface (211) approach. Left: The unit cell includes 26 metal atoms and the vacuum space. Right: Lateral view of the surface. 1: step site, 2 and 3: terrace sites. 70
6.2	Binding energies (in eV) of atomic oxygen on Pt(111), Pt(211), Pt(331), and Pt(320) surfaces tested in different positions along the steeped surface. 73
6.3	Adsorption of atomic oxygen on Pt(211), Pt(320), and Pt(331) surfaces..... 74
7.1	Relative free energies of reactions 7.1-7.5 with respect to Pt for the dissolution of Pt, Co, Ni, Pd, Rh atoms from the model catalyst surfaces of pure Pt, Pt ₃ Co, Pt ₃ Ni, Pt ₃ Pd, and Pt ₄ Rh..... 79
7.2	Relative free energies with respect to Pt for reactions 7.1-7.5 for the dissolution of Pt atoms from the catalyst surfaces of pure Pt and Pt monolayers of Pt ₃ Co, Pt ₃ Ni, Pt ₃ Pd, and Pt ₄ Rh 82
7.3	Relative free energies changes for reactions 7.1-7.5 for the dissolution of Pt atoms from the catalyst surface with respect to Pt in pure Pt and Pt skin monolayer of Pt ₃ Co, Pt ₃ Ni, Pt ₃ Pd, and Pt ₄ Rh model catalyst surfaces 84

LIST OF TABLES

TABLE	Page	
1.1	Summary of electrolyte materials, operating temperature, fuel (transported ion), advantages and disadvantages of common fuel cell types.	3
4.1	Calculated lattice constant (\AA) for Pt and Pt-Pd alloys, their atomic composition in the 4-layer slab, the interlayer separation between the first two layers (Δ_{12}), and the percent of change of such interlayer separation after relaxation with respect to the bulk conformation.	32
4.2	Binding energies (in eV) of OOH, OH, and O on various sites of the Pt ₃ Pd, PtPd, and PtPd ₃ surfaces	33
4.3	Structural characteristics of adsorption of oxygenated species on Pt and Pt-Pd alloys. O is adsorbed in fcc hollow sites, and the interactions with Pd atoms are indicated in bold font. Distances are in \AA	35
4.4	Changes in d-electron population after adsorption of OOH, OH, and O, defined as percents with respect to the population found in the naked surface. In each group, Δ_{surf} is the change on the surface, and Δ_{slab} is the change per atom averaged for the total slab. Largest changes indicate significant depletion of the d population and are shown in bold font.	39
4.5	Slab and surface d-band center ordered with respect to the surface d-band center	45
5.1	Lattice constants and slab layer by layer distribution for Pt, Pt ₃ Co, Pt ₃ Ni, Pt ₃ V, and Pt ₄ Rh. The Pt:M layer by layer distribution is indicated starting from the surface composition.....	54
5.2	Binding energies (BE, in eV) of OOH, OH, and O on Pt, Pt ₃ Co, Pt ₃ Ni, Pt ₃ V, and Pt ₄ Rh surfaces. BEs calculated as: $BE_{\text{slab-adsorbate}} = E_{\text{slab+adsorbate}} - E_{\text{slab}} - E_{\text{adsorbate}}$. Interactions with either Co or Ni or V or Rh are indicated in bold font	57

TABLE	Page	
5.3	Structural characteristics of the adsorption of oxygenated species on Pt, Pt ₃ Co, Pt ₃ Ni, Pt ₃ V, and Pt ₄ Rh. Atomic oxygen is adsorbed on fcc hollow sites while hydroxyl and OOH adsorb on top sites. Interactions with either Co or Ni or V or Rh are indicated in bold font	58
5.4	Surface relaxation estimated as changes from bulk separation between the first two layers Δ_{12}	59
5.5	Relative free energies (eV) according to equations 1.3 and 1.6 for Pt, Pt ₃ Co, Pt ₃ Ni, Pt ₃ V, and Pt ₄ Rh alloys with respect to pure Pt.....	62
6.1	Binding energies (BE, in eV) of OOH, OH, and O on Pt and Pt/Pt ₃ Ni. BEs calculated as: $BE_{\text{slab-adsorbate}} = E_{\text{slab+adsorbate}} - E_{\text{slab}} - E_{\text{adsorbate}}$	71
6.2	Relative free energies (eV) according to equations 1.3 and 1.6 for Pt and Pt/Pt ₃ Ni with respect to pure Pt.	72
6.3	Distances (in Å) for adsorption of oxygenated species on Pt and Pt/Pt ₃ Ni(211). Atomic oxygen, hydroxyl and OOH adsorbed on bridge sites.....	72
7.1	Free energy changes ΔE (eV) for Pt, Co, Ni, Pd, and Rh dissolution in Pt, Pt ₃ Co, Pt ₃ Ni, Pt ₃ Pd and Pt ₄ Rh surface catalysts for reactions 7.1-7.5.....	77
7.2	Free energy changes (eV) for Pt dissolution in Pt, Pt ₃ Co, Pt ₃ Ni, Pt ₃ Pd and Pt ₄ Rh catalysts for reactions 7.1-7.5.....	80
7.3	Free energy changes (eV) for Pt dissolution in Pt, skin Pt/Pt ₃ Co, skin Pt/Pt ₃ Ni, skin Pt/Pt ₃ Pd, and skin Pt/Pt ₄ Rh catalysts for reactions 7.1-7.5.	83

CHAPTER I

INTRODUCTION

In the last decades a necessity to reduce and eradicate high levels of contamination in the environment has raised the development of the so-called clean technologies. Among these alternative technologies fuel cells have emerged as promising alternative sources of energy that can eventually replace the use of internal combustion engines. Fuel cells operate on the basis of electrochemical reactions that convert chemical energy coming from fuels such as hydrogen, methanol, gasoline, etc. into electricity. Fuel cells today are certainly much more than simple curiosities of laboratories, and although they still need some improvements in the selection of the materials and design for practical operation, they constitute a real alternative for the replacement of internal combustion engines. That is the reason why the automobile industry and the energetic sector have shown interest in their development in the last decades.

In 1839 Sir William Grove who is known as “father of the Fuel Cell” undertook a series of experiments discovering the possibility of the production of electric current from electrochemical reactions of hydrogen and oxygen. However, he also raised questions about the production of heat and "novel gaseous and liquid products", questions that he could not answer with the equipment and theory available to him. These questions became puzzles for later researchers to solve. Grove verified that the oxidation of hydrogen in the negative electrode (anode) combined with the reduction of oxygen in the positive electrode (cathode) generate electric current. The experiments of Grove showed the inter-convertibility between the chemical energy from a fuel and the electric energy, without going through an intermediate process of combustion, which involve a low efficient mechanism that converts thermal energy into mechanical energy. In fuel cells the chemical energy of the fuel is converted directly to electric current and

This dissertation follows the style of Surface Science

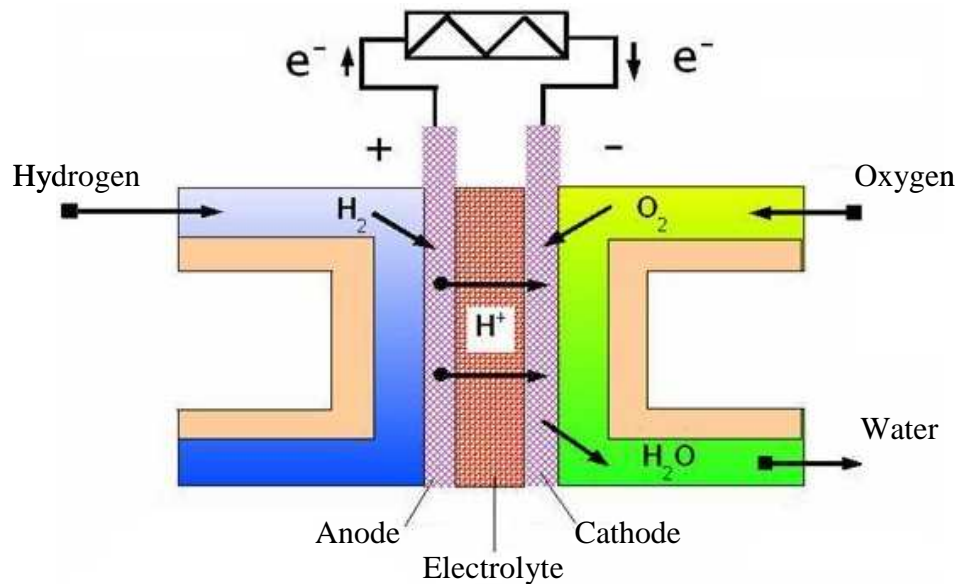


Figure 1.1. Schematic representation of a hydrogen-air fuel cell operation

the efficiency can reach values in the order of 60 to 70%.

Figure 1.1 shows a schematic representation of a hydrogen-air fuel cell operation. This device is conceptually simple; an individual fuel cell is constituted by two electrodes that are separated by an electrolyte. This electrolyte allows the flow of ions but not electrons. In the negative electrode (anode) the oxidation of the fuel takes place; the fuel can be hydrogen, methanol or gasoline and in the positive electrode (cathode) the reduction of the oxygen from the air takes place. The overall reaction is given by: $O_2 + 4e^- + 4H^+ \leftrightarrow 2H_2O$. The H^+ ions migrate through the electrolyte while the electrons (e^-) flow from the anode to the cathode through an external circuit. Each of these cells generates a voltage close to one volt; for applications that require more voltage a series of fuel cells is stacked.

There are different types of fuel cells; they are usually characterized by their electrolyte, operating temperature, transported ion and fuel. Table 1.1 lists a summary of the most important characteristics of different types of fuel cells.

Table 1.1

Summary of electrolyte materials, operating temperature, fuel (transported ion), advantages and disadvantages of common fuel cell types

Fuel Cell Type	Electrolyte	Operating temperature	Fuel (Ion)	Advantages	Disadvantages
Polymer electrolyte membrane fuel cell (PEMFC)	Cation conducting polymer membrane	60 – 100 °C	H ₂ (H ⁺)	Low temperature, solid electrolyte and low corrosion	Require expensive catalyst and pure H ₂
Direct methanol fuel cell (DMFC)	Cation conducting polymer membrane	60 – 100 °C	CH ₃ OH (H ⁺)	Liquid fuel	Poor fuel utilization
Phosphoric acid fuel cell (PAFC)	Molten phosphoric acid (H ₃ PO ₄)	175 – 200 °C	H ₂ (H ⁺)	High efficiency (85%), impure H ₂ can be used	Low electric current and high size and weight
Alkaline fuel cell (AFC)	Aqueous alkaline solution (e.g. KOH)	90 – 100 °C	H ₂ (OH ⁻)	Fast cathode reaction	CO ₂ emissions and fuel
Molten carbonate fuel cell (MCFC)	Molten alkaline carbonate (e.g. NaHCO ₃)	600 – 1000 °C	H ₂ (CO ₃ ²⁻)	Advantages related to the high temperature	corrosion
Solid oxide fuel cell (SOFC)	O ²⁻ conducting ceramic oxide (e.g. Y ₂ O ₃ -stabilized ZrO ₂)	800 – 1000 °C	H ₂ (O ²⁻)	Solid electrolyte reduce corrosion	Hard to operate due to high temperature

Among all types of fuel cells, the PEMFC is the most advanced for applications, but there are still issues to be solved before the PEM fuel cells can successfully compete with conventional technologies. Probably the most important outstanding technological challenge is the slow kinetics in the cathode reactions, and catalysts durability and lifetime, which have not yet been solved completely. Furthermore, the current price of both catalysts and the electrolyte materials are too high for competitiveness with conventional technologies.

Due to its importance, a large amount of experimental ^[1-10] and theoretical ^[11-18] work has been reported in recent years, however because of its complexity the complete understanding of the reaction mechanism remains unclear. Alloy catalysts have been proposed and tested with various degrees of success. For example, it has been demonstrated that the use of alloys such as Pt-Pd, Pt-Fe, Pt-Ni, Pt-Co, and Pt-Cr leads to an enhancement in the activity of the oxygen reduction on the fuel cell cathode compared with pure platinum. ^[2-4; 19-22] Stamenkovic et al. ^[23] evaluated the ORR on polycrystalline Pt₃Ni and Pt₃Co alloys in acid electrolytes using the rotating disk electrode (RRDE) method. They found that in the temperature range of 293 < T < 333 K the activity increases in the order of: Pt₃Ni > Pt₃Co > Pt. Catalytic enhancement of Pt₃Ni and Pt₃Co vs. Pt is attributed to the inhibition of Pt-OH_{ad} formation on Pt sites surrounded by oxide covered Ni and Co atoms beyond 0.8 V.

Additional information were collected in studies of ORR activity using electrode catalysts that do not contain Pt., Min-Hua Shao et al. ^[24] found that Pd-Fe alloy nanoparticles have a very high ORR activity. Similar results were reported for Pd-Co ^[25] and Pd-Co-Au ^[26] catalysts. A relationship has been found between the electrocatalytic activity and the Pd-Pd bond distances, which is related to the electronic structure through changes in the orbital overlap that alter the d-band center, thus determining surface reactivity. They observed an interesting correlation between the current density at 0.85 V and the Pd-Pd distances. A higher activity was found for a 2.73Å Pd-Pd bond distance, which corresponds to Pt₃Pd. It is also pointed out that the value of the Pd-Pd distance for any of the used composition highly depends on the method used in the catalyst

preparation. Myoung-ki Min et al. ^[27] also investigated the origin of the enhanced activity of the ORR using Pt-based binary alloys of Pt₃Co, Pt₃Cr, and Pt₃Ni. According to cyclic voltammetry and X-ray adsorption near-edge structure (XANES) analyses, the electrocatalytic activity was related to the adsorption strength of the oxygen intermediates on the Pt surface, which is apparently favored by reduced Pt-Pt bond distances. It was also found that Pt-based alloy catalysts showed significantly higher specific activities than Pt catalyst with the same surface area.

In general, most of the studies ^[28-32] indicate that the enhancement of the electrocatalytic activity for the ORR on Pt-Co and Pt-Ni alloys may be attributed to the modification of the electronic structure, which is reflected on the increase of the 5d orbital vacancies, changes in the physical structure of Pt (Pt-Pt bond distance and coordination number), and on the adsorption strength of oxygen-containing species from the electrolyte onto Pt or the alloying element. Toda et al. ^[33] on the other hand, show some disagreement with the previous cited statements related to the ORR enhancement in some bimetallic alloys. They found an enhancement of the electrocatalytic activity of Pt by alloying with Fe. It was observed a maximum activity at ca. 50% Fe content (25 times higher activity than pure Pt). They also observed the formation of a skin Pt surface in the bulk catalyst (< 1nm in thickness). These results showed some discrepancy with other works. For example, Jalan and Taylor ^[34] claimed that the enhancement of the Pt catalytic activity is due to the reaction results from the shortening of Pt-Pt distances. In the same way Appleby ^[35] shows a volcano type behavior in the relationship between the electrocatalytic activity and the adsorbed bond length. The lattice contraction due to alloying was shown to result in more favorable Pt-Pt distances for the dissociative adsorption of molecular oxygen, while maintaining the favorable electronic properties of Pt. Mukerjee and Srinivasan ^[31] supported the view of favorable Pt-Pt distances, but found no electronic structure changes on binary alloys in PEFCs. Toda suggests the enhancement in terms of the 5d-vacancy of the surface, but not by the interatomic distance or roughening of the surfaces. The increased d-vacancy of the Pt in the electrode surface, brought about by alloying, must bring about a strong metal-oxygen

interaction. Such strong interaction will cause an increase of the adsorbed O^{2-} , a weakening of the O-O bond and an increase in its length, resulting in fast bond scission and/ or a new bond formation between the O atom and H^+ in the electrolyte.

In order to achieve a better understanding of the ORR, results from experiments must be also interpreted with thermodynamic principles analyses. Fernandez et al. ^[26] proposed guidelines for the design of bimetallic catalysts for the oxygen reduction reaction (ORR) in acid media. Assuming that the ORR starts with an initial dissociative chemisorption ^[36] (equation 1.1); involving the splitting of the O-O bond to form adsorbed oxygen atoms, followed by the four electron reduction of the metal oxide to water (equation 1.2),



They reported the standard potential for reaction (1.2) versus the Gibbs free energy for reaction (1.2). From this analysis, it is inferred that metals that favor the bond cleavage of molecular oxygen, stabilize the metal oxide. And from tabulated data [37; 38] of the free Gibbs energy of the formation of metal oxide versus the standard potential for the reduction of metal oxide to water, metals that form less stable M-O bonds are easier to reduce to water. It is proposed to couple a good oxygen bond cleaving metal (M) with a second metal (M') that adsorbs atomic oxygen weakly so this can be easily to reduce to water. It is also pointed out that since most of the metal oxide with lower Gibbs free energy for reaction (1.1) and standard potential for reaction (1.2) dissolve rapidly in acidic solutions, especially in the presence of molecular oxygen, they should be alloyed into a stable phase to avoid dissolution under real conditions. Another point to have in mind is the metal miscibility because some of them are not miscible under normal conditions.

Besides important insights about the ORR from experimental works, the complete understanding is not yet available due to the complexity of this process. In recent years the use of computational chemistry has raised as an alternative tool to

explain and analyze the complex thermodynamic of the surface reaction catalysts, especially on Pt and Pt-based bimetallic catalysts. At the same time, these theoretical publications have been successfully supported by experiments. ^[12; 13; 15; 21; 22; 39]

Xu et al. ^[18] correlated the atomic and molecular binding energies on Pt₃Co, Pt₃Ni, Skin Pt on Pt₃Co, and Skin Pt on Pt₃Fe and the activation energy differences of the dissociation of molecular oxygen and the formation of hydroxyl finding that weaker atomic adsorption on the catalyst surface facilitates the O-H bond formation but makes the O-O bond breaking more difficult. They also correlated the binding energies of atomic oxygen with the d-band center. They proposed that an alleviation of poisoning by O and enhanced rates of reactions involving O may be some of the reasons why Pt skins are more active for the ORR in low temperature fuel cells. Minhua Shao et al. ^[40] also showed a volcano type dependence between the measured ORR activity of Pt or Pd monolayers supported on many different noble metal single crystals and their calculated d-band center and the atomic oxygen binding energy using DFT calculations.

The continuous search for more active and less expensive ORR catalyst than Pt also includes the search for more stable Pt alloy catalysts. Although metals such as Pt, Pd, Rh, Co, and Ni have been extensively used as electrodes for the ORR, few investigations have been directed to analyze the dissolution of these metals in acid medium. Recent investigations ^{[41] [9; 33; 42; 43]} have found that Pt and other important metal alloys are not completely inert in non-complexing acids. This process is not also affected by the concentration of the active species, the agitation of the electrolyte and the electrolyte temperature but also the applying potential which lead to passivation and repassivation of the electrodes. The dissolution of the metal electrode is also expected to be accompanied by changes in the surface morphology and composition.

It was found that in wet cells after the catalysts have been briefly immersed in an acid electrolyte, a skin consisting of a monolayer of pure Pt forms on the surface of the Pt alloys. These results indicate the dissolution of the metal from the cathode catalyst during the cell operation. Recent studies on the catalytic activity and stability of supported Pt-Co alloys with well-defined structures by Watanabe et al. ^[41]

demonstrated that both Co and Pt dissolve out preferentially from small-size alloy particles and Pt re-deposits on the surfaces of large-size ones in hot H_3PO_4 . As a result, an alloy with a disordered crystallite structure, which is more corrosion-resistant than an ordered one, maintains higher electrocatalytic activity for a longer time due to the active alloy surfaces with a relatively large surface area. It was also found that a fine Pt alloy catalyst is covered with a pure Pt skin under the practical operation conditions in PEMFCs^[41]. Thus, it is important to examine the electronic-structure changes of alloy surfaces during the catalytic life as a possible factor for the enhancement in combination with the surface composition.

Therefore, although the mechanism of the ORR has been the main topic to researches debating how the oxygen adsorption and dissociation takes place in the catalyst, and how the use of Pt alloys can change and enhance the activity of the ORR, there is also a new question that is raised regarding the stability of the catalyst in the presence of the electrolyte. Over time, fuel cell performance decreases, and it is believed that this is because the platinum dissolves away, resulting in a decrease of the electrochemically active surface area of the catalyst^[42] which reduces the performance of the fuel cell. It was observed that the surface area initially increases until it reaches a maximum value due to the initial wetting of the thin Nafion layer covering the catalyst particles in polymer electrolyte polymer fuel cell (PEMFC), but after saturation of the active material with the electrolyte, the surface area starts to decrease.

It is also known that after the catalyst is immerse in the acid electrolyte, a skin Pt monolayer is formed^[9; 33; 42; 43] under practical operation conditions even in dilute acid solutions. This theory proved that Pt alloys on the surface most likely dissolve in the presence of the acid electrolyte. And even after some hours of operation, the Pt surface is also dissolved in the presence of the electrolyte. It is believed that platinum oxidizes and dissolves at high potentials often encountered at the cathode; such a process would be exacerbated with repeated cycling between high and low cathode potentials, which leads to platinum oxidation and reduction, respectively. The dissolved platinum then either deposits on existing platinum particles to form larger particles or diffuses into an

electrochemically inaccessible portion of the membrane-electrode assembly or its support structure. As we can see the stability and the dissolution of Pt and Pt alloys of the catalyst play an important role for the application to practical fuel cells.

Respect to the ORR mechanism, it is generally accepted that depending on the experimental conditions, the oxygen reduction reaction takes place through two overall pathways: the series two-electron reduction to peroxide, followed by its decomposition, and the direct four-electron reduction to water ^[44]. It has been postulated that the two electron reduction is caused by the availability of only one atom site, and on the other hand in the four electron reduction the oxygen atoms are bonded to the surface forming di- σ structure ^[45].

Wang and Balbuena ^[12] studied the reaction thermodynamics of the ORR using theoretical methods. Based on ab-initio molecular dynamics ^[46], they suggested an alternative reaction pathway for the ORR on Pt(111). They proposed a parallel pathway, where the direct and the series occurring simultaneously, with the direct as a dominant step. In agreement with Damjanovic ^[47] and Anderson ^[48; 49], the proton transfer participates in the first step simultaneously with the electron transfer. The product of this step is OOH, which dissociates with a small barrier compared to the dissociation of O-O as it has been previously suggested ^[12; 13]. Tsuda and Kasai also supported this idea; they found that the activation barrier for the proton transfer in the $\text{CF}_3\text{SO}_3\text{-Pt}_2\text{-O}_2 + \text{H}$ system (0.105 eV and 0.051 eV for the singlet and the triplet respectively) are lower than those in the $\text{CF}_3\text{SO}_3\text{-Pt}_2\text{-O} + \text{H}$ system (0.239 eV and 0.187 eV for the singlet and the triplet respectively). The trifluoro-methane sulfonate ion (CF_3SO_3^-) represents the physical properties of the active site of the Nafion chain ^[50-55]. These results indicated that the protonation tends to be followed by the molecular oxygen dissociation, resulting in H_2O production via a hydroperoxo (-OOH) species. Considering the high activation barrier for the O_2 dissociation, which it is been found to be high in both experimental ^[56] (0.38 eV) and theoretical studies ^[48; 57; 58] (this value changes depending on the size of the cluster and on the adsorption sites: 0.74, ~0.9, and ~1.7 eV) and the lower activation barrier for the OOH dissociation, we can consider that the protonation tends to occur

before the molecular oxygen dissociation, which is promoted by the formation of M-OOH.

Using this analysis and based on the work of Wang and Balbuena^[59], which indicated that it is possible to separate the effect of the first reduction step from that of the last three reduction steps (last three electron-proton transfers) and might be considered coupled; they proposed that a good ORR catalyst could be designed as a combination of a metal M that adsorbs OOH stronger than Pt plus a second metal M' able to bind OH and O less stronger than Pt, thus can be easily reduced to water. Figure 1.2 shows the ability of various metals to thermodynamically favor the formation of M-OOH ($\Delta\Delta G_1 < 0$) and the reduction of OH and the O ($\Delta\Delta G_4 < 0$).

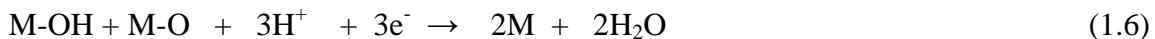
In this work we study the changes in reaction energy (at 0 K) for the parallel pathway, evaluating ΔE_1 (equation 1.3), ΔE_2 (equation 1.4), and ΔE_3 (equation 1.5) for the first electron reduction step on a given metal site M as:



The reaction for the first electron and proton reduction becomes



And the last three electron reduction steps evaluating ΔE_4 (equation 1.6):



which combines the last three electron and proton transfers representing successive reductions of the adsorbed hydroxyl and the atomic oxygen resulting from the dissociation of the OOH intermediate to water molecules.

Although the characterization of surface atomic distribution in alloy nanoparticles is still far from being solved, recent theoretical and experimental studies

have yielded some interesting information ^[60]. In these work we explore the surface catalyst distribution in terms of segregation and stability.

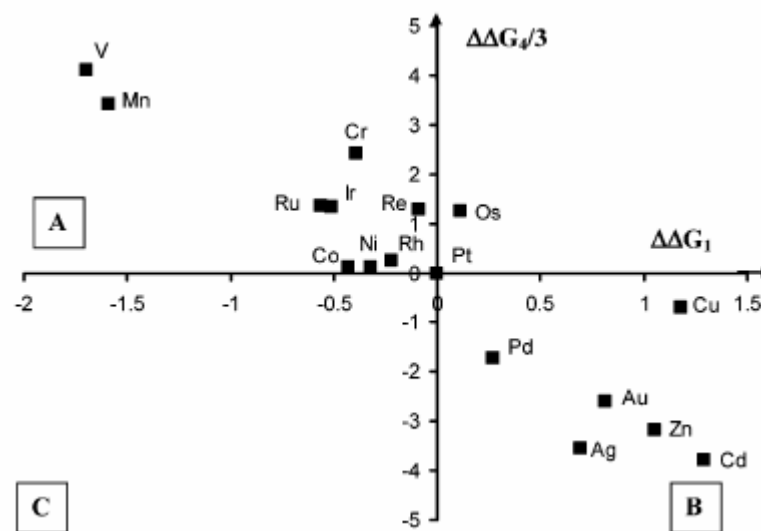


Figure 1.2. Plot of relative Gibbs free energies (eV), $\Delta\Delta G_4/3$ vs $\Delta\Delta G_1$. The metals (M) in region A have vacant valence d orbitals and are able to more efficiently enhance thermodynamically the formation of M-OOH, whereas the valence d orbitals for the metals (M') in region B are fully occupied and the metals M' favor the reductions of M-O and M-OH. ^[59]

It is emphasized that the nature of the environment used in this study corresponds to a solid-gas interaction, which differs from the electrochemical environment (solid-liquid) under which the cathode catalyst operates in a fuel cell. However, as it has been shown by a large number of computational studies the general trend provided by these approximations offers important insights useful to analyze ORR real operational conditions ^[24; 46; 48; 59; 61].

In the first part of this dissertation, we analyze the reactivity of Pt and Pt-Pd catalysts. We use a variety of compositions and atomic distributions to evaluate the reactivity of the ORR in terms of reaction thermodynamics. In the second part, we explore the reactivity of Pt₃Co, Pt₃Ni, Pt₃V, and Pt₄Rh catalysts using two different distributions (homogeneous and Pt skin monolayer catalysts). In addition, a comparison of surfaces (111) and (211) in terms of reactivity toward the ORR is performed for Pt and Pt₃Ni. In the last part we analyze the electrochemical stability of the Pt₃Co, Pt₃Ni, Pt₃V, and Pt₄Rh alloy catalysts against the dissolution in acidic environment measuring the free energy changes of allowed dissolution reactions.

CHAPTER II

COMPUTATIONAL TECHNIQUES

Introduction

Since the mid 1980's, computational chemistry has been one of the fastest growing areas of chemistry and engineering. One of the reasons for the fast development is the vast increase in the number of computing platforms and the development of efficient high performance computational algorithms. It has already been accepted that high-quality of theoretical data is not just an addition to experimental findings, but it is a reliable, independent source of information about molecular structures, properties, and reactivity. In this section, an overview of the basic theories, models, and approximations involved is given. The theoretical frameworks of Hartree-Fock (HF) theory and density functional theory (DFT) are presented as approximate methods to solve the many-electron problem, a variety of ways to incorporate electron correlation are discussed. Emphasis is also given to the application of these techniques to calculate thermodynamic and spectroscopic properties in chemical systems. This tool will be used to explain the catalyst reactivity and stability toward the oxygen reduction reaction.

Let us start with the most important restriction in this study, since we will be dealing with isolated clusters and extended surfaces, which do not interact with the environment in any way, these systems must have their energy conserved; therefore their energies and electron distributions are independent of time. This important restriction enables us to remove all time dependence from the Schrödinger equation leaving the wave function with only a trivial time dependence which is usually ignored. So, we start with the time independent Schrödinger equation that is given by:

$$H \cdot \Psi = E \cdot \Psi \quad (2.1)$$

Where H is the Hamiltonian operator, Ψ is the wave function and E is the energy of the system. In the next sections we introduce some of the assumptions and approximations needed to deal with the solution of the time independent Schrödinger equation.

Born-Oppenheimer Approximation

A good approximation of the electronic structure can be obtained with all the nuclei fixed in space. This is an essence the Born-Oppenheimer approximation^[62], which allows the degrees of freedom of the electrons to be treated separately from those of the ions. Its justification resides on the fact that the nuclei are much heavier than the electrons (the mass of the proton or a neutron is about 1835 times as large as the electron mass). So it is intuitively clear that the nuclei move much more slowly than the electrons. The later will then be able to adapt themselves to the current configuration of the nuclei. This approach results also from formal calculations, and leads to a Hamiltonian for the electrons in the field generated by a static configuration of the nuclei, and a separate Schrödinger equation for the nuclei in which the electronic energy enters as a potential. The Born-Oppenheimer approximation for electrons is given by:

$$H_{\text{BO}} = \sum_{i=1}^N \frac{p_i^2}{2m} + \frac{1}{4\pi\epsilon_0} \cdot \frac{1}{2} \sum_{i,j=1;i \neq j}^N \frac{e^2}{|\mathbf{r}_i - \mathbf{r}_j|} - \frac{1}{4\pi\epsilon_0} \sum_{n=1}^K \sum_{i=1}^N \frac{Z_n e^2}{|\mathbf{r}_i - \mathbf{R}_n|} \quad (2.2)$$

where the first term corresponds to the kinetic energy of the system, the second term represents the electron interactions, and the third term represents the interaction between the nuclei and the electrons. The total energy is given by the sum of the energy of the electrons and the energy resulting from the Schrödinger equation satisfied by the nuclei. With this approximation, the motion of the nuclei is neglected and only the electrostatic energy of the nuclei should be added to the energy of the electrons to arrive at the total energy. The positions of the nuclei can be varied in order to find the minimum of this energy, that is, the ground state of the whole system. In this procedure the nuclei is

treated on a classical footing since their ground state is determined as the minimum of their potential energy, neglecting quantum fluctuations^[63].

Even with the position of the nuclei fixed, the problem of solving the Schrödinger equation of the electronic wave function using the Hamiltonian remains intractable, even in a computer, since too many degrees of freedom are involved. The second term, which contains the interactions between the electrons, makes the problem so difficult.

Pauli Principle

Perhaps the most important constrain that we must place on the solution of the time-independent Schrödinger equation is that due to the consequences of the fact that the electrons are all the same; the wave function of a many-electron system must reflect the fact that electrons are indistinguishable. It can be also stated in other words that an acceptable wave function for many electrons must be antisymmetric with respect to the exchange of coordinates of any two electrons, which is perhaps the most general statement of the Pauli Principle for electrons. The relevance of the Pauli principle to the computation of molecular electronic structures is enormous. The complications brought about by the antisymmetric requirement itself look trivial at first sight, however the real complications arise when we consider what is meant by the “coordinate” of the electrons. We have not included anything about the description of the electrons to account for electron “spin” in previous correlations, and since there is no mention of electron spin in the Hamiltonian the spin should have as little relevance to the energy of the system as any other coordinate which does not occur in the Hamiltonian. However, the Pauli principle applies to exchange of all the coordinates of an electron; space and spin. So, in order to comply with the Pauli principle in full we have to bring formally the electron spin into the theory^[63].

The Orbital Model

There are just few one-particle systems for which the Schrödinger equation is completely soluble. The ones of greatest chemical interest are the hydrogen-like atom and the harmonic oscillator. Assuming that we have access to the set of all solutions of the one electron Schrödinger equation we have:

$$\hat{h}\phi_i = \varepsilon_i\phi_i \quad (2.3)$$

Mathematically, these solutions are the eigenvalues ε_i and the eigenfunctions ϕ_i of the Hermitian operator \hat{h} and, as such, they have several important properties. One of these properties is that they are complete; any function of ordinary three-space with sufficiently similar boundary conditions can be expanded as a linear combination of these functions. That is any function $f(\vec{r})$ can be written exactly as

$$f(\vec{r}) = \sum_{i=1}^{\infty} c_i \phi_i(\vec{r}) \quad (2.4)$$

This is a very powerful result since it means, in principle, that any one-electron Schrödinger equation may be solve by evaluating a set of numerical coefficients; that is a partial differential equation may be replaced by an ordinary, algebraic equation ^[63].

Variational Method for the Schrödinger Equation

The time independent Schrödinger equation can be solved analytically in a very restricted number of cases; examples include the free particle, the harmonic oscillator and the hydrogen atom. In most cases we must resort to computers to determine the solution to this equation. The variational method enables us to solve the Schrödinger equation much more in efficiently in many cases. In the variational method, the possible solutions are restricted to a subspace of the Hilbert space, and in this subspace the best solution is found. This method allows us to approximate the ground state energy of a system without solving the Schrödinger equation. It also can be extended to estimate the energy of the excited states. To see how this works, we first show that the stationary Schrödinger equation can be derived by a stationary condition of the functional:

$$E[\psi] = \frac{\langle \psi | H | \psi \rangle}{\langle \psi | \psi \rangle} \quad (2.5)$$

which is recognized as the expectation value of the energy for a stationary state ψ . The stationary state of this energy functional is defined by postulating that if such a state is changed by an arbitrary but small amount $\delta\psi$, the corresponding change in E vanishes to first order.

A special kind of variation function widely used in the study of molecules is the linear variation function. A linear variation function is a linear combination of n linearly independent functions f_1, f_2, \dots, f_n .

$$\phi = \sum_{j=1}^n c_j f_j \quad (2.6)$$

where ϕ is the trial variation function and the coefficients c_j are the parameters to be determined by minimizing the variational integral. The basis functions f_j must satisfy the boundary conditions of the problem. We shall restrict ourselves to real ϕ so that the c_j 's and f_j 's are all real.

Applying the variational theorem for the linear variation function, we have

$$\int \phi^* \phi \cdot d\tau = \sum_{j,k=1}^n c_j c_k \cdot S_{jk} \quad , \text{ where the overlap integral } S_{jk} \text{ is defined as} \quad (2.7)$$

$$S_{jk} \equiv \int f_j^* f_k \cdot d\tau \quad \text{and,} \quad (2.8)$$

$$\int \phi^* \hat{H} \cdot \phi \cdot d\tau = \sum_{j,k=1}^n c_j c_k \cdot H_{jk} \quad \text{where,} \quad (2.9)$$

$$H_{jk} = \int f_j^* \hat{H} \cdot f_k \quad (2.10)$$

The stationary states follow from the condition that the derivative of this functional with respect to the c_k vanishes, which leads to

$$\sum_{j=1}^N (H_{kj} - E\delta_{kj})C_j = 0 \quad \text{for } k = 1, \dots, n. \quad (2.11)$$

An extended derivation of this method can be found in Levine's book ^[64].

The Hartree-Fock Method

The Hartree-Fock (HF) method can be viewed as a variational method in which the wave functions of the many-electron system have the form of an anti-symmetrized product of one electron wave function. This restriction leads to an effective Schrödinger equation for the individual one-electron wave functions (orbitals) with a potential determined by the orbitals occupied by the other electrons. This coupling between the orbitals via the potentials causing the resulting equations to become nonlinear in the orbitals, and the solution must be found iteratively in a self-consistency procedure.

We shall see that in this variational approach, correlations between electrons are neglected to some extent. In particular, the coulomb repulsion between the electrons is represented in an averaged way. However, the effective interaction caused by the fact that the electrons are fermions, obeying Pauli's principle, and hence want to keep apart if they have the same spin, is accurately included in the HF approach (there exist several methods which improve on the approximation made in the HF method). The HF equation is given by:

$$F\Psi_k = \varepsilon_k \Psi_k \quad \text{with} \quad (2.13)$$

$$F\Psi_k = \left[-\frac{1}{2}\nabla^2 - \sum_n \frac{Z_n}{|\mathbf{r} - \mathbf{R}_n|} \right] \Psi_k(x) + \sum_{l=1}^N \int dx' |\Psi_l(x')|^2 \frac{1}{|\mathbf{r} - \mathbf{r}'|} \Psi_k(x) - \sum_{l=1}^N \int dx' \Psi_l^*(x') \frac{1}{|\mathbf{r} - \mathbf{r}'|} \Psi_k(x') \Psi_l(x) \quad (2.14)$$

The operator F is called the Fock operator. The first term represents the kinetic energy of the electrons, the second term represents the Coulomb attraction potential of the nucleus, and the third term is the Coulomb energy of the particle resulting from a charge distribution caused by all the electrons. The fourth term is the same as the third, with two spin-orbital labels k and l interchanged and a minus sign in front as a resulting from the antisymmetry of the wave function – it is called the exchange term. Note that this term is nonlocal: it is an operator acting on Ψ_k , but its value at \mathbf{r} is determined by the value assumed by Ψ_k at all possible position \mathbf{r}' .

A subtlety is that the eigenvalues \mathcal{E}_k of Fock operator are not the energies of single electron orbitals, although they are related to the total energy by

$$E = \frac{1}{2} \sum_k [\mathcal{E}_k + \langle \Psi_k | h | \Psi_k \rangle] \quad (2.15)$$

It is clear that equation 2.14 is a nonlinear equation, which must be solved by a self-consistency iterative procedure. The self-consistent procedure is carried out as follow. Solving equation 2.14 yields an infinite spectrum. To find the ground state, we must take the lowest N eigenstates of this spectrum as the spin-orbitals of the electrons. These are Ψ_l eigenfunctions which are then used to build the new Fock operator which is diagonalized again and the procedure is repeated over and over until convergence is achieved. Extended derivations of HF method are given in detail in Cook's ^[63] and Thijssen's books ^[65].

Density Functional Theory (DFT)

Most electronic calculations for solids are based on density functional theory (DFT), which results from the work of Hohenberg, Kohn, and Sham ^[66; 67]. This approach has also become popular for atoms and molecules. In the density functional theory, the electronic orbitals are solutions to a Schrödinger equation which depends on the electronic density rather than on the individual electron orbitals.

$$\rho(r) = n \int dr_1 \cdot dr_2 \cdot dr_3 \dots dr_{n-1} |\Psi(r, r_1, r_2, \dots, r_{n-1})|^2 \quad (2.16)$$

The electronic density ρ is a much simpler quantity than Ψ because it depends on one spatial coordinate only. For a while it was not obvious how to relate the ground state energy of the electrons to the electronic density. This issue has been elucidated by theorem due to Hohenberg and Kohn^[66]. The theorem states that the ground state energy of a system of interacting electrons subject to an external local potential $V(r)$ is a unique functional of the electron density.

In density functional theory, an effective independent particle Hamiltonian is arrived at, leading to the following Schrödinger equation for one-electron spin Orbital:

$$\left[-\frac{1}{2}\nabla^2 - \sum_n \frac{Z_n}{|r - R_n|} + \int d^3r' n(r') \frac{1}{|r - r'|} + V_{xc}[\rho](r) \right] \Psi_k(r) = \epsilon_k \Psi_k(r) \quad (2.17)$$

The first three terms in the left hand side of this equation are exactly the same as those of Hartree-Fock equation (2.14), namely the kinetic energy, the electrostatic interaction between the electrons and the nuclei, and the electrostatic energy of the electron in the field generated by the total electron density $\rho(r)$. The fourth term contains the many-body effects, lumped together in an exchange correlation potential. The main result of the density functional theory is that there exists a form of this potential, depending only on the electronic density $\rho(r)$, which yields the exact ground state energy and density.

A substantial step forward to make the DFT approach useful for practical calculations was made by Kohn and Sham^[67]. These authors introduce the concept of fictitious non-interacting electrons having the same density of the true interacting electrons. Non-interacting electrons are described by orthonormal single-particle wavefunctions and their density is given by:

$$\rho(r) = \sum_k^n |\Psi_k(\mathbf{r})|^2 \quad (2.18)$$

The total energy of a many-electron system is given by

$$E = \sum_{k=1}^n \epsilon_k - \frac{1}{2} \int d^3r \cdot d^3r' \rho(\mathbf{r}) \frac{1}{|\mathbf{r} - \mathbf{r}'|} \rho(\mathbf{r}') + E_{xc}[\rho] - \int d^3r \cdot V_{xc}[\rho](\mathbf{r}) \rho(\mathbf{r}) \quad (2.19)$$

where the parameters \mathcal{E}_k are the eigenvalues occurring in equation (2.17) and the E_{xc} is the exchange correlation energy. The exchange correlation potential $V_{xc}[\rho]$ which occurs in equation (2.17) is the functional derivative of this energy with respect to the density:

$$V_{xc}[\rho](\mathbf{r}) = \frac{\delta}{\delta n(\mathbf{r})} E_{xc}[\rho] \quad (2.20)$$

The E_{xc} describes all many-body effects differences between the real system and the effective non-interacting system. It contains an exchange energy contribution as well as a correlation distribution to the kinetic and potential energy of the electrons. In order to specify the E_{xc} , an approximation is needed. The basic approximation is the local density approximation (LDA). In the LDA we assume instead that it depends only on the density at point r itself (it becomes a local functional). The LDA often predicts structural and vibrational properties of molecules and solids with surprising accuracy. Typical errors are 1-2 percent in bond lengths and 5-10 percent in vibrational frequencies. It tends, however to overestimate cohesive energies of solids and the atomization energies of molecules (even by 20 percent and more). A turning point for the success of DFT has been the development of the generalized gradient approximation (GGA). This approximation allows the E_{xc} to depend not only on the local electronic density, as in the LDA, but also on the local electronic density gradient. It is possible to construct the GGA functional in a non-empirical way. This is achieved in the parameterization of Perdew, Burke and Enzerhoff (PBE) ^[68], which is today one of the widely used GGA functionals. The GGA improved substantially over the LDA, particularly for the cohesive properties and atomization energies. Extended derivations of the DFT method are given in detail in Cook's ^[63] and Thijssen's books ^[65].

In summary, DFT calculations require solution of the Kohn-Sham equations. If the single particle Kohn-Sham orbitals are expanded in a finite basis, these amounts can be reduced to a self-consistent diagonalization problem.

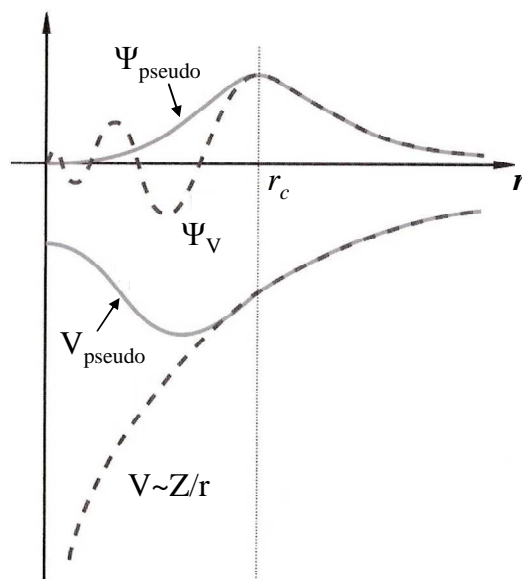


Figure 2.1. Comparison of a wavefunction in the Coulomb potential of the nucleus (dashed line) to the one in the pseudopotential (continuous line). The real and the pseudo wavefunction and potentials match above a certain cutoff radius r_c .

Pseudopotentials

For practical uses of the DFT approach, it is realized that only valence electrons are important for chemical bonding. Freezing core electrons in the state corresponding to a reference atomic configuration usually does not affect significantly the calculated binding properties. A powerful approach to implement this idea is provided by pseudopotential theory. In this formalism, originally developed in the context of solid state physics, the external potential is replaced by an external pseudopotential (see Figure 2.1). This is an effective potential acting on the valence electrons only. The pseudo-wavefunctions have the same Kohn-Sham eigenvalues of their all-electron counterparts. In the core region pseudo and all-electron-wavefunctions differ, notably the pseudo-wavefunctions are smoother than their all-electron counterparts because they are nodeless and do not exhibit the fast oscillations due to orthogonality to the core states. An interesting discussion of pseudopotentials for DFT and Ab-initio molecular

dynamic methods is offered by Car ^[69]. Pseudopotentials constructed according the above procedure are called norm-conserving pseudopotentials ^[70] and have optimal transferability properties. It must be noticed that pseudopotentials are uniquely defined only outside the core region. The error introduced by the pseudopotential is usually smaller than the error due to the GGA. Nodeless pseudo-wavefunctions can be conveniently expanded in plane waves. This corresponds to the adsorption of periodic boundary conditions. For a finite system like a molecule, it means that the molecule is placed in a periodically repeated cell. The supercell has to be large enough that the wavefunction of the occupied molecular state be essentially zero at the cell boundary.

Projector Augmented Wave Pseudopotential

Projector Augmented Wave (PAW) approaches has established itself as one of the most efficient and widely used tools for performing ab-initio density functional calculations. It was pointed out by Blochl ^[71] that a true wavefunction Ψ , and a well behaving pseudo-wavefunction $\tilde{\Psi}$ can be linked by a linear transformation $\Psi = T \tilde{\Psi}$, by which physical quantities like $\langle \Psi | A | \Psi \rangle$ can be easily calculated in the pseudo Hilbert space representation, rather than directly from true wavefunctions.

Similarly, the variational principle for the total energy gives an equivalent of the Kohn-Sham equation for the pseudo-wavefunctions, and the search for the ground state can be also done in the pseudo Hilbert space. This latter, due to the slowly varying character of the pseudo-wavefunctions can be efficiently spanned by the plane wave expansion. However, contrary to the norm-conserving pseudopotential, the pseudo-wavefunctions are directly shadowing the true crystal wavefunctions by means of the T transformation ^[72].

As it can be expected, T mainly concerns the regions of the atomic cores. In the interstitial regions, where the true crystal wave function varies slowly Ψ , $\tilde{\Psi}$ may practically be built to coincide with Ψ . As a consequence, T can be seen as a sum of

non-overlapping atom-centered contributions T_R , each of them acting within the corresponding augmentation region, such that

$$T = 1 + \sum_R T_R \quad (2.21)$$

In the following points we focus on the practical construction of the operator T_R . Inside each atomic sphere, both the true and the pseudo-wavefunctions can be represented as linear combinations of (true and pseudo) partial waves:

$$\tilde{\Psi} = \sum_i c_i \tilde{\psi}_i \quad \text{and} \quad \Psi = \sum_i c_i \psi_i = T \tilde{\Psi} \quad (2.22)$$

Where, since $\psi_i = T \tilde{\psi}_i$, the coefficients c_i are the same in both the expansions. As a consequence:

$$\Psi = \tilde{\Psi} + \sum_i c_i (\psi_i - \tilde{\psi}_i) \quad (2.23)$$

And the transformation T can be written as:

$$T = 1 + \sum_i (\psi_i - \tilde{\psi}_i) \langle \tilde{p} | \quad (2.24)$$

In the above expression we have introduced the set of projector function $\langle \tilde{p} |$, which verify the condition:

$$\tilde{\Psi} = \sum_i c_i \tilde{\psi}_i = \sum_i \langle \tilde{p} | \tilde{\Psi} \rangle \tilde{\psi}_i \quad (2.25)$$

Each augmentation region is associated to two sets of partial waves and a set of projector functions. The set of the all-electron partial waves Ψ_l can be generated from numerical solutions of the radial Schrödinger equation. They can be chosen to describe the physically relevant states (valence band and semi-core states), and their number per l channel can be increased up to the desired convergence of results. Additionally, the divergent tail of the true partial wave cancels with that of the corresponding pseudo partial wave, so that there is no constrain to the bound states only. Since the pseudo

partial waves $\tilde{\Psi}_l$ are supposed to be slowly oscillating, they can be in principle generated by the techniques used in the pseudopotential approach.

Different practical schemes can be used to generate the set of projector functions \tilde{p} . The Gram–Schmidt inspired scheme by Blochl ^[71] seems particularly well adapted for numerical implementation, assuring that the all electron and the pseudo wave partial waves form complete sets of functions within the augmentation region.

Periodic Density Functional Theory

The conservation of the crystal momentum \mathbf{k} follows from the periodicity of the one-particle Hamiltonian ^[73], according to Bloch's theorem. \mathbf{k} is therefore a good quantum number for the electronic wavefunctions, with the following property:

$$\psi_{mk}(\mathbf{r} + \mathbf{L}) = e^{i\mathbf{k} \cdot \mathbf{L}} \psi_{mk}(\mathbf{r}) \quad (2.26)$$

Where \mathbf{L} is the lattice vector. For the normalization of the wavefunctions, the Born-Von Karman (BvK) cyclic boundary conditions are used:

$$\psi_{mk}(\mathbf{r} + N_i \mathbf{a}_i) = \psi_{mk}(\mathbf{r}) \quad (2.27)$$

m and k label the band and the wave-vector, respectively, while three \mathbf{a}_i vectors form a basis of the real space lattice, and the three corresponding N_i are large numbers, that should tend to infinity. Wavefunctions are normalized to one in the BvK supercell. Because of the BvK conditions, the number of \mathbf{k} wave-vectors in the Brillion zone (BZ) is equal to $N = N_1 N_2 N_3$, and their density is $\Omega_0 / (2\pi)^3$, where Ω_0 is the primitive unit cell volume.

The Bloch wavefunctions can be decomposed in a product of a phase factor by a function u_{mk} having the crystal periodicity $u_{mk}(\mathbf{r} + \mathbf{L}) = u_{mk}(\mathbf{r})$:

$$\psi_{mk}(r) = (N \cdot \Omega_0)^{-1/2} e^{ik \cdot r} u_{mk}(r) \quad (2.28)$$

The periodic part u_{mk} of a Bloch wavefunction is normalized to one in the primitive cell. This periodic part of the Bloch function can be expanded in terms of plane waves as follow:

$$u_{mk}(r) = \sum_G e^{-iG \cdot r} u_{mk}(G) \quad (2.29)$$

Where the sum runs over all vectors G of reciprocal lattice. The coefficients $u_{mk}(G)$ are the Fourier transform of $u_{mk}(r)$:

$$u_{mk}(G) = \frac{1}{\Omega_0} \int_{\Omega_0} e^{-iG \cdot r} u_{mk}(r) dr \quad (2.30)$$

The expansion of (3)(2.28) is easily truncated, to provide a finite basis set; one can select wave-vectors such that

$$\frac{\hbar^2 |k + G|^2}{2m} < E_{cut} \quad (2.31)$$

E_{cut} is the maximum kinetic energy of the plane waves and is usually called cutoff energy. The larger cutoff energy, the more accurate the wavefunction representation. (Gonze and Finocchi^[72] provide detailed explanations of this derivation).

CHAPTER III

METHODOLOGY AND COMPUTATIONAL DETAILS

DFT Calculations for the Reactivity of Pt and Pt-M (M: Pd, Co, Ni, V, and Rh) Catalyst Models

All the calculations were performed within the framework of DFT using the Vienna Ab initio Simulation package (VASP)^[74-77], which is a DFT code based on plane wave basis sets. Electron-ion interactions are described using the projector-augmented wave (PAW) method^[78], which was expanded within a plane wave basis set up to a cutoff energy of 400 eV. Electron exchange and correlation effects were described by Perdew-Burke-Ernzerhof (PBE)^[79] GGA type exchange correlation functional; spin polarization was included in all the simulations.

The Pt(111) and the Pt-M(111) catalyst systems were described using a 4-layer periodic slab model, where each slab was infinite in the x and y directions, while finite along the z direction, and then repeated periodically along all the directions. The optimum bulk lattice constant was determined for each case and then used for a model four-layer slab, in which the first two layers on the top are allowed to relax, while the two at the bottom are fixed (Figure 3.1). A vacuum space equivalent to 19 layers was used to ensure that there were no interaction between the adsorbed intermediates and the bottom surface of the next slab. The (111) surfaces were modeled using a 2x2 supercell. Brillouin zone integration was performed using 5x5x1 Monkhorst Pack grid^[80] and a Methfessel-Paxton^[81] smearing of 0.2 eV. All the adsorption sites used to evaluate the interaction between the ORR intermediates OOH, OH, and O and the surface were those found as the most stable sites using an overall coverage of ¼ monolayer (ML). For OOH and OH the most stable are the surface top sites, and for atomic oxygen both fcc and hcp hollow sites are studied, with fcc being the most stable.

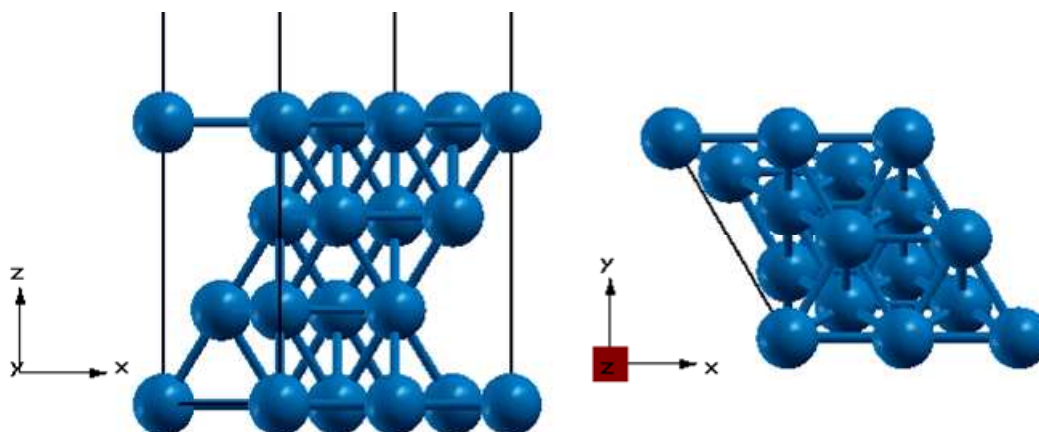


Figure 3.1. Extended surface approach. Left: The unit cell includes 16 metal atoms and the vacuum space. Right: Top view of the surface and a few of its periodic images. (All the schematic representations in this work were performed using Xcrysden^[89; 90]).

DFT Calculations for Hydrated Metal Cations $M(\text{H}_2\text{O})_6^{2+}$ (M: Pt, Pd, Co, Ni, and Rh)

For the complex molecules, the calculations were performed with the same VASP framework using a simple cubic supercell of 20 Å length. This length is sufficiently big to isolate the system from their supercell image^[82]. VASP handles the charged system by applying a background charge to maintain the charge neutrality, and by adding dipole, and quadrupole corrections^[83; 84]. Balamurugan and Prasad^[85] reported that VASP calculated total energies and structures of positive charged systems using a big supercell provide good accuracy, while negatively charged systems do not provide the same accuracy in terms of energy values and structures compared to results performed in real space from Gaussian^[86]. In the negatively charged cluster, the uppermost electron is highly diffuse in nature; therefore negative clusters require even a larger supercell. For protons the inner shell may be conceived as the three water molecules solvating H_3O^+ ^[87; 88] (the H_3O^+ ion itself is similar in diameter to K^+ and both have similar solvation

energies). The hydrated metal cation (M^{2+}) is modeled as $M(H_2O)_6^{2+}$ because six-coordinate complexes of transition metals are commonly formed.

Transition State Calculations (CI-NEB Method)

Transition state calculations have been performed using the climbing image nudged elastic band (CI-NEB) method^[91]. This method constitutes a small modification of the NEB method, in which the information of the minimum energy pathway (MEP) is retained, and a rigorous convergence of the saddle point is also obtained. Qualitatively the climbing image moves up to the potential energy surface along the elastic band and down the potential surface perpendicular to the band. The other images in the band serve the purpose of defining the one degree of freedom for which a maximization of the energy is carried out. Since the images in the band eventually converge to the MEP, they give a good approximation to the reaction coordinate around the saddle point. The CI-NEB method refines an accurate pathway and finds the diffusion barrier. At the same time this method guarantees that the image with the highest energy converges to the saddle point^[91-93].

All the calculations in this section are performed using the VASP package^[74-77]. Electron-ion interactions are described using the PAW method^[78], which was expanded within a plane wave basis set up to a cutoff energy of 400 eV. Electron exchange and correlation effects were described by Perdew-Burke-Ernzerhof (PBE)^[79] GGA type exchange correlation functional, and the Brillouin zone integration was performed using 5x5x1 Monkhorst Pack grid^[80]. An initial relaxation of the reactants (OOH) and products (OH and O) initiates a full relaxation of seven images along the path, keeping the volume of the cell fixed. The seven images are initialized by linear interpolation between the two relaxed end points.

CHAPTER IV

CHEMICAL REACTIVITY OF PT AND PT-PD ALLOY CATALYSTS

Introduction

Commonly platinum catalysts are used in anodes and cathodes to promote the electrochemical reactions that generate electrical energy. Alloy catalysts have emerged as potential candidates of more active and less expensive catalytic materials.^[23; 24; 94-96] There have been many attempts to elucidate the factors affecting the catalytic activity toward the ORR, but there is still some debate about the reasons for the enhanced reactivity of certain alloy combinations. Previous results suggest that the enhancement is related to changes in the electronic structure with respect to that of Pt and to changes of the physical structure of the catalyst (metal-metal catalyst distances and coordination numbers). The continued search to overcome the slow kinetics of the ORR even with the use pure Pt catalyst has led to the use of Pt alloys, which has been demonstrated to reduce the poisoning effect caused by the OH adsorption and to produce an improvement in the activity of the ORR. Norskov et al.^[97] predicts a volcano-shaped relationship between the oxygen reduction activity of Fe, Mo, W, Co, Ru, Ni, Rh, Cu, Ir, Pd, Ag, Pt, and Au and the adsorption energies of OH and O using DFT calculations. From the results it was observed that Pt and Pd are the best catalysts for the ORR in agreement with experiments^[98; 99]. Considering this fact, in previous work^[100] we evaluated the free energy changes corresponding to the first and the last three electron-proton transfer reactions (equations 1.3-1.6) to evaluate the performance of various Pt-Pd combinations in small clusters of 10 atoms. The calculations indicated that two different ensembles: one ordered and one randomly mixed, with overall composition Pt₃Pd₇ are thermodynamically more favorable than pure Pt₁₀ for the oxygen reduction reaction. The reasons for this behavior are clearly explained in terms of the atomic and electronic distribution, which makes the Pd atoms to act as electron donors to Pt atoms and to the adsorbates, thus having intermediate reactivity between Pt and Pd. Moreover, it is found that in the mixed Pt₃Pd₇ state the electronic distribution makes the average atom more

similar to Pt than to Pd, whereas in the ordered Pt₃Pd₇ cluster, the average atom is more similar to Pd than to Pt.

In this Chapter extended Pt-Pd surfaces are evaluated exploring the overall composition of the catalyst and the surface atomic distribution, comparing the results with previous results found for small clusters. We use nine different periodic slabs: Pt, Pt₃Pd, PtPd, PtPd₃, skin Pt/Pd, skin Pd/Pt, skin Pt/Pt₃Pd, skin Pt/PtPd, and skin Pt/PtPd₃. We define the skin surface as one pure component monolayer over the periodic slab, which differs from the overall composition of the substrate.

Lattice Constant and Slab Structures of Pt-Pd Catalysts

The value of the lattice constant may play an important role on the ORR reactivity considering experimental evidence that shows that alloying Pt with Fe ^[1], Co ^[1; 5], Ni ^[5; 39], and Cr ^[5] results in enhanced catalytic activities possibly associated with a lowering of the lattice parameters and reduction of the Pt-Pt bond distances, with the consequent modification of the surface electronic properties caused by charge and atomic redistribution on the surface. Similar studies have been made for Pd-Fe alloys ^[20], showing a comparable relation between the Pd-Pd bond distances and the ORR activity. Others report the same trend for trimetallic systems such as Pd-Co-Au alloy nanoparticles ^[6].

Table 4.1 lists the optimum lattice constant for nine different Pt-Pd alloys and that for pure Pt. The calculated total energy of bulk platinum shows a minimum at 3.98 Å lattice constant, which is 1.45% higher than the experimental value (3.923 Å) ^[101]. Table 4.1 illustrates that alloying Pt with Pd results in lowering the lattice constant and hence the Pt-Pt bond distances. The highest computed lattice constant corresponds to pure Pt, while the smallest lattice constant of this group corresponds to the case with the highest composition of Pd in the PtPd₃ alloy. In all cases, the optimized structures reveal a contraction of the interlayer distance between the first two layers after relaxation with respect to the bulk conformation; such contractions are approximately proportional to the amount of Pt in the alloy.

Table 4.1

Calculated lattice constant (\AA) for Pt and Pt-Pd alloys, their atomic composition in the 4-layer slab, the interlayer separation between the first two layers (Δ_{12}), and the percent of change of such interlayer separation after relaxation with respect to the bulk conformation

Bulk system	Lattice constant (\AA)	% Pt	Pt:Pd layer by layer distribution	Separation Δ_{12} (\AA)	% Change
Pt	3.98	100	4:0 4:0 4:0 4:0	2.38	-1.81
Skin Pt/Pt ₃ Pd	3.97	81	4:0 3:1 3:1 3:1	2.37	-1.57
Skin Pd/Pt	3.96	75	0:4 4:0 4:0 4:0	2.34	-1.87
Skin Pt/PtPd	3.96	63	4:0 2:2 2:2 2:2	2.36	-1.05
Pt ₃ Pd	3.96	75	3:1 3:1 3:1 3:1	2.37	-1.05
PtPd	3.95	50	2:2 2:2 2:2 2:2	2.35	-0.61
Skin Pt/PtPd ₃	3.95	44	4:0 1:3 1:3 1:3	2.36	-0.54
Skin Pt/Pd	3.95	25	4:0 0:4 0:4 0:4	2.36	-0.57
PtPd ₃	3.94	25	1:3 1:3 1:3 1:3	2.34	-0.39

Binding Energies of ORR Intermediates on Pt(111) Surfaces and Structural Characteristics

In this section we compare our results corresponding to adsorption on pure Pt surfaces with published data. It is found that the fcc hollow is the most stable site for the adsorption of atomic oxygen with a binding energy of -3.92 eV/O , which is close to both theoretical -3.88 eV/O [18] and experimental results -3.60 eV/O [102; 103], while the hcp hollow is less stable (-3.52 eV/O). Panchenko et al. [104] report Pt-O distances of the O atom to its first metal neighbors in the fcc hollow site of 2.04 \AA each and on the hcp hollow sites 2.06 \AA each, which compare well with our values of 2.04 \AA and 2.05 \AA for fcc and hcp hollow sites respectively. OH, one of the key intermediates in the ORR, at low coverage adsorbs on top site with a binding energy of -2.27 eV/OH . This value is in

agreement with previous reports of -2.25 eV/OH^[105] and -2.23 eV/OH^[104]. The binding energy for OOH adsorbed on top site is -1.085 eV and the Pt-O and O-O distances are 2.04 and 1.43 Å, compared to reported values of binding energy of -1.07 eV and distances of 2.03 and 1.45 Å for Pt-O and O-O respectively^[104].

Binding Energies and Structural Characteristics of ORR Intermediates on Pt-Pd(111) Surfaces

Most of the surfaces in this study have either Pt or Pd surface sites exclusively (skin monolayer catalyst cases), except for Pt₃Pd, PtPd, and PtPd₃; in those cases we have found an interesting binding behavior of the oxygenated species. Table 4.2 shows that both OOH and OH bind stronger to Pt than to Pd top sites on the three surfaces, which could be attributed to the oxidation of Pd donating electrons to their neighbor Pt atoms. The difference in binding energies between Pt and Pd sites are between 0.3 and 0.4 eV, suggesting a clear preference of the adsorbates for the Pt sites in these surfaces. For O adsorption, the Pt-Pt-Pd fcc hollow site shows stronger adsorption than the equivalent in the Pt(111) surface. To test the accuracy of our results, we evaluated the adsorption of the three adsorbates to a pure Pd(111) surface. The results are -1.019 eV for OOH (top site), -2.221 eV for OH (top site), and -4.196 eV for O adsorbed in the fcc hollow site of Pd(111), versus -1.085 eV for OOH (top site), -2.271 eV for OH (top site) and -3.922 eV for O (fcc hollow) in the Pt (111) surface. Similar results were reported recently by Karlberg^[14] based on DFT calculations.

Table 4.2

Binding energies (in eV) of OOH, OH, and O on various sites of the Pt₃Pd, PtPd, and PtPd₃ surfaces

Adsorbate	Pt ₃ Pd		PtPd		PtPd ₃	
OOH	-1.073 (Pt top)	-0.740 (Pd top)	-1.188 (Pt top)	-0.830 (Pd top)	-1.206 (Pt top)	-0.903 (Pd top)
OH	-2.371 (Pt top)	-1.954 (Pd top)	-2.45 (Pt top)	-2.077 (Pd top)	-2.506 (Pt top)	-2.120 (Pd top)
O	-4.055 (Pt, Pt, Pd hollow site)		-4.200 (Pt, Pt, Pd hollow site)		-4.203 (Pt, Pd, Pd hollow site)	

As it is shown in equation 1.3, the OOH adsorption is directly related to the first electron reduction step coupled to a proton transfer. It has been proposed ^[12] that a good ORR catalyst could be designed as the combination of a metal that adsorbs OOH stronger than Pt, and a second metal able to bind OH and O less strong than Pt, thus favoring O and OH reduction to water. Figure 4.1 shows the binding energies of OOH on Pt and Pt-Pd alloys. It is found that alloys such as PtPd₃, PtPd and skin Pd/Pt satisfy the first criterion, adsorbing OOH strongly on Pt sites, whereas Pt₃Pd yields very similar binding energies than pure Pt. Thus, increasing the amount of Pd atoms present on the surface makes the adsorption of OOH stronger, as in PtPd₃, even though the adsorption is on the Pt sites. Regarding the monolayer skin Pt surfaces, the presence of Pd atoms in the substrate *reduces* the interaction strength between OOH and the surface Pt atoms.

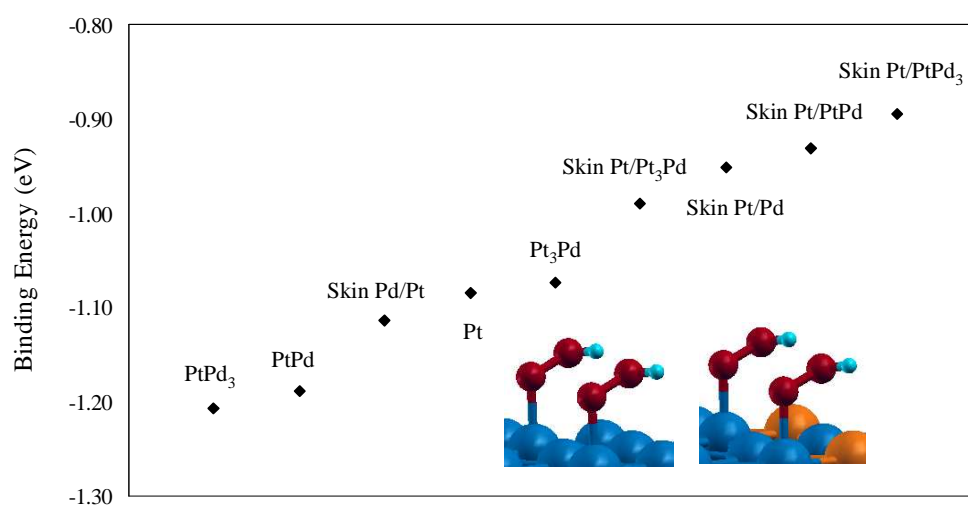


Figure 4.1. Binding energies of OOH adsorbed on Pt(111) and Pt-Pd(111) alloys (top Pt sites). OOH is adsorbed with the O atom on top of Pt atoms (the most favorable site). The inset shows the structures of OOH adsorbed on Pt(111) (top site), with Pt (blue), O (red), and H (light blue) and the adsorption of OOH on Pt₃Pd(111) (Pt top site). The three surfaces at the left of Pt have increasing amounts of Pd and show the strongest binding to OOH (even though adsorption is on Pt sites, see Table 4.2), whereas the four Pt-skin surfaces show reduced binding strength.

The O-O bond length for the OOH top site adsorption -its most stable conformation on Pt- is 1.43 Å (Table 4.3). Surfaces with stronger OOH adsorption, such as PtPd and PtPd₃, show elongated bond lengths of 1.48 Å and 1.47 Å respectively, thus signaling the dissociation of OOH into OH and O. The d-electron distribution averaged on the surface and in the slab (not shown) after adsorption of OOH is qualitatively similar to that of the naked surface (Figure 4.2). The geometric adsorption features of the intermediates are listed in Table 4.2.

Table 4.3

Structural characteristics of adsorption of oxygenated species on Pt and Pt-Pd alloys. O is adsorbed in fcc hollow sites, and the interactions with Pd atoms are indicated in bold font. Distances are in Å

	M-OOH d _{O-O}	M-OOH d _{M-O}	M-OH d _{M-O}	M-O d _{M-O fcc}	M-O d _{M-O hcp}
Pt	1.430	2.037	2.002	2.042	2.055
Skin Pd/Pt	1.462	2.025	1.987	2.007	2.019
Skin Pt/Pd	1.424	2.024	1.991	2.03	2.041
Skin Pt/Pt ₃ Pd	1.425	2.019	1.993	2.038 2.042 2.042	2.053
Skin Pt/PtPd	1.427	2.031	1.999	2.043 2.027 2.027	2.043 2.043 2.058
Skin Pt/PtPd ₃	1.429	2.032	1.993	2.030 2.031 2.033	2.045
Pt ₃ Pd	1.440	2.011	1.993	2.010 2.012 2.080	2.012 2.011 2.125
PtPd	1.475	2.010	1.993	1.998 1.998 2.081	2.006 2.006 2.109
PtPd ₃	1.471	2.006	2.000	1.972 2.035 2.036	1.970 2.055 2.058

Figure 4.3 shows the most favorable binding energies of OH on Pt and the alloys. It is observed that skin Pt/PtPd₃, skin Pt/PtPd, and skin Pt/Pd favor the reduction of OH, allowing a weaker interaction of OH with the surface compared with pure Pt, as we had observed in Figure 4.2 for the interaction with OOH. Thus, the three most favorable surfaces for OH *reduction* yield binding energies of -2.179, -2.221, and -2.225 eV respectively, whereas the binding energy for Pt is -2.271 eV. Note that the best Pt-skin surface catalysts for reducing OH are those containing $\geq 50\%$ Pd in the substrate.

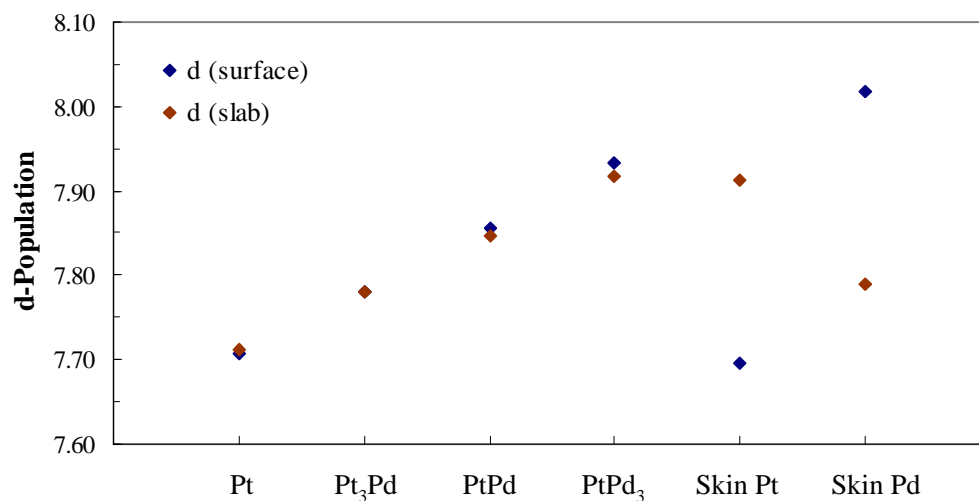


Figure 4.2. Average electronic d-population on the surface and in the four-layer slab. The skin slabs are skin Pt/Pd and skin Pd/Pt respectively.

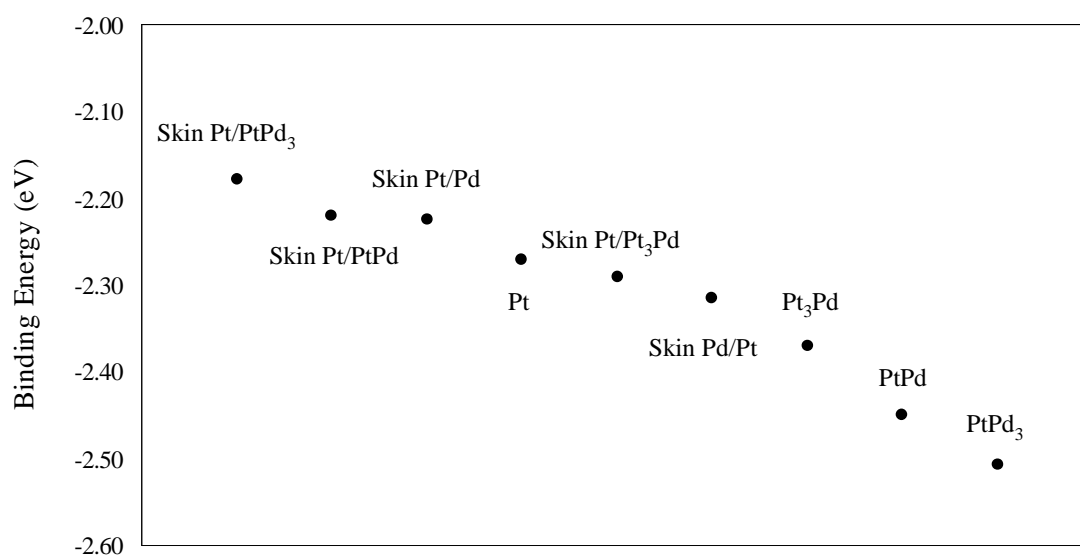


Figure 4.3. Binding energies of OH adsorbed on Pt(111) and Pt-Pd(111) alloys (top sites). OH is adsorbed on Pt top sites, except in the Pd-skin surface.

The last three electron transfer steps (represented by equation 1.6) are controlled not only by adsorption of the hydroxyl radical but also by that of atomic oxygen, and it is found that in *all cases* except skin Pt/PtPd, atomic oxygen adsorbs stronger on the alloy surfaces than on Pt, as shown in Figure 4.4. Thus, based on our second criteria we can state that only skin Pt/PtPd favors *both* the reduction of atomic oxygen having less strong interaction with the catalyst (-3.905 eV) compared with pure Pt (-3.922 eV), and the OH reduction because of its weaker (-2.221 eV) adsorption compared to that of Pt (-2.271 eV).

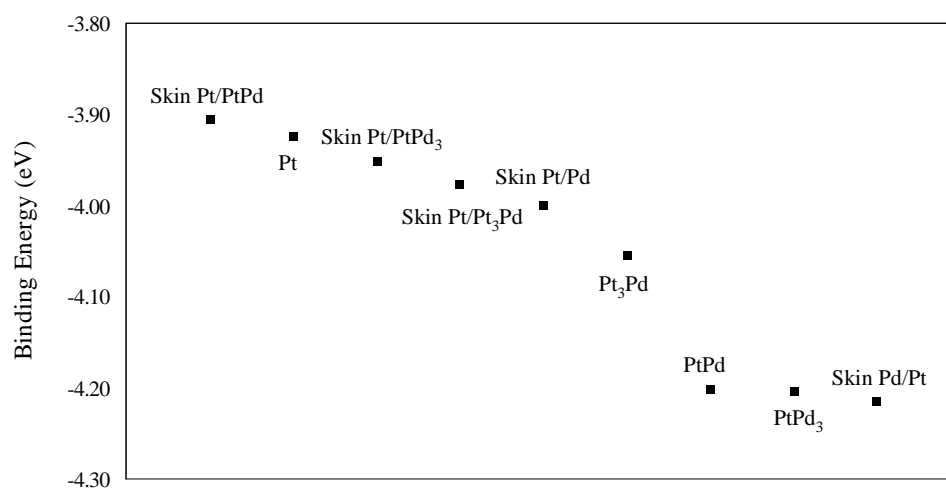


Figure 4.4. Binding energies of atomic oxygen adsorbed on Pt(111) and Pt-Pd(111) alloys (fcc hollow sites).

d-Population Analysis

The d-electron population shown in Figure 4.5 for the OH adsorption case reveals a significant change in the surface d population after adsorption of OH on Pd of the Pt₃Pd surface, in comparison to the values shown in Figure 4.2 for the naked surface. Changes in that average population defined as percents with respect to the population existent in the naked surface are listed in Table 4.4. In all cases, changes in the surface after adsorption are negative, indicating a charge transfer, with the largest changes found

for OH and O. Note also that the electron transfer may occur not only to the adsorbate but also to the subsurface layers as shown by a positive value of Δ_{slab} in Table 4.4.

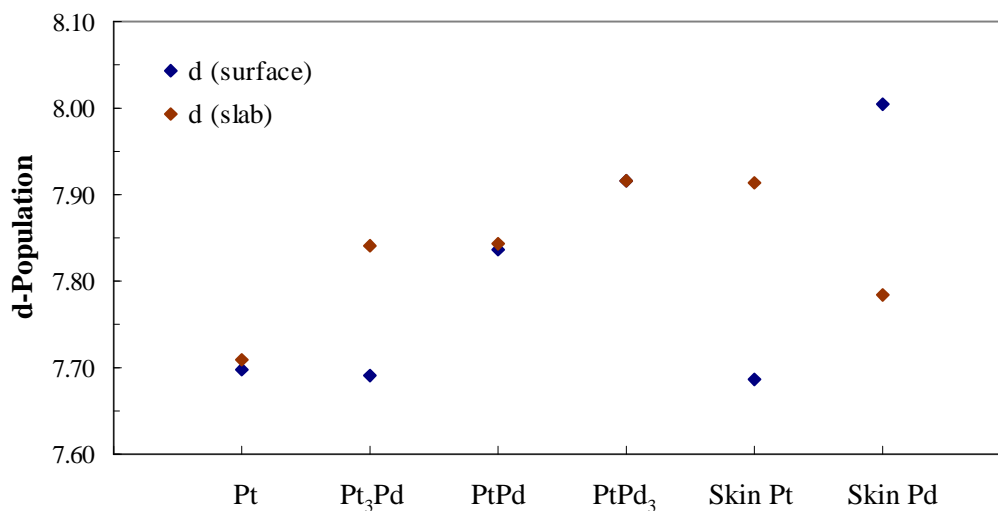


Figure 4.5. Average electronic d-population on the surface and in the four-layer slab after adsorption of OH. The skin slabs are skin Pt/Pd and skin Pd/Pt respectively.

Thus comparing the values of Δ_{slab} after adsorption of OOH among the different surfaces, the largest change is observed on the Pt₃Pd surface, with OH adsorption strength comparable to pure Pt (Figure 4.3); such large change seems to be not only due to the presence of the adsorbate but also because of charge redistribution in the slab, possibly due to oxidation of Pd atoms. On the other hand, for Δ_{surf} after O adsorption large changes are found for PtPd₃ and for the skin Pd/Pt surfaces, both yielding the strongest binding energies (Figure 4.4); in those cases note that the corresponding Δ_{slab} is also negative, suggesting that the decrease of d population on the surface is due mainly to charge transfer to the adsorbate.

Table 4.4

Changes in d-electron population after adsorption of OOH, OH, and O, defined as percents with respect to the population found in the naked surface. In each group, Δ_{surf} is the change on the surface, and Δ_{slab} is the change per atom averaged for the total slab. Largest changes indicate significant depletion of the d population and are shown in bold font

	OOH		OH		O	
	Δ_{surf}	Δ_{slab}	Δ_{surf}	Δ_{slab}	Δ_{surf}	Δ_{slab}
Pt	-0.075	-0.043	-0.130	-0.035	-0.104	-0.019
Pt ₃ Pd	-0.064	-0.016	-1.153	0.784	-0.196	-0.041
PtPd	-0.070	-0.006	-0.245	-0.047	-0.261	-0.040
PtPd ₃	-0.060	-0.009	-0.217	-0.036	-0.362	-0.070
Skin Pt/Pd	-0.055	0.024	-0.123	0.009	-0.127	0.020
Skin Pd/Pt	-0.112	-0.028	-0.175	-0.051	-0.449	-0.110

Thermodynamic Reactivity of Pt-Pd Catalysts

According to Figure 4.6 the free energy changes ΔE_1 for the first electron-proton transfer is parallel to ΔE_2 corresponding to the dissociation of OOH into OH and O, and since both pathways are driven by the chemisorption of oxygenated species such as OOH (equation 1.3) and OH and O (equation 1.4), the catalyst surface that favors the formation of M-OOH, at the same time will favor the dissociation of this specie into M-OH and M-O by elongation of the O-O distance. Figure 4.6 also shows the different trend of ΔE_4 with respect to ΔE_1 proving that the stability of the OH and O (reaction 1.3) do not favor the reduction of these species to water.

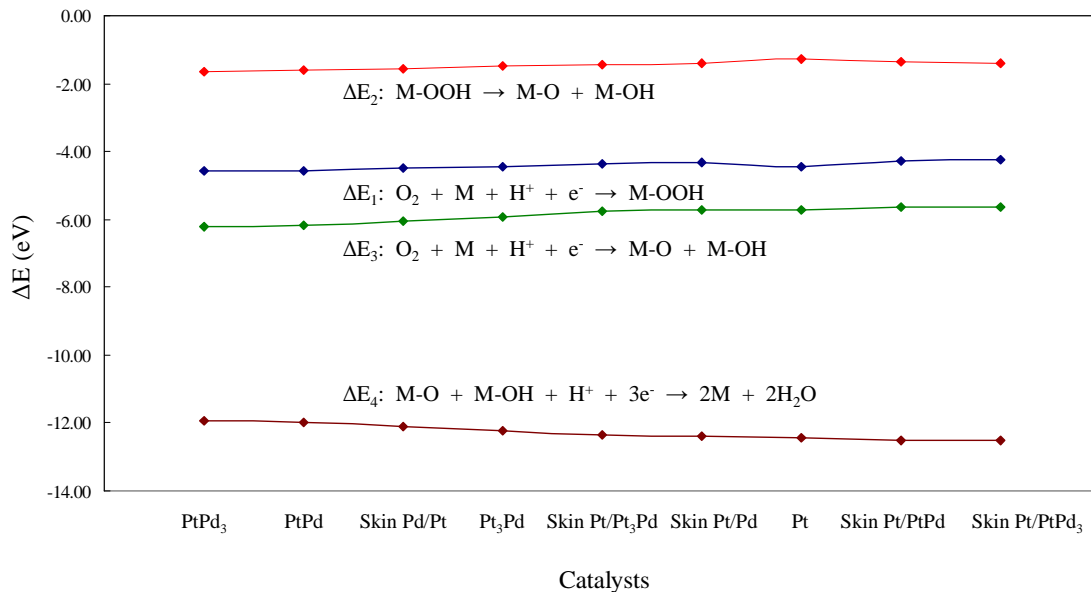


Figure 4.6. Reaction free energy changes for equations 1.3-1.6 (ΔE_1 , ΔE_2 , ΔE_3 , and ΔE_4) of Pt and Pt-Pd alloy catalysts.

Figure 4.7 depicts the relative reaction energies $\Delta\Delta E_1$ corresponding to equation 1.3 (first electron transfer step) and $\Delta\Delta E_4$ corresponding to equation 1.6 (last three electron transfer steps) for all cases taking Pt as a reference, it is observed that none of the studied Pt-Pd alloys provides both negative $\Delta\Delta E_1$ and $\Delta\Delta E_4$, therefore the best surfaces are those that have the smallest values of $\Delta\Delta E_1$ and $\Delta\Delta E_4$, i.e., they are the closest to pure Pt. For the skin monolayer systems $\Delta\Delta E_1$ is slightly positive due to the presence of Pd atoms in the substrate that decrease the binding strength of Pt to OOH. Figure 4.7 shows that $\Delta\Delta E_1$ decreases as *less* Pd atoms are loaded in the subsurface, the best surfaces follow the order: skin Pt/PtPd > skin Pt/PtPd₃ > skin Pt/Pd > skin Pt/Pt₃Pd; and the same surfaces give the smallest values of $\Delta\Delta E_4$. On the other hand, $\Delta\Delta E_4$ becomes more positive as *more* Pd atoms are present (as in PtPd₃, PtPd, and skin Pd/Pt), because the presence of Pd enhances the binding strength especially of atomic oxygen (Figure 4.4) making these surfaces less appropriate for reduction of O and OH (equation

1.6), in agreement with experimental analyses of Pd monolayers on various substrates.^[15]

According to our thermodynamic analysis, the best alloy of the group of bulk ordered alloys may be Pt₃Pd, which is almost as good as Pt for dissociating the OO bond, and it performs better than the other bulk ordered alloys for reduction of adsorbed O and OH. In a previous study, we had analyzed similar overall compositions in small clusters (a total of 10 atoms)^[100]. Comparing those results on the 10-atom clusters to the ones in this work, on slabs representing extended surfaces, we note that there are general trends common to both sets of systems, such as the effect of Pd for enhancing the adsorption energy of the oxygenated compounds and the lower reactivity of the Pt-skin surfaces; however the distinct nature (shape, geometry, electronic structure) of the small clusters and their tendency to become polarized even in the absence of the adsorbate (see Table 2 in reference^[100]) yields some interesting differences. In the case of the 10-atom clusters we found the disordered system Pt₃Pd₇ (PtPd_{2.33}) and the ordered Pd-monolayer over Pt (Pd_{2.33}Pt) the best towards the ORR reaction according to equations 1.3 and 1.6. Recent work by Crooks et al.^[106] reported kinetic current densities at different potentials for dendrimer-encapsulated Pt-Pd nanoparticles, and enhanced current values with respect to pure Pt were found in a range between Pt₂Pd and Pt₅Pd with a maximum of activity approximately at a composition Pt₅Pd. These findings are in fair agreement with the trend observed in Figure 4.7, and differ from our results on very small clusters, making clear the reactivity difference based on size.

Regarding the lattice constants in Table 4.1, there is no clear trend with reactivity. Note however that the lattice constant only represents an average for the system; individual surface metal-metal bond lengths could vary according to the specific surface compositions; thus additional analysis is needed to establish a clear relationship between specific geometries and reactivity.

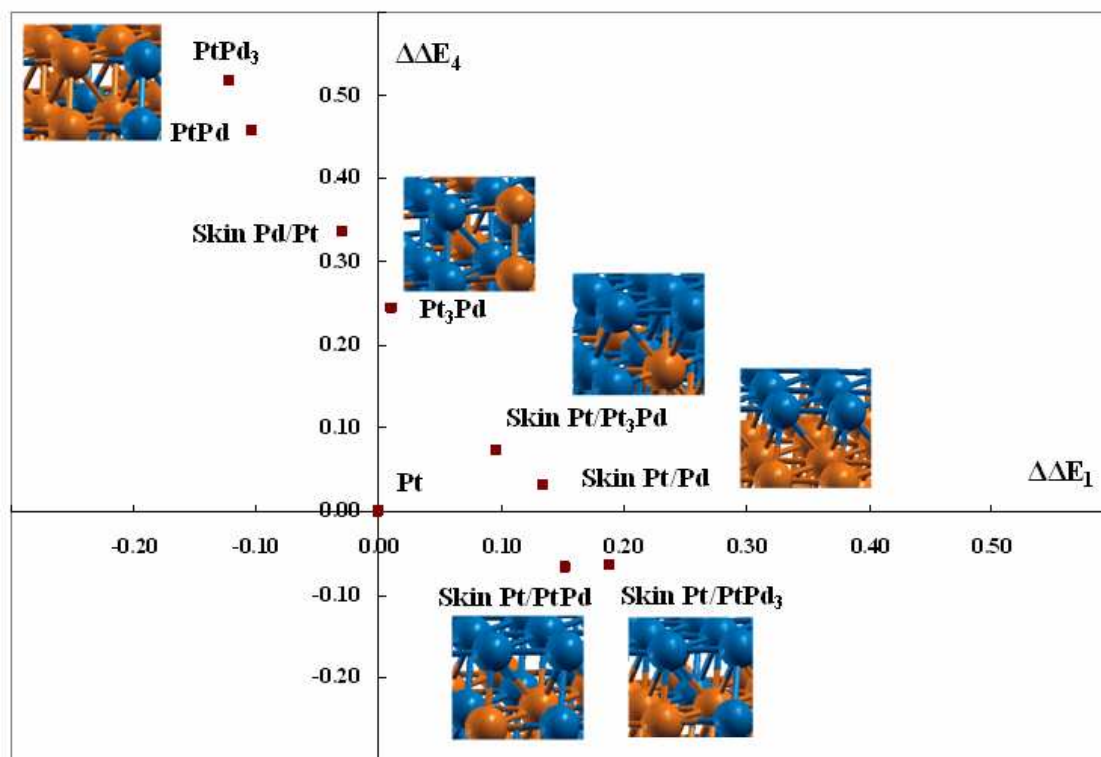


Figure 4.7. Relative free energies (eV) according to equations 1.3 and 1.6 for Pt and Pt-Pd alloys with respect to pure Pt.

Correlation Between the Surface d-band Center and the ORR Intermediates

Minhua Shao et al. ^[40] found using DFT calculations a volcano type dependence between the measured ORR activity of Pt or Pd monolayers supported on many different noble metal single crystals and their calculated d-band center and the atomic oxygen binding energy. The d-band center values reported for Pt and Pd are closest to -2.18 and -1.80 eV respectively, while in this study we found d-band center values of -2.16 (Figure 4.8) and -1.67 eV for Pt and Pd respectively. Figure 4.9 shows the changes of the partial density of states of the d-electrons as a function of the Pd content in the Pt-Pd alloy from a high Pd content (PtPd₃) to low Pd content (Pt₃Pd). It is observed a shift of the partial density of states and the d-band to negative values as the Pd content decreases and the Pt content increases reaching Pt partial density of state positions. This behavior can be

attributed to the electronic interactions between Pt and Pd atoms because of the relaxation of the bond distance of the atoms due to the increase of Pt content in the slab.

As it is proposed by Stamenkovic et al.^[107] the best catalyst is predicted to bond oxygen more weakly than pure Pt by 0.2 eV. The binding energies of atomic oxygen found in this study are around -1.86 eV at the top of the volcano plot for Pt skin on Pd₃Fe, which is consistent with this prediction. Nevertheless weaker interactions with O are needed to achieve the enhancement, lower atomic oxygen binding energies than -1.86 eV do not favor the activity of the ORR, suggesting an optimum value for this adsorption. This fact is in agreement with our results and can be attributed to the trend found for the adsorption of OOH and O and OH. The more strongly O and OH are adsorbed on the catalyst, the stronger OOH is adsorbed.

Figure 4.10 shows the almost linear relationship between the calculated surface d-band center for Pt, Pt₃Pd, PtPd, PtPd₃, skin Pt/Pd, skin Pd/Pt, skin Pt/Pt₃Pd, skin Pt/PtPd, and skin Pt/PtPd₃ and the atomic oxygen binding energy. M. Shao et al.^[40] and Norskov^[97] showed similar trends, but using the d-band center values for the periodic slab instead of using the surface d-band center value, which is directly related to the reactivity and adsorption of all the intermediates.

We found that the smaller the surface d-band center, the strongest atomic oxygen adsorption to the surface. As we can expect the other intermediates OH and OOH have similar trends (Table 4.5). Nevertheless the reduction of the interaction distances between the metals on the surfaces due to the reduction of the lattice constant increases the interaction of all the intermediates, and somehow favor the first electron and proton transfer (equation 1.3), at the same time this effect is translated into a different effect for the last the electron and proton transfers (equation 1.6); increasing the interaction of the adsorption of both the hydroxyl and the atomic oxygen intermediates. This evidence is in agreement with M. Shao's work^[40], who found that the maximum enhancement in the ORR electroactivity for the Pd monolayer catalyst is located at an intermediate point along the d-band center of the catalysts. Mavrikakis^[18] also stated that lowering the d-band center will make the catalyst less reactive because the weak interactions of the

ORR intermediates and the catalyst surface. However in some degree this can make the catalyst more active toward the ORR due to the weak interactions of OH and O that facilitate their reduction to water.

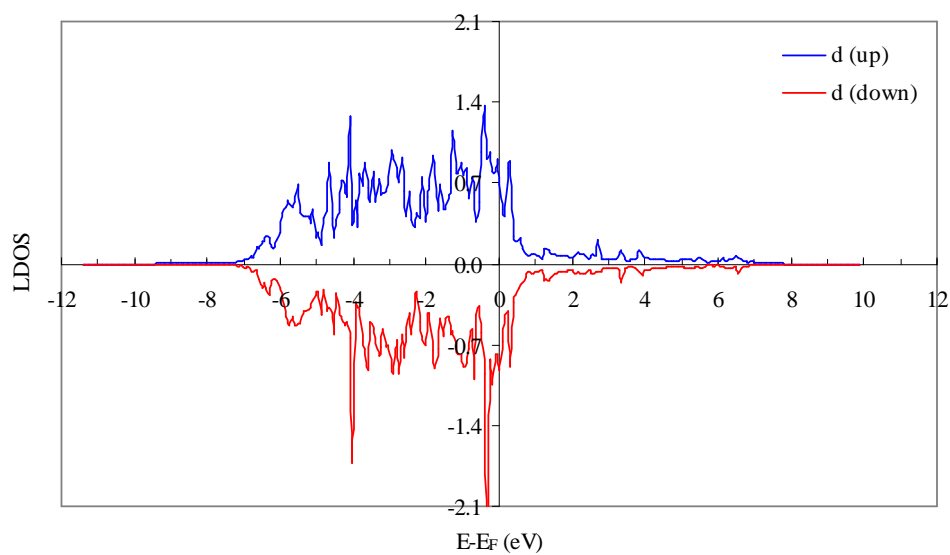


Figure 4.8. Partial density of states of d-electrons for Pt(111). $E_{\text{d-band center}}(\text{Pt}) = -2.16 \text{ eV}$

Table 4.5

Slab and surface d-band center ordered with respect to the surface d-band center

Pt:Pd	M	d-band center	Surf. d-band center	L.C.	B.E. (OOH)	B.E. (OH)	B.E. (O)
100:00	Pt	-2.16	-1.96	3.98	-1.08	-2.27	-3.92
81:19	Skin Pt/Pt ₃ Pd	-2.04	-1.91	3.97	-0.99	-2.29	-3.98
75:25	Pt ₃ Pd	-2.05	-1.87	3.96	-1.07	-2.37	-4.05
44:56	Skin Pt/PtPd ₃	-1.86	-1.87	3.95	-0.90	-2.18	-3.95
25:75	SkinPt/Pd	-1.76	-1.83	3.95	-0.95	-2.23	-4.00
50:50	PtPd	-1.91	-1.74	3.95	-1.19	-2.45	-4.20
75:25	Skin Pd/Pt	-2.10	-1.68	3.96	-1.11	-2.31	-4.21
25:75	PtPd ₃	-1.81	-1.66	3.94	-1.21	-2.51	-4.20
00:100	Pd	-1.67	-1.52	3.94	-1.02	-2.22	-4.20

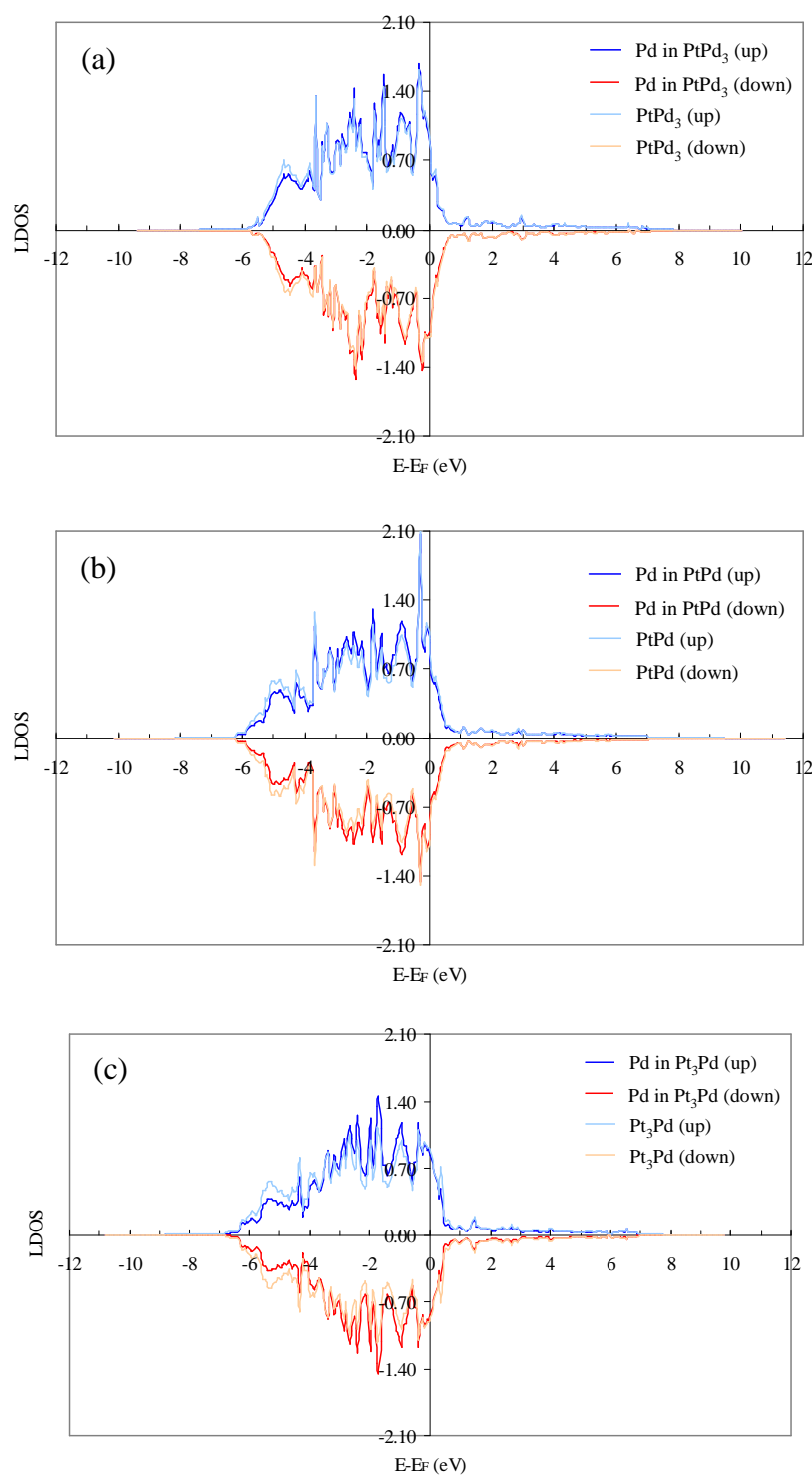


Figure 4.9. Comparison of the partial density of states of d-electrons for Pd in Pt-Pd alloys. (a) Pd in PtPd₃ ($E_{d\text{-band center}} = -1.765$ eV), (b) Pd in PtPd ($E_{d\text{-band center}} = -1.825$ eV), and (c) Pd in Pt₃Pd ($E_{d\text{-band center}} = -1.906$ eV).

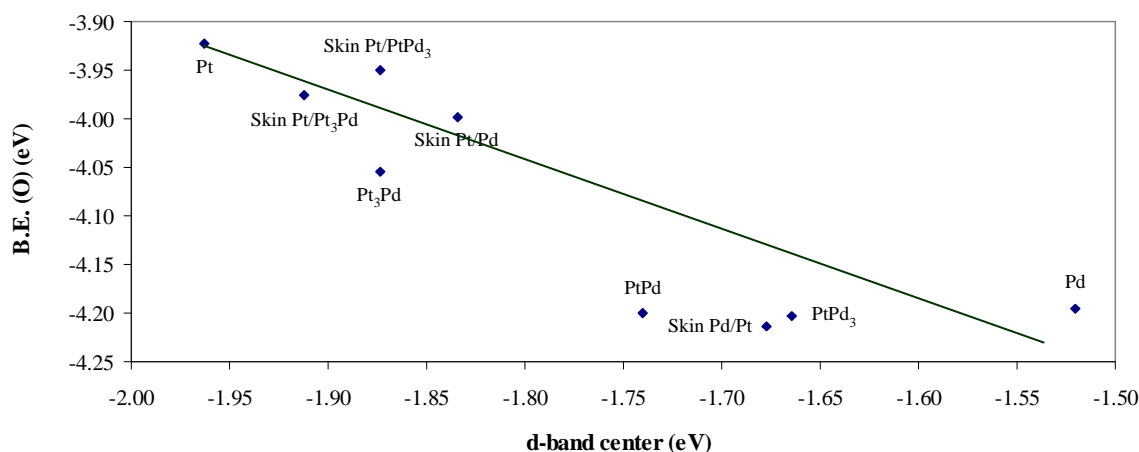


Figure 4.10. Binding energies of O as a function of the surface d-band center for Pt, Pt₃Pd, PtPd, PtPd₃, skin Pt/Pd, skin Pd/Pt, skin Pt/Pt₃Pd, skin Pt/PtPd, and skin Pt/PtPd₃.

Transition State Calculations of the OOH Dissociation on Pt(111) and Pt₃Pd(111)

As it was suggested by Anderson ^[48] and Damjanovic ^[47] the proton transfer participates in the first electroreduction step. This step also involves the electron transfer, yielding to the formation of the OOH radical. This step could be considered the rate determining step of the ORR because of its activation barrier of 0.4 eV ^[59].

The OOH dissociation follows this step, which is crucial to understand because of its implication in the further reduction of OH and O species into water. Today there is no a complete understanding of the barrier and pathway for this event. For that reason we analyze the transition state of the OOH dissociation on Pt and then Pt₃Co to compare the effect of the alloyed catalyst toward the dissociation of OOH into OH and O.

In this section the climbing image nudged elastic band (CI-NEB) method ^[91] to obtain the pathway of the OOH dissociation and to finds the OOH dissociation barrier. The CI-NEB method is an efficient method to find the minimum energy pathway (MEP) between the given initial and final state of transition, which have been previously optimized. In the initial configuration OOH is adsorbed on top Pt site and in the final configuration after the OOH dissociation into OH and O it was found that the most

stable conformation corresponds to the hydroxyl adsorption on top Pt sites and the atomic oxygen adsorption on fcc hollow sites. The results of the CI-NEB calculation of the OOH dissociation on Pt(111) are shown in Figure 4.11. An activation barrier of 0.32 eV is found. In the same plot the O-O elongation bond length is reported during the dissociation event. In the saddle point it is found a O-O bond length of 1.902 Å, which varies by 33 % with respect to the initial Pt-OOH structure (1.430 Å). The Pt-O distances are 1.903 Å and 2.096 Å, the angle Pt-Pt-O is 81.9 ° and the angle Pt-O-O is 102.3 °. In earlier investigations Sidik and Anderson ^[48] reported a much more smaller activation barrier of 0.06 eV using a initial structure of Pt₂-OOH, finding Pt-O distances of 1.842 Å and 2.017 Å, Pt-Pt-O angle of 76.7 °, and Pt-O-O angle of 107.6 °. A much higher activation barrier was reported over a Pt₁₅ cluster with an activation barrier of 0.22 eV, which is close to what we computed for the OOH dissociation on a Pt(111) periodic slab cluster.

From Figure 4.7 it is observed that the closest Pt-Pd alloy catalyst to behave like Pt toward the first electroreduction step is Pt₃Pd ($\Delta\Delta E = 0.01$ eV). We use this catalyst to evaluate the OOH dissociation and to compare how the presence of Pd atoms in the surface can alter the OOH dissociation activation barrier. Figure 4.12 shows the results of the CI-NEB calculation of the OOH dissociation on Pt₃Pd(111). In the same way as the previous case the most stable conformations are used for the initial and final configurations. For Pt₃Pd, an activation barrier of 0.35 eV was computed, which is very close to the one on Pt(111) (0.32 eV). In the same plot the O-O elongation bond length is reported during the dissociation event. In the saddle point it is found a O-O bond length of 2.503 Å, which varies by 73.8 % with respect to the initial Pt₃Pd-OOH structure (1.440 Å). The Pt-O distance is 1.843 Å, Pd-O distance is 1.987 Å, the angle Pt-Pt-O is 92.5 ° and the angle Pt-O-O is 89.0 °. As it is observed although the activation barrier in both cases is very close (which is in agreement with the small $\Delta\Delta E$), some of the geometric characteristics are not necessarily close. In this section it is pointed out that the pathways between states have nothing to do with what the system really does dynamically under real conditions. Sometimes, the guess which is assumed by the

method based on the minima found in the calculations of the initial and final structures is used by the program to map and suggest a pathway between the minima that we found. It is good, however, to keep in mind that that something important on the reaction pathway could be missing. And of course there is qualitative valuable information that is provided by these numerical simulations.

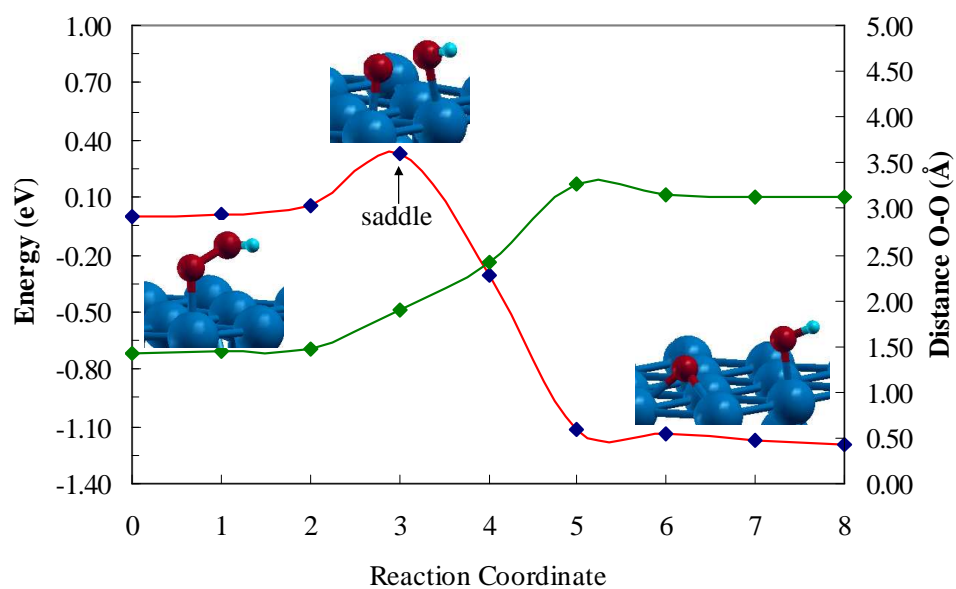


Figure 4.11. Transition state pathway for the OOH dissociation on Pt(111) (red line) and elongation distance O-O (green line).

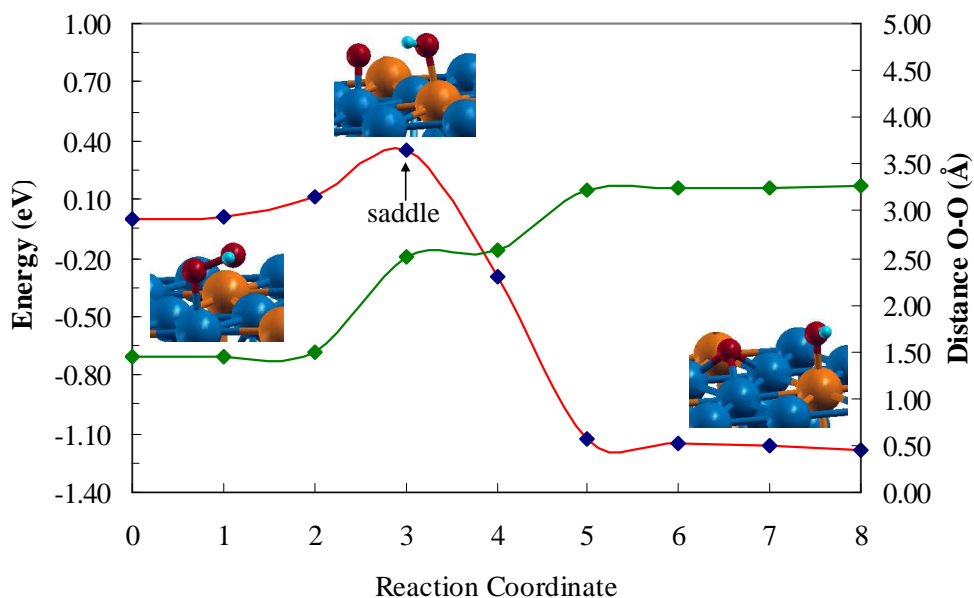


Figure 4.12. Transition state pathway for the OOH dissociation on Pt₃Pd(111) (red line) and elongation distance O-O (green line).

Summary

Periodic DFT calculations have been performed using Pt and Pt-Pd alloys to analyze the ORR thermodynamic trends. From all cases, none of the studied Pt-Pd systems yield *both* negative $\Delta\Delta E$ s (relative to pure Pt) for the change of reaction energy representing the first electron and proton transfer to molecular oxygen, *and* for the reaction representing the reduction of adsorbed hydroxyl and atomic oxygen. Thus, it is shown that the catalytic reactivity is related not only to the overall composition but especially to the atomic distribution, particularly on the surface and near-surface. The d-electron distribution differs significantly between the “bulk ordered” vs. the “skin” surfaces; in the bulk ordered the increase in d population is directly proportional to the amount of Pd, whereas in the skin surfaces there is a large difference between the surface population and that of the average slab. After adsorption of the oxygenated compounds, there are slight changes in the d population of the metal atoms, usually a

decrease is observed on the d surface population due both to electron transfer to the adsorbates and to the metal subsurface atoms. In addition the calculated surface d-band center is correlated with all the intermediates of the ORR, not only atomic oxygen as it was found in previous investigations, but also with hydroxyl and OOH. That is the reason why the activation of the OOR can not be correlated directly to the d-band center.

It was found that the adsorption of oxygenated species is stronger on Pt-sites of Pd-rich surfaces; thus those would be favorable surfaces to dissociate oxygen, however the skin-surfaces are better suited for O and OH reduction while they perform similar to pure Pt for O-O dissociation. It was observed that the best surfaces for the ORR are those that have the smallest values of $\Delta\Delta E_1$ and $\Delta\Delta E_4$, i.e., they are the closest to pure Pt, and therefore should behave like Pt. This fact has been demonstrated analyzing the activation barrier for catalyst with almost the same $\Delta\Delta E_1$.

In summary, it could be concluded that the Pt-skin surfaces are the best alloys of this group because of their ability to emulate a pure Pt surface.

CHAPTER V

CHEMICAL REACTIVITY OF Pt₃Co, Pt₃Ni, Pt₃V, AND Pt₄Rh ALLOY CATALYSTS

Introduction

In the previous chapter we observed that the skin Pt monolayer catalysts are the most suitable for the ORR. In addition a Pt:X (X: alloy metal) surface ratio 3:1 can also have some impact toward the ORR. This fact can be supported by the changes in the electronic structure with respect to that of pure Pt and to changes of the physical structure of the catalyst (metal-metal catalyst distances). Mukerjee and Srinivasan^[31] and Min et. al.^[27] reported an ORR activity enhancement by a factor of 1.1 to 3 on several binary Pt-M (3:1) alloy catalysts. Toda et. al.^[9; 33] reported the effect of Pt alloying with Ni, Co, and Fe, prepared by sputtering, on the ORR activity and found enhancement factors of 10, 15, and 20 with 30, 40, and 50 atomic % Ni, Co, and Fe, respectively, which was attributed to electronic effects. The two selected distributions for each bimetallic catalyst in this chapter; the ordered structure and the skin Pt monolayer catalysts (Figure 5.1) were chosen considering the previously mentioned facts. In addition two different criteria were used. The first one is the segregation information for each of the components of the catalyst. Ruban et al.^[108] reported a database with surface segregation energies of single transition metal impurities in transition metal hosts; it is shown that Rh, Ni, Co, and V present a moderate to strong anti-segregation of 0.26, 0.43, 0.46, and 0.98 eV per atom respectively. The second criterion is the information found in some studies about the dissolution of the metal from the cathode catalyst during the cell operation^[9; 33; 43]. It was found that in wet cells after the immersion of the bimetallic catalyst in an acid electrolyte, a skin consisting of a monolayer of pure Pt is formed on the surface. These results indicate the dissolution of the metal from the cathode catalyst during the cell operation. Recent studies on the catalytic activity and stability of supported Pt-Co alloys with well-defined structures by Watanabe et al.^[41] demonstrated that both Co and Pt dissolve out preferentially from

small-size alloy particles and Pt re-deposits on the surfaces of large-size ones in hot H_3PO_4 . As a result, an alloy with a disordered crystallite structure, which is more corrosion-resistant than an ordered one, maintains higher electrocatalytic activity for a longer time due to the active alloy surfaces with a relatively large surface area. It was also found that that a fine Pt alloy catalyst is covered with a pure Pt skin under the practical operation conditions in PEMFCs ^[41]. Thus, it is important to examine the electronic–structure changes of alloy surfaces as a possible factor for the enhancement in combination with the surface composition.

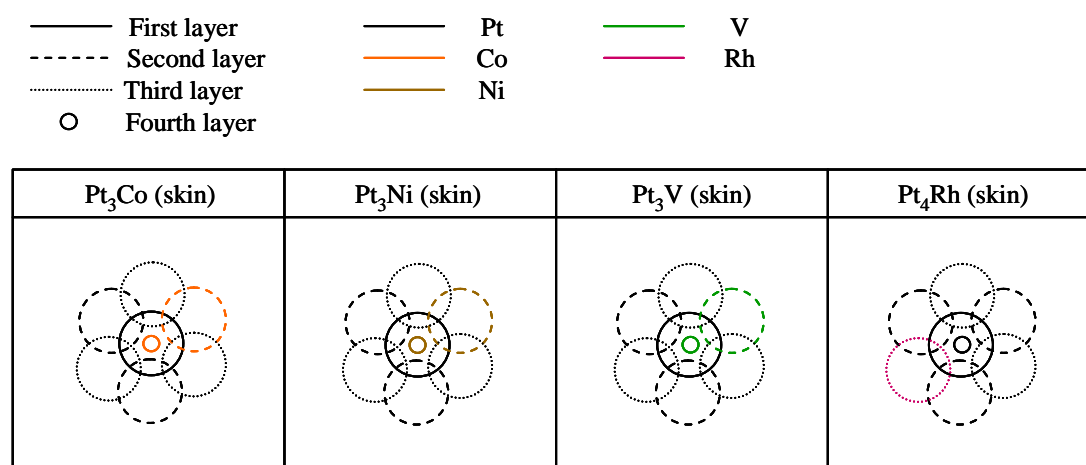


Figure 5.1. Distribution layer by layer for top adsorption sites of OOH and OH on skin Pt monolayer of Pt_3Co , Pt_3Ni , Pt_3V , and Pt_4Rh .

Lattice Constant and Slab Structures of Pt and Pt-X Catalysts (X: Co, Ni, V, and Rh)

Experimental values of lattice constants have been reported for ordered Pt_3Co , 3.85 \AA ^[109], and for Pt 3.92 \AA ^[110]; the predictions in Table 5.1 slightly overestimate these values by 0.77% and 1.53% respectively, in agreement with other theoretical studies ^[18; 111; 112]. We computed lattice constants for Pt, Pt_3Co , Pt_3Ni , Pt_3V , and Pt_4Rh of 3.98 \AA , 3.88 \AA , 3.88 \AA , 3.92 \AA , and 3.95 \AA respectively.

Table 5.1

Lattice constants and slab layer by layer distribution for Pt, Pt₃Co, Pt₃Ni, Pt₃V, and Pt₄Rh. The Pt:M layer by layer distribution is indicated starting from the surface composition

System	Case	Lattice constant (Å)	Pt:M distribution per layer
Pt		3.98	4:0 4:0 4:0 4:0
Pt ₃ Co (Skin Pt)	A	3.88	4:0 3:1 3:1 2:2
Pt ₃ Co	B	3.88	3:1 3:1 3:1 3:1
Pt ₃ Ni (Skin Pt)	A	3.88	4:0 3:1 3:1 2:2
Pt ₃ Ni	B	3.88	3:1 3:1 3:1 3:1
Pt ₃ V (Skin Pt)	A	3.92	4:0 3:1 3:1 2:2
Pt ₃ V	B	3.92	3:1 3:1 3:1 3:1
Pt ₄ Rh (Skin Pt)	A	3.95	4:0 3:1 3:1 3:1
Pt ₄ Rh	B	3.95	3:1 3:1 3:1 4:0

Binding Energies of ORR Intermediates on Pt(111) and Pt-X(111) Surfaces (X: Co, Ni, V, and Rh) and Structural Characteristics

In this section we evaluate the binding properties of OOH, OH, and O. From equations 1.3 and 1.6, as it was suggested in the previous chapter, the first electron reduction step is favored by strong OOH adsorption while the last three electron reduction steps are favored by weak O and OH adsorption, which will promote the reduction of O and OH to water. And a good ORR catalyst could be designed as the combination of a metal that adsorbs OOH stronger than Pt plus a second metal able to bind OH and O less strong than Pt, thus these species can be easily reduced to water. Tables 5.2 and 5.3 show the binding energies and some structural characteristics of all the ORR intermediates adsorbed on Pt, Pt₃Co, Pt₃Ni, Pt₃V, and Pt₄Rh surfaces.

It is found that the fcc hollow is the most stable adsorption site for atomic oxygen on Pt, Pt₃Co, Pt₃Ni, Pt₃V, and Pt₄Rh surfaces. Xu et al. reported theoretical calculation with values of -3.88 eV, -4.29 eV, and -3.50 eV for oxygen in the hollow fcc site of Pt, Pt₃Co and skin Pt/Pt₃Co respectively (surface coverage 1/4 ML) in good agreement with

our calculations. Campbell et al. ^[113] and Gland et al. ^[56] estimated from experiments the binding energy of atomic oxygen on Pt(111) to be -3.6 eV. Karlberg ^[112] also reported similar DFT calculated values for the adsorption of atomic oxygen and hydroxyl on Pt (111) and skin Pt monolayers and Panchenko et al. ^[111] reported values for the adsorption of OOH, OH, and O on Pt(111): -1.07 eV, -2.23 eV, and -4.08 eV respectively.

Table 5.2 shows that the adsorption of the intermediates OOH, OH and O is weaker on skin Pt surfaces. The presence of any of the metal alloy elements used in this study in the substrate of the periodic slab reduces the interaction of the surface with the oxygenated species mainly because of the redistribution of the charges found in the skin monolayer and the substrate; this is clearly observed in the distribution of the d-population of the periodic slab (see Figure 5.3). On the other hand the presence of the alloy metal on the surface increases the interaction of the OOH with the surface particularly when the adsorption takes place on the alloy metal site, generating a strong adsorption of OOH. This strong OOH interaction elongates the distance O-O facilitating the dissociation of OOH into OH and O. Even if the oxygenated species are adsorbed on Pt, for example OOH adsorbed on Pt₃V (homogeneous distribution) yields a binding energy of -1.37 eV and a O-O distance of 1.513 Å compared to 1.430 Å in pure Pt. This trend is found in all cases (Pt₃Co, Pt₃V, and Pt₄Rh surfaces) except on Pt₃Ni surfaces; the OOH adsorption in Pt sites for this case is -1.00 eV while the adsorption on Ni sites is -0.92 eV. This behavior could be attributed to the oxidation of Ni atoms donating electrons to the Pt neighbor atoms in the surface based on the d-population of the Ni surface atoms, which decreases once OOH is adsorbed in Pt atoms. It is pointed out that the value reported in Table 5.2 for the binding energy when OOH is adsorbed on Vanadium corresponds to the average of the hydroxyl and atomic oxygen. This is the only case we found that the adsorption of OOH leads to an instantaneous dissociation (Figure 5.2).

The presence of the metal alloy in the surface increases strongly the interaction of hydroxyl and especially atomic oxygen, thus making difficult the reduction of these

species to water. In contrast, skin Pt monolayers of Pt₃Co, Pt₃Ni, Pt₃V, and Pt₄Rh favor the reduction of both atomic oxygen and hydroxyl allowing weaker interaction on the most stable sites of these species compared with pure Pt.

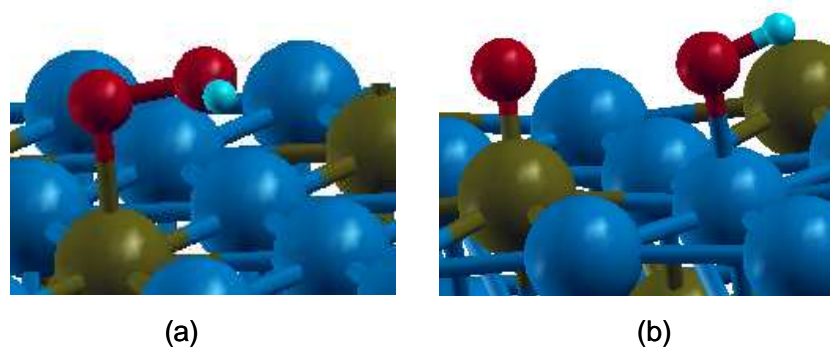


Figure 5.2. Initial (a) and final (b) structures (after optimization) for the OOH adsorption on Vanadium atom in Pt₃V slab.

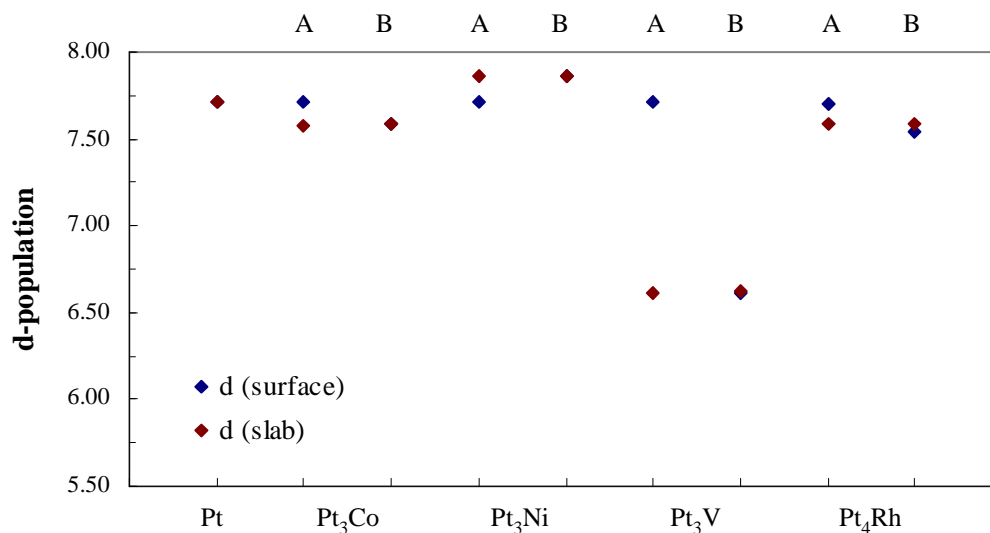


Figure 5.3. Average electronic d-population on the surface and in the four-layer slab for Pt, Pt₃Co, Pt₃Ni, Pt₃V, and Pt₄Rh (cases A and B).

d-Population Analysis

Table 5.3 shows the structural relaxation of the surfaces as differences from the bulk separation between the first two layers after relaxation with respect to the bulk conformation. It was found that most of the homogeneous Pt-X (X: Co, Ni, V, and Rh) distribution atoms on the surface relax inwards by a small amount (-1.81 %) while most of the Pt-skin monolayer surfaces (except the one on Pt₄Rh) relax outward by a noticeable amount. On the other hand, all the homogeneous distribution surfaces relax inwards with the highest values of -2.62%, found for Pt₃V, and Pt₄Rh. All the details of the catalyst surface relaxation with respect to the bulk structure are listed in Table 5.4.

Table 5.2

Binding energies (BE, in eV) of OOH, OH, and O on Pt, Pt₃Co, Pt₃Ni, Pt₃V, and Pt₄Rh surfaces. BEs calculated as: $BE_{\text{slab-adsorbate}} = E_{\text{slab+adsorbate}} - E_{\text{slab}} - E_{\text{adsorbate}}$. Interactions with either Co or Ni or V or Rh are indicated in bold font

M	Case	BE (M-OOH)	BE (M-OH)	BE (M-O (fcc))	comment
Pt		-1.08	-2.27	-3.92	
Pt ₃ Co (Skin Pt)	A	-0.83	-2.11	-3.42	All weaker
Pt ₃ Co	B	-1.05 -1.10	-2.28, -2.57	-4.22	All stronger on Co; OOH weaker on Pt
Pt ₃ Ni (Skin Pt)	A	-0.88	-2.16	-3.51	All weaker
Pt ₃ Ni	B	-1.00 , -0.92	-2.32, -2.30	-4.14	All stronger on Ni except OOH; OOH weaker on Pt as well
Pt ₃ V (Skin Pt)	A	-0.64	-2.00	-3.23	All weaker
Pt ₃ V	B	-1.37, -4.16*	-2.16 , -3.93	-6.01	All stronger on V; OH weaker on Pt
Pt ₄ Rh (Skin Pt)	A	-0.93	-2.22	-3.91	All weaker
Pt ₄ Rh	B	-1.13, -1.29	-2.24 , -2.50	-4.37	All stronger on Rh; OH weaker on Pt

* OOH adsorption on Vanadium atom leads to an instantaneous dissociation into OH and O due to the strong interaction between the surface and the OOH intermediate (-4.16 eV after the dissociation), which elongates the O-O distance dissociating this bond.

The separation found in skin Pt monolayers is mainly caused by the rearrangement of the electronic density in the slab. This effect is observed in the d-population analysis shown in Figure 5.3. The average d-population on the surface is higher than that in the slab by approximately the same amount in the Pt-skin surfaces over Pt₃Co and Pt₄Rh, whereas it is much higher on the surface than in the slab of skin Pt/Pt₃V, and is lower on the surface than in the slab of skin Pt/Pt₃Ni. On the other hand it is observed that the average d-population is practically the same for the catalyst with homogeneous distribution in all the slab layers (cases B).

Table 5.3

Structural characteristics of the adsorption of oxygenated species on Pt, Pt₃Co, Pt₃Ni, Pt₃V, and Pt₄Rh. Atomic oxygen is adsorbed on fcc hollow sites while hydroxyl and OOH adsorb on top sites. Interactions with either Co or Ni or V or Rh are indicated in bold font

M	Case	M-OOH d _{O-O}	M-OOH d _{M-O}	M-OH d _{M-O}	M-O d _{M-O fcc}	M-O d _{M-O hcp}	d-band center (eV)
Pt		1.430	2.037	2.002	2.042	2.055	-2.16
Pt ₃ Co (Skin Pt)	A	1.427	2.032	2.009	2.032 2.038 2.042	2.080 2.052 2.039	-1.99
Pt ₃ Co	B	1.492 1.486	2.023 1.807	2.002 1.808	2.044 2.055 1.878	2.058 2.070 1.883	-2.02
Pt ₃ Ni (Skin Pt)	A	1.423	2.038	2.006	2.041 2.040 2.033	2.072 2.058 2.040	-1.95
Pt ₃ Ni	B	1.434 1.443	2.014 1.848	1.994 1.821	2.030 2.037 1.879	2.041 2.040 1.892	-1.98
Pt ₃ V (Skin Pt)	A	1.432	2.049	2.019	2.023 2.023 2.017	2.079 2.070 2.054	-1.88
Pt ₃ V	B	1.513 2.865	2.109, 2.055 1.614 ,2.023	2.025 1.774	3.489 3.471 1.605	1.606	-1.92
Pt ₄ Rh (Skin Pt)	A	1.427	2.031	2.002	2.038 2.042 (2)	2.055 2.058 (2)	-2.11
Pt ₄ Rh	B	1.491 1.447	2.035 1.964	2.002 1.960	2.044 2.035 1.995	2.048 2.059 1.995	-2.12

Table 5.4

Surface relaxation estimated as changes from bulk separation between the first two layers Δ_{12}

M	Cases	Pt:M distribution layer by layer starting from top	Separation Δ_{12} (Å)	% Separation change wrt bulk
Pt		4:0 4:0 4:0 4:0	2.38	-1.81
Pt ₃ Co (Skin Pt)	A	4:0 3:1 3:1 2:2	2.36	3.29
Pt ₃ Co	B	3:1 3:1 3:1 3:1	2.26	-1.97
Pt ₃ Ni (Skin Pt)	A	4:0 3:1 3:1 2:2	2.36	2.49
Pt ₃ Ni	B	3:1 3:1 3:1 3:1	2.29	-1.52
Pt ₃ V (Skin Pt)	A	4:0 3:1 3:1 2:2	2.34	0.28
Pt ₃ V	B	3:1 3:1 3:1 3:1	2.28	-2.62
Pt ₄ Rh (Skin Pt)	A	4:0 3:1 3:1 3:1	2.37	-0.59
Pt ₄ Rh	B	3:1 3:1 3:1 4:0	2.33	-2.62

Thermodynamic Reactivity of Pt, Pt₃Co, Pt₃Ni, Pt₃V, and Pt₄Rh Catalysts

In a similar way to the behavior of Pt-Pd catalyst model surface, Figure 5.4 shows the free energy changes ΔE_1 for the first electron-proton transfer is parallel to ΔE_2 corresponding to the dissociation of OOH into OH and O for , Pt₃Co, Pt₃Ni, Pt₃V, and Pt₄Rh catalysts, suggesting that both pathways are driven by the chemisorption of oxygenated species such as OOH (equation 1.3) and OH and O (equation 1.4), the catalyst surface that favors the formation of M-OOH, at the same time will favor the dissociation of this specie into M-OH and M-O by elongation of O-O distance. Figure 5.4 also shows the different trend of ΔE_4 with respect to ΔE_1 proving that the strong adsorption of OH and O (reaction 1.3) do not favor the reduction of these species to water. It is pointed out that P₃V (case B) shows a particular behavior compared with the other cases. In this case similar ΔE for reactions 1.3 and 1.4 suggests similar favorability for the formation of the OOH radical and its dissociation into OH and O. At the same time it is the only case that shows lower values for ΔE_3 compared to ΔE_4 .

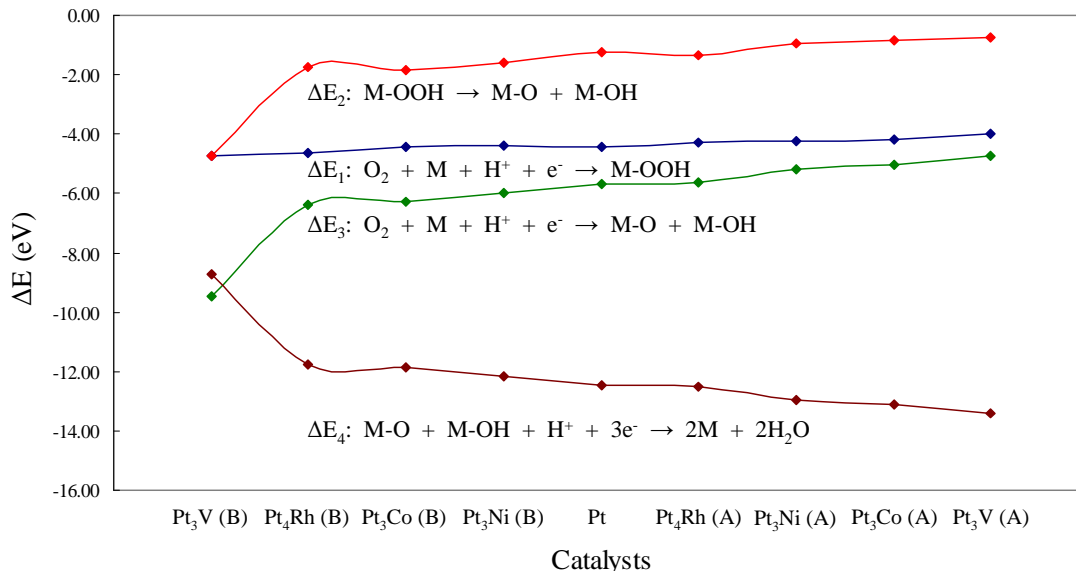


Figure 5.4. Reaction free energy changes for equations 1.3-1.6 (ΔE_1 , ΔE_2 , ΔE_3 , and ΔE_4) of Pt, Pt_3Co , Pt_3Ni , Pt_3V , and Pt_4Rh (case B) and their respective skin Pt monolayers (case A).

In order to compare how each of these systems catalyzes the ORR compared with pure Pt, the reaction energy differences are calculated with respect to pure Pt ($\Delta\Delta E_1$ and $\Delta\Delta E_4$). Thus, the common energetic terms such as protons and water molecules in equations 1.3 and 1.6 cancel out. All the relative energies for Pt_3Co , Pt_3Ni , Pt_3V , and Pt_4Rh (cases A and B) with respect to Pt for reactions 1.3 and 1.6 are listed in Table 5.5. According to thermodynamics, both ΔE_1 and ΔE_4 for a given catalyst should be more negative than those of pure Pt to be able to catalyze better the ORR than pure Pt. For the skin-Pt surfaces we found that none of them has both negative values of $\Delta\Delta E_1$ and $\Delta\Delta E_4$ (relative free energy taking Pt as a reference). For the skin-Pt monolayer surfaces $\Delta\Delta E_1$ is always positive, this is an evidence of the weak interaction of these surfaces with the oxygenated species and consequently of the poor OOH cleavage which makes difficult its further dissociation into OH and O. On the other hand, for the same reason these surfaces favor the reduction of OH and O (equation 1.6) due to their weak interactions with atomic oxygen and hydroxyl compared to the ones in pure Pt, that facilitate the

reduction of OH and O to water. Among all cases, skin Pt monolayer of Pt₃V has the highest $\Delta\Delta E_1$ (0.44 eV), this is reflected in the weak interaction of OOH and the surface with a low binding energy of -0.64 eV. Considering the ORR reactivity in terms of $\Delta\Delta E_{1+4}$ we found the following order: Pt₃V (skin Pt) > Pt₃Co (skin Pt) > Pt₃Ni (skin Pt) > Pt > Pt₄Rh (skin Pt). From these cases, the closest catalyst to the $\Delta\Delta E$ values of Pt is skin Pt/Pt₄Rh.

Similarly, for the homogeneous distribution layer by layer (case B) none of the cases has both negative values of $\Delta\Delta E_1$ and $\Delta\Delta E_4$. But in contrast to the skin-Pt surfaces, these surfaces favor the first electron transfer by having a relatively strong interaction with OOH. For the same reason, the presence of the metal alloy on the surface increases the interaction with atomic oxygen making difficult its reduction to water. Among all cases Pt₃V presents the highest $\Delta\Delta E_4$ (1.97) with a very strong atomic oxygen binding energy (-6.01 eV). Thus, none of these cases has an overall negative value of $\Delta\Delta E_{1+4}$.

Figure 5.5 shows the relative free energy of Pt, Pt₃Co, Pt₃Ni, Pt₃V, and Pt₄Rh alloys taking Pt as a reference for the first reduction step against the last three reduction steps. It is clearly shown that none of the studied model catalyst surfaces has the ability to reduce oxygen as pure Pt. All the catalysts have either positive values of $\Delta\Delta E_1$ and $\Delta\Delta E_4$ or a mix of positive and negative values for $\Delta\Delta E_1$ and $\Delta\Delta E_4$. In order to be considered a better catalyst than Pt, the catalyst must be on the quadrant with negative values of both $\Delta\Delta E_1$ and $\Delta\Delta E_4$. It is observed that most of them are on quadrants with either positive values of $\Delta\Delta E_1$ and negative values of $\Delta\Delta E_4$ (skin Pt monolayer catalysts of Pt₄Rh, Pt₃Ni, Pt₃Co, and Pt₃V) which favor the reduction of OH and O to water or negative values of $\Delta\Delta E_1$ and positive values of $\Delta\Delta E_4$ (Pt₄Rh, Pt₃Co, and Pt₃V) which favor the formation of M-OOH (however they do not promote the reduction of O and OH to water in the last three electron and proton transfer steps).

Table 5.5

Relative free energies (eV) according to equations 1.3 and 1.6 for Pt, Pt₃Co, Pt₃Ni, Pt₃V, and Pt₄Rh alloys with respect to pure Pt

	Case	$\Delta\Delta E_1$	$\Delta\Delta E_2$
Pt		0.00	0.00
Pt ₃ Co (Skin Pt)	A	0.26	-0.66
Pt ₃ Co	B	-0.01	0.59
Pt ₃ Ni (Skin Pt)	A	0.21	-0.52
Pt ₃ Ni	B	0.08	0.27
Pt ₃ V (Skin Pt)	A	0.44	-0.96
Pt ₃ V	B	-0.28	3.74
Pt ₄ Rh (Skin Pt)	A	0.16	-0.06
Pt ₄ Rh	B	-0.20	0.68

According to thermodynamic guidelines for the design of OOR alloy catalysts^[26; 59], which are based on information of pure metal catalyst behavior toward the ORR; a good candidate to catalyze the ORR better than Pt must have both $\Delta\Delta E_1 < 0$ and $\Delta\Delta E_4 < 0$. Thus, none of these cases satisfy the two criteria, however we can expect that some of the studied skin Pt monolayer model catalyst surfaces can behave at least comparably to pure Pt. That is the case of skin Pt/Pt₄Rh, skin Pt/Pt₃Ni, and skin Pt/Pt₃Co. For example, OOH binds on Pt/Pt₄Rh with a binding energy of -0.93 eV, very close to the one found in Pt (-1.08 eV). And atomic oxygen and hydroxyl binding energies are -3.91 and -2.22 eV compared to -3.92 and -2.27 eV in pure Pt; the free energy profile for Pt₄Rh (skin Pt) is shown in Figure 5.6.

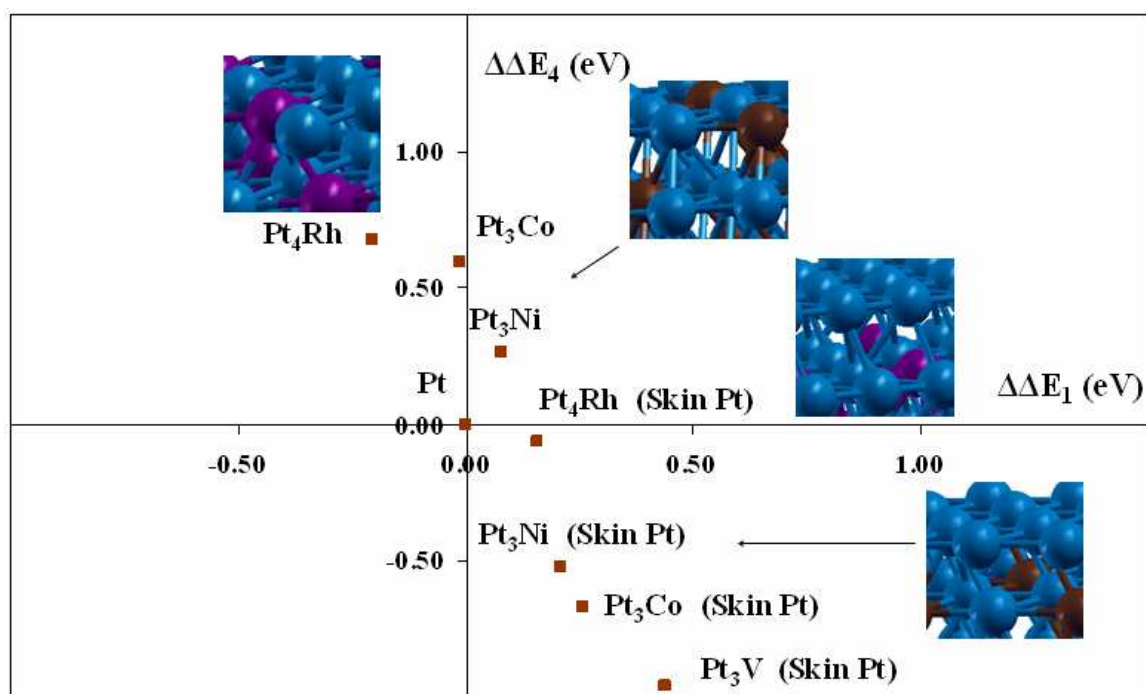


Figure 5.5. Relative energies (eV) according to equations 1.3 and 1.6 for Pt, Pt₃Co, Pt₃Ni, Pt₃V, and Pt₄Rh alloys with respect to pure Pt.

Nevertheless skin Pt/Pt₃V has the lowest $\Delta\Delta E_4$, it should be expected to have serious problems to dissociate the OOH radical into OH and O on the surface due to its relative high $\Delta\Delta E_1$ (0.44 eV) compared to the other cases.

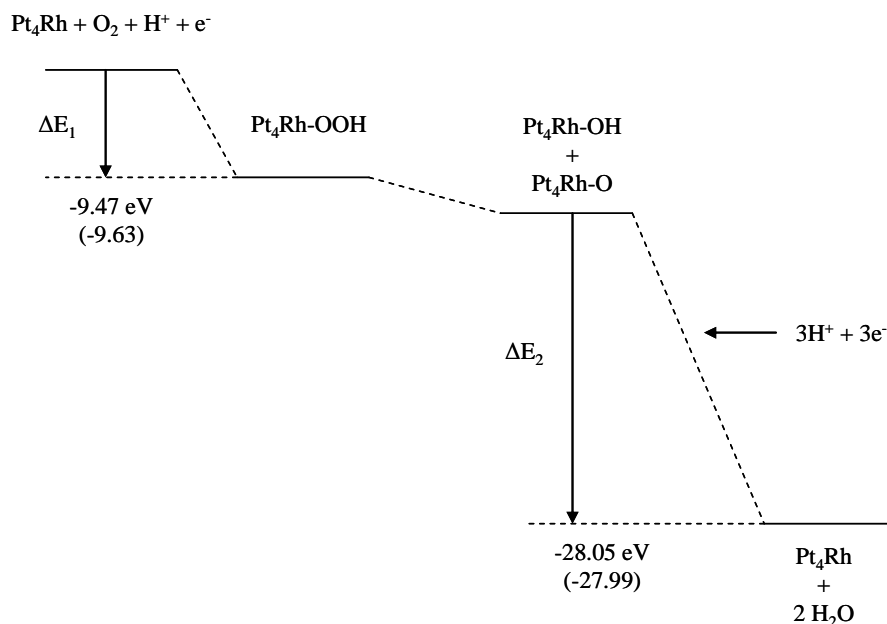


Figure 5.6. Gibbs free energy profile for the ORR on Pt₄Rh (skin Pt). The data in parenthesis are for pure Pt.

Correlation Between the Surface d-band Center and the ORR Intermediates

In this section the d-band center (Figure 5.7) and the surface d-band center (Figure 5.8) of the slab cluster for Pt, Pt₃Co, Pt₃Ni, Pt₃V, and Pt₄Rh (cases A and B) are computed. It was found a linear relationship between the calculated surface d-band center for the studied slab catalysts and the binding energy of OOH, hydroxyl and atomic oxygen. It is noticed however that the d-band center values do not follow the same trend. M. Shao et al. ^[40] and Norskov ^[97] showed a correlation between the d-band center values and the binding energy of atomic oxygen, and at the same time this trend is related to the reactivity of the catalyst.

In Figure 5.7 it is observed that the d-band center values of cases A (skin Pt monolayer) and B (homogeneous distribution) for each of the model catalyst surfaces are close in magnitude, having the skin Pt monolayer the lower values. The d-band center

values for Pt₄Rh, Pt₃Co, Pt₃Ni, and Pt₃V are -2.11, -1.99, -1.95, and -1.88 eV respectively whereas the corresponding d-band center values for their Pt skin monolayer catalyst are -2.12, -2.02, -1.98, and -1.92 eV. The d-band center value for pure Pt is -2.16 eV.

In Figure 5.8 is particularly interesting to observe the trend of the surface d-band center and the binding energies for OOH, OH, and O. We found that the smaller absolute value of the surface d-band center (meaning that the d-band center is closer to the Fermi level, i.e. more reactive the surface), the stronger adsorption of the intermediates on the catalyst surface.

Nevertheless the reduction of the interaction distances between the metals on the surfaces due to the reduction of the lattice constant increases the interaction of all the intermediates, and somehow favors the first electron and proton transfers (equation 1.3), at the same time this effect is translated into a different effect for the last electron and proton transfers (equation 1.6); increasing the interaction of the adsorption of both the hydroxyl and the atomic oxygen intermediates. This evidence is in agreement with M. Shao et al ^[40], who found that the maximum enhancement in the electroactivity of the ORR for Pd monolayer catalyst is located at an intermediate point along the d-band center of the catalysts, demonstrating that a good catalyst should balance the effect in the d-band center considering not only atomic oxygen and hydroxyl adsorption but also the OOH intermediate adsorption. This trend causes that the correlation of the surface d-band center clearly separates the catalyst location for cases A and B based on their capacity to adsorb the intermediates. In this plot Pt is located exactly in the middle and Pt₄Rh, Pt₃Co, Pt₃Ni, and Pt₃V developing a gap around Pt for cases A and B.

In general it was observed that in both cases the surface d-band center and the d-band center are directly related with the atomic size of the metal alloy.

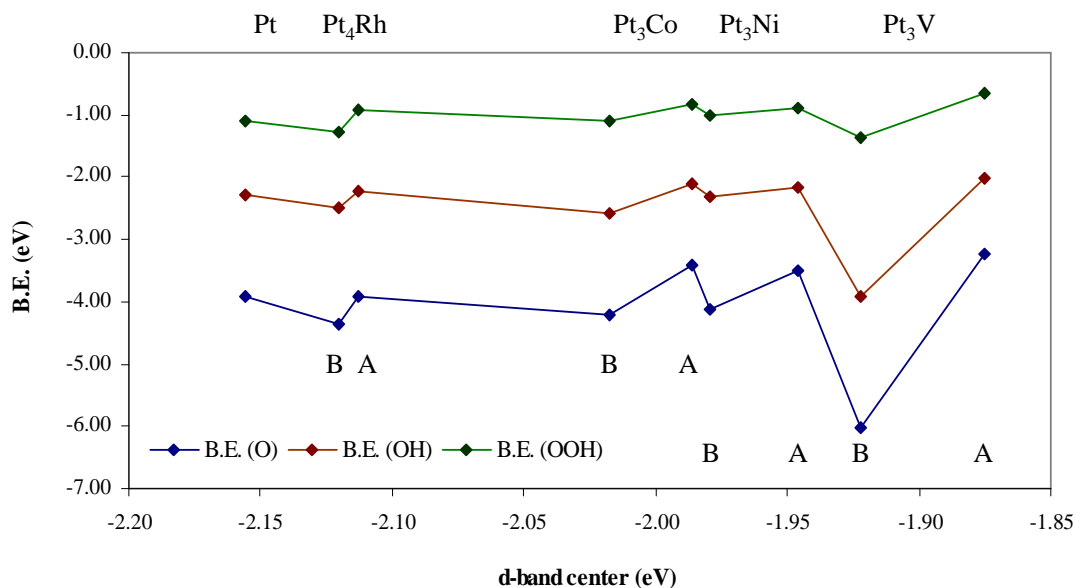


Figure 5.7. Binding energies of OOH, OH, and O as a function of the d-band center of the slab cluster for Pt, Pt₃Co, Pt₃Ni, Pt₃V, and Pt₄Rh (cases A and B).

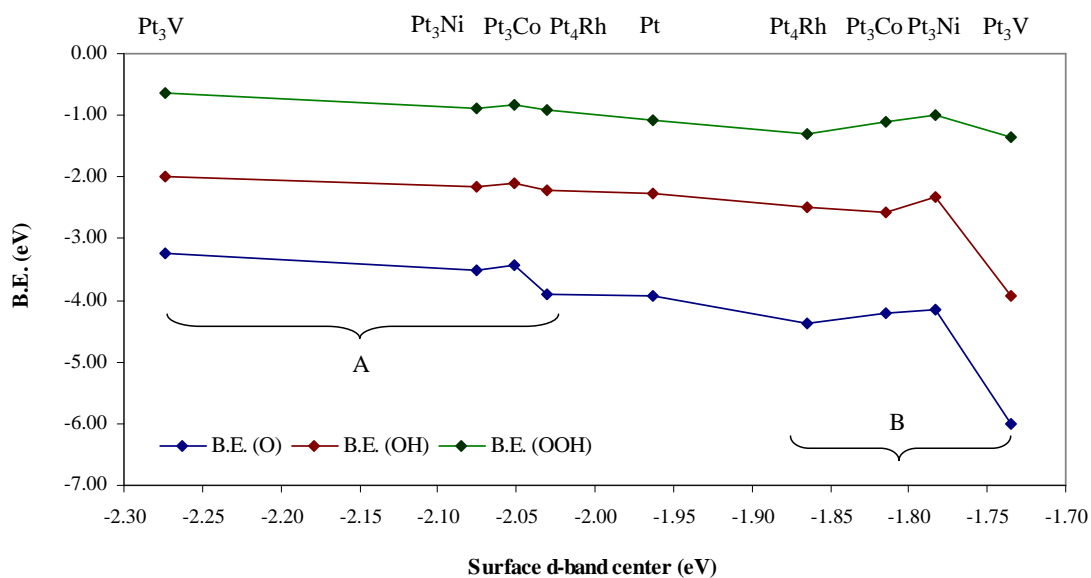


Figure 5.8 Binding energies of OOH, OH, and O as a function of the surface d-band center of the slab cluster for Pt, Pt₃Co, Pt₃Ni, Pt₃V, and Pt₄Rh (cases A and B).

Summary

None of the studied catalysts yield both negative values of $\Delta\Delta E_1$ and $\Delta\Delta E_4$. However skin Pt monolayer of Pt₃Co, Pt₃Ni, and Pt₃V catalysts provide an overall negative value of $\Delta\Delta E_{1+4}$, and they should act at least in a similar way than pure Pt. The order of the reactivity based on the overall relative free energy is for the ORR is: Pt₃V (skin Pt) > Pt₃Co (skin Pt) > Pt₃Ni (skin Pt) > Pt > Pt₄Rh (skin Pt). This behavior is attributed to the polarization of the slab caused by the charge density distribution, which is also reflected in the separation of the atoms in the surface (first layer) and the substrate. All skin Pt monolayer model catalyst surfaces facilitate the reduction of OH an O to water (last three electron and proton transfer), and nevertheless they do not favor the formation of M-OOH in the same way of Pt (they all have $\Delta\Delta E_1 > 0$), most of them (skin Pt/Pt₃Co, skin Pt/Pt₃Ni, and skinPt/Pt₃V) have $\Delta\Delta E_{1+4} < 0$, suggesting that they could be used to catalyze the ORR, especially skin Pt/Pt₃Co and skin Pt/Pt₃Ni; both have similar strength to adsorb OOH, -0.83 and -0.88 eV for skin Pt/Pt₃Co and skin Pt/Pt₃Ni respectively compared to -1.08 eV of Pt. We also found that once any of the metal alloy elements is present on the surface the catalyst, they behave in a different way, the catalyst favors the formation of M-OOH, but at the same time it does not facilitate the reduction of O and OH into water. On the contrary, it adsorbs strongly the hydroxyl and especially the atomic oxygen making difficult their reduction to water.

A correlation between the surface d-band center and the binding energy of the OOH, OH, and O intermediates was observed. They basically follow the same trend, the stronger adsorption of the intermediate the lower value for the surface d-band center.

CHAPTER VI

CHEMICAL REACTIVITY IN STEPPED PT AND PT-NI SURFACES

Introduction

In this chapter we extend the study of the reactivity of homogeneous, low Miller index surfaces to heterogeneous, stepped, high Miller index surfaces. Since most of catalytic reactions are structure sensitive due to the presence of step and kink sites, the under coordinated surface atoms and the changes of the electronic density of the surface, we explore the reactivity sensitivity of the ORR on these surfaces in terms of chemisorption of the ORR intermediates and the changes in the d-band structure. We evaluate the electrocatalytic activity in stepped surfaces (211), and then we explore the sensitivity of the atomic oxygen adsorption on Pt(320) and Pt(331). Pt(211) surfaces can be classified in surfaces with (111) terraces separated by monatomic (100) steps. In the same way Pt(331) consists of (111) terrace and (111) step, and Pt(320) has a (110) terrace and (100) step. Pt(211), Pt(331) and Pt(320) surfaces can also be denoted as Pt[3(111)(100)], Pt[3(111)(111)], and Pt[3(110)(100)] respectively.

To explore the reactivity in (211) surfaces we chose two cases, Pt and skin Pt monolayer over Pt₃Ni. We used skin Pt monolayer catalysts since it has been shown in previous chapters that this kind of model catalyst surfaces are the most suitable for the ORR, not only in terms of reactivity, but also in terms of stability. This last point will be addressed in the next chapter.

The (211) surfaces were modeled using a 3x2 supercell. The Pt(211) and the Pt/Pt₃Ni(211) catalyst systems were described using a 4-layer periodic slab model, where each slab was infinite in the x and y directions, while finite along the z direction, and then repeated periodically along all the directions. For each relaxation process, the first two layers on the top are allowed to relax, while the two at the bottom are fixed. A vacuum space equivalent to eight layers was used to ensure that there were no interaction between the adsorbed intermediates and the bottom surface of the next slab. In all the calculations, the obtained bulk lattice constant was used.

In order to compute the reactivity for these cases, we used the most stable conformation only for the adsorption of the ORR intermediates (OOH, OH, and O). The overall coverage used for these cases is 1/6 monolayer (ML). Table 6.1 lists the detailed information of the binding energy values taking as a reference positions sketched in Figure 6.1. It was found that the intermediates adsorbed stronger mostly in bridge step sites (in Pt/Pt₃Ni(211) the hydroxyl radical adsorbs in hollow sites).

Thermodynamic Reactivity of Pt(211) and Pt₃Ni (211) Catalysts

After testing all possible adsorption sites in the (211) surface based on the sketch of Figure 6.1, we found that all the intermediates tend to adsorb strongly on bridge positions on step sites (position 1) while the interactions in terrace sites (positions 2 and 3) are less stronger. This effect can be explained in terms of the low coordination number at the step sites, which leads to the redistribution of the electron charge density. The strength of adsorption on step sites considerably overpass the strength on (111) surfaces. The OOH adsorption on Pt(211) has a binding energy of -1.91 eV while the binding energy on Pt (111) is -1.08 eV. The same trend is found for the other intermediates. On Pt model (211) catalyst surfaces OH and O adsorb with 38% and 14% more strength respectively than in the most stable sites of the (111) surface (these values can be observed in Table 6.1).

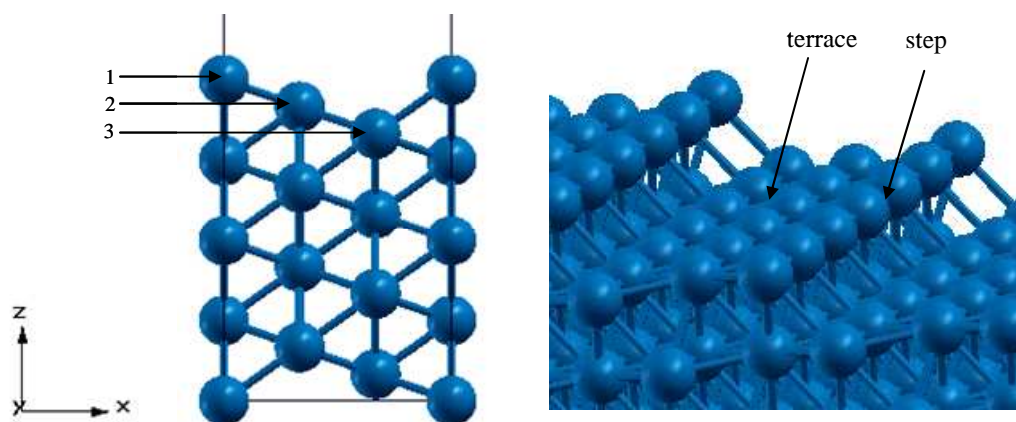


Figure 6.1. Extended surface (211) approach. Left: The unit cell includes 26 metal atoms and the vacuum space. Right: Lateral view of the surface. 1: step site, 2 and 3: terrace sites.

From Table 6.1 the role of the metal alloy in the substrate is also observed, which causes the reduction of the interaction strength between the intermediates and the catalyst surface. For example the binding energy of OOH on Pt(211) is -1.91 eV while the binding energy on Pt/Pt₃Ni(211) is -1.59 eV.

Table 6.2 shows a comparison between the relative free energies for reactions 1.3 and 1.6 on Pt and Pt/Pt₃Ni (111) and (211) surfaces while Table 6.3 shows some the structural characteristics after the adsorption of OOH, OH, and O on these surfaces. From the results it is clear that the (211) surface does not enhance the ORR activity compared to the same composition on a (111) surface. Nevertheless, (211) surfaces favor the first electron and proton transport due the strong interaction between the OOH intermediate and the surface in step sites, at the same time they also increase the adsorption of the intermediates involved in the reduction to water, which makes these type of surfaces less suitable for the reduction of oxygen. In a recent study ^[114] it was found however that stepped Pt surfaces enhance the catalytic activity of the ORR. It is stated that the ORR in acid media is a structure sensitive reaction that is affected by the

anion adsorption and the oxide formation, whereas the oxygen adsorption energies on the different sites play a secondary role in determining the catalytic activity of the electrode. The high activity of the stepped surfaces is attributed to the formation of a less stable (bi)sulfate adlayer compared to that formed on Pt(111). This explanation may be explored in future work for a better understanding of the ORR performance on stepped surfaces.

The computed local density of states shows a shift of the d-band center to positive energy values, which suggests an increased reactivity of this surface. The computed d-band center for Pt(211) is -1.90 eV whereas for Pt(111) is -2.16 eV. This change is also reflected in the strong interaction between Pt(211) surfaces and the ORR intermediates compared to the ones found on Pt(111).

In general terms, the comparison between (111) and (211) surfaces shows the important site structure sensitivity for the chemisorption in stepped surfaces. It is also noticed that surfaces (211) are also sensitive to the presence of the alloy metal in the substrate; in particular to the adsorption of OH and O.

Table 6.1

Binding energies (BE, in eV) of OOH, OH, and O on Pt and Pt/Pt₃Ni.

BEs calculated as: $BE_{\text{slab-adsorbate}} = E_{\text{slab+adsorbate}} - E_{\text{slab}} - E_{\text{adsorbate}}$

Catalyst	B.E. (OOH)	B.E. (OH)	B.E. (O)
Pt (111)	-1.08	-2.27	-3.92
Pt (211)	-1.91	-3.13	-4.45
Skin Pt/Pt ₃ Ni (111)	-0.88	-2.16	-3.51
Skin Pt/Pt ₃ Ni (211)	-1.59	-2.38	-4.49

Table 6.2

Relative free energies (eV) according to equations 1.3 and 1.6 for Pt and Pt/Pt₃Ni with respect to pure Pt

Catalyst	$\Delta\Delta E_1$	$\Delta\Delta E_4$
Pt (111)	0.00	0.00
Pt (211)	-0.83	1.40
Skin Pt/Pt ₃ Ni (111)	0.21	-0.52
Skin Pt/Pt ₃ Ni (211)	-0.51	0.68

Table 6.3

Distances (in Å) for adsorption of oxygenated species on Pt and Pt/Pt₃Ni(211). Atomic oxygen, hydroxyl and OOH adsorbed on bridge sites

	Pt (111)	Pt (211)	Skin Pt/Pt ₃ Ni (111)	Skin Pt/Pt ₃ Ni (211)
M-OOH d _{O-O}	1.430	1.464	1.423	1.466
M-OOH d _{M-O}	2.037	2.100 (2)	2.038	2.099(2)
M-OH d _{M-O}	2.002	2.126 (2)	2.006	2.066
M-O d _{M-O}	2.042	1.941 (2)	2.041, 2.040 , 2.033	1.943 (2)

Atomic Oxygen Adsorption on Pt(111), Pt(211), Pt(331), and Pt(320)

As it was observed in the previous section, the reactivity of any specific catalyst is directly related to the adsorption of the intermediates on the surface. It was detected that the reactivity of the ORR is favored by a moderate atomic oxygen interaction with the surface. Therefore, we can use this criterion to suggest the best stepped catalyst for the ORR. In this section we evaluate the adsorption of atomic oxygen on Pt(111), Pt(211), Pt(331), and Pt(320) to evaluate the interaction of this specie with the model catalyst surface.

Figure 6.2 shows the atomic oxygen binding energies on Pt(111), Pt(211), Pt(331), and Pt(320). We included the values for all possible adsorption sites on the

catalyst surfaces. In general, it was found that the most stable conformations correspond to either hollow or bridge sites (Figure 6.3). It is particularly interesting to see that among all cases and comparing only the most stable adsorption conformations that atomic oxygen is adsorbed weaker on Pt(111) than on the stepped surfaces. Atomic oxygen adsorbs to the surface with binding energies of -3.92, -4.32, -4.40, and -4.50 eV for Pt(111), Pt(331), Pt(320), and Pt(211) respectively. From these results we should expect that all stepped surfaces should have problems to reduce atomic oxygen from the surface due to strong adsorption, therefore they should work less efficiently than Pt(111) in the ORR.

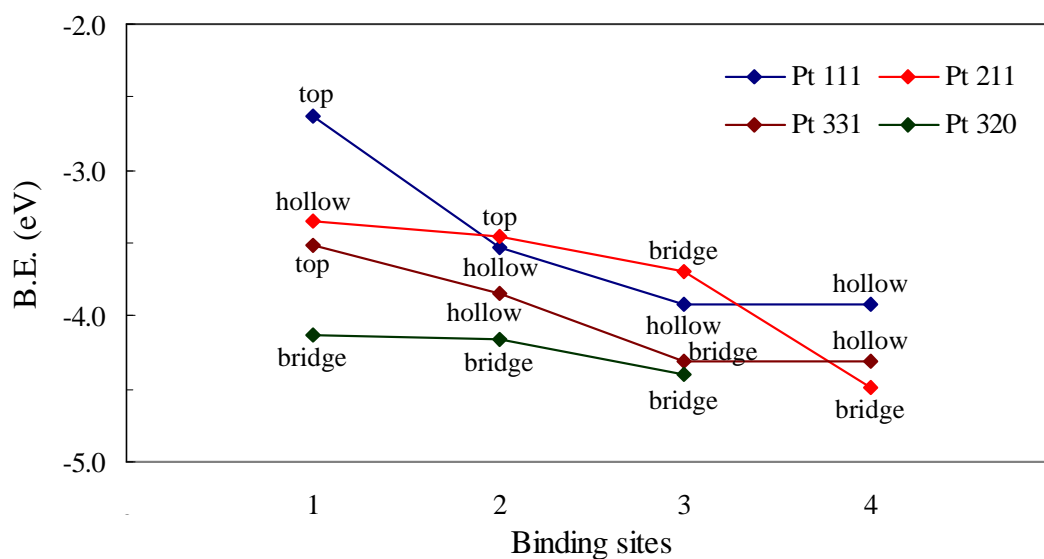


Figure 6.2. Binding energies (in eV) of atomic oxygen on Pt(111), Pt(211), Pt(331), and Pt(320) surfaces tested in different positions along the stepped surface.

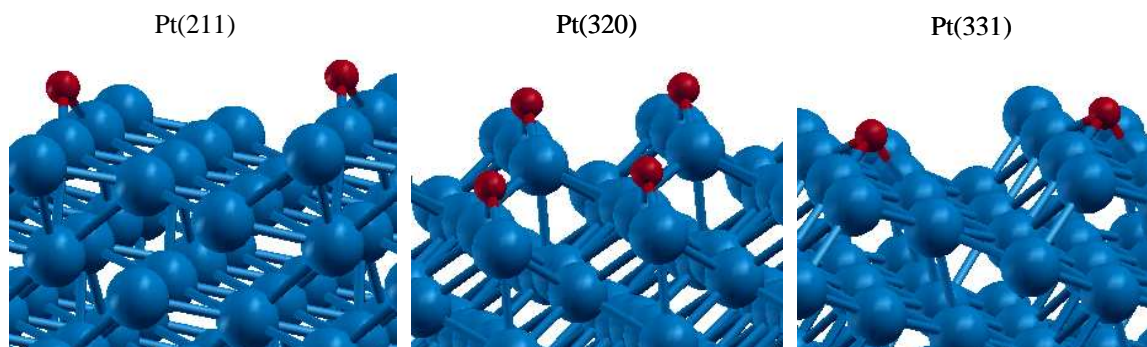


Figure 6.3. Adsorption of atomic oxygen on Pt(211), Pt(320), and Pt(331) surfaces.

Summary

In this chapter we analyze the reactivity of Pt and Pt₃Ni stepped surfaces. We found that in terms of adsorption energies none of the (211) surfaces enhances the catalytic activity of the ORR compared to Pt(111). On the other hand they may offer good sites for anion adsorption. It is also detected that the presence of the alloy metal in the substrate favors the reduction of OH and O.

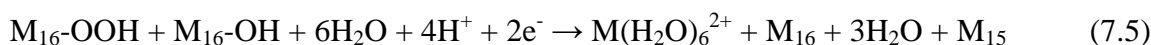
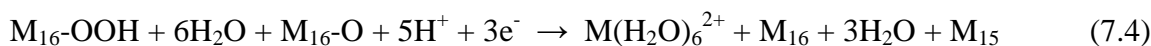
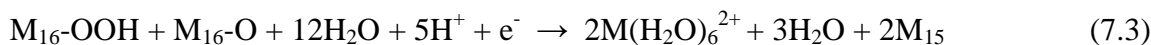
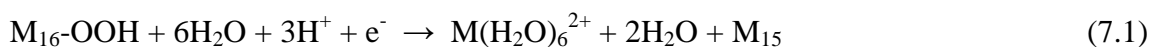
The changes in the local density of states of stepped surface surfaces implied remarkable changes in the electronic structure; this effect is translated into the shift of the d-band center to positive energy values.

We also compared Pt(111), Pt(331), Pt(320), and Pt(211) surfaces, and we found that among all these surfaces Pt(111) is the most suitable catalyst for the ORR mainly because of the its moderate adsorption of the ORR intermediates that allows the reduction of them.

CHAPTER VII
CHEMICAL STABILITY OF PT₃CO, PT₃NI, PT₃PD, AND PT₄RH ALLOY
CATALYSTS

Introduction

In this section, we analyze the chemical stability of the Pt₃Co, Pt₃Ni, Pt₃V, and Pt₄Rh alloy catalysts against the dissolution in acidic environment measuring the free energy changes of allowed dissolution reactions considering the presence of some intermediates of the ORR. As a starting point based on previous work performed by Balbuena and Gu we selected thermodynamic allowed dissolution reactions ^[115] to evaluate the stability on Pt and Pt alloy model surfaces. The reactions that are thermodynamically favorable are electrochemical and involve interactions of the ORR oxygenated intermediates (OOH, OH, and O) with the catalyst surface and solvated proton molecules coming from the acid electrolyte. Balbuena and Gu also tested some chemical dissolution reactions, demonstrating that these type of reactions are thermodynamically unfavorable. The following are the electrochemical dissolution reactions used in this study:



where M_{16} represents the 2x2 four layer periodic slab for Pt, Pt₃Co, Pt₃Ni, Pt₃V, and Pt₄Rh catalyst surfaces. As it is shown for the set of reactions, the dissolution of one of two M atoms from the surface leads to the formation of hydrated metal cations, $M(H_2O)_6^{2+}$. And in order to approximate the condition of hydrated protons present in the acidic environment, the protons are modeled as $H_3O^+(H_2O)_3$; for protons the inner shell may be conceived as the three water molecules solvating H_3O^+ [87; 88] (the H_3O^+ ion itself is similar in diameter to K^+ and both have similar solvation energies). On the other hand the hydrated metal cation (M^{2+}) is modeled as $M(H_2O)_6^{2+}$ because six-coordinate complexes of transition metals are commonly formed in acid medium [116].

The free energy change ΔE for each reaction is calculated as the difference between the free energy of the products and the reactants as it is shown for reaction 6.1:

$$\Delta E_1 = E[M(H_2O)_6^{2+}] + 2E[H_2O] + E[M_{15}] - E[M_{16}-OOH] - 6E[H_2O] - 3E[H^+] - U(e^-) \quad (7.6)$$

In each electrochemical reaction, the electron energy is set to zero, which corresponds to a zero cell potential ($U = 0$ V).

We also evaluate the relative free energy $\Delta\Delta E$ of these reactions respect to the free energy changes for pure Pt catalyst using the following correlation:

$$\Delta\Delta E_{\text{rxn}}(M) = \Delta E_{\text{rxn}}(M) - \Delta E_{\text{rxn}}(\text{Pt}) \quad (7.7)$$

In this way we could reduce the errors arising from the modeling of the extended metal systems. It is pointed out that these calculations have a qualitative character since the metal dissolution of the electro-catalyst under real conditions would depend on many different variables such us the kind of the metal catalyst, potential, scan rate, temperature, solution concentration, composition, etc.

Thermodynamic Trends of the Dissolution of Pt, Co, Ni, and Rh on Pt and Pt-X (X: Co, Ni, Pd, and Rh) Catalysts

In this section we study how the presence of Pt atoms on the surface catalyst can alter the dissolution of Co, Pd, Ni, and Rh in homogeneous surface distributions of Pt:X (3:1) (X: Pt, Co, Ni, Pd, and Rh). In earlier investigations^[42; 115; 117], it was shown that Pt atoms are more stable than elements from the Group VIII (Co, Ni, Rh, and Pd) coming from rows four and five of the periodic table.

As it is shown in reactions 7.1-7.5, all dissolution reactions involve interactions of the ORR intermediates OOH, OH and O with the catalyst surfaces. We evaluate the dissolution of Pt, Co, Ni, Pd, and Rh respectively. In order to achieve realistic values for the ΔE s, we considered the energy values for the most stable conformations only.

In agreement with Balbuena and Gu^[115] we found that all the electrochemical reactions used in this study are thermodynamically favorable. Table 7.1 lists the values for all the free energy changes of reactions 7.1-7.5 for Pt, Pt₃Co, Pt₃Ni, Pt₃Pd, and Pt₄Rh. From Table 7.1 it is noticed that reaction 7.4 has the highest negative value of ΔE for all the considered dissolution reactions. This reaction also involves the highest number of electron transfer (three).

Table 7.1

Free energy changes ΔE (eV) for Pt, Co, Ni, Pd, and Rh dissolution in Pt, Pt₃Co, Pt₃Ni, Pt₃Pd and Pt₄Rh surface catalysts for reactions 7.1-7.5

	Pt	Pt₃Co	Pt₃Ni	Pt₃Pd	Pt₄Rh
ΔE_1	-46.094	-47.926	-50.002	-48.913	-48.222
ΔE_2	-44.838	-46.088	-48.329	-47.496	-46.490
ΔE_3	-68.355	-71.735	-75.785	-73.515	-72.367
ΔE_4	-90.927	-92.462	-94.619	-93.613	-92.607
ΔE_5	-68.671	-70.492	-72.526	-71.390	-70.832

Figure 7.1 shows the relative free energy changes $\Delta\Delta E$ for the dissolution reactions 7.1-7.5 of Co, Ni, Pd, and Rh with respect to Pt in Pt₃Co, Pt₃Ni, Pt₃Pd, and Pt₄Rh respectively. We found that Co, Ni, Pd, and Rh are more easily dissolved than Pt, which is deduced by the negative values of the $\Delta\Delta E$. The free energy changes for Ni is ~3.5 eV more negative than Pt for reaction 7.1, 7.2, 7.4, and 7.5 while reaction 7.3 is 7.43 eV more negative than Pt. It is pointed out that reaction 7.3 describes the dissolution of two hydrated cation molecules $X(H_2O)_6^{2+}$ (X: Pt, Co, Ni, Pd, and Rh). From all the model catalyst surfaces studied, Ni was found to be the less stable metal atom on the surface. We found that the order of stability of the Pt, Co, Ni, Pd, and Rh in Pt₃Co, Pt₄Rh, Pt₃Pd, and Pt₃Ni catalyst surfaces is: Pt > Co > Rh > Pd > Ni respectively. The results are in agreement with Juodkazis et al. in the investigation of the dissolution of Pd^[118] and Rh^[119] in 0.5 M H₂SO₄, finding that during the potential cycling through the oxygen region the electrode mass decreases which each cycle as a indication of the metal dissolution. Lukaszewski and Czerwinski^[117] also reported the dissolution of Pd, Rh and Pt-Pd, finding that Pd and Rh are less stable than Pt, and that Rh is more stable than Pt along the potential under experimental conditions. The trend found in this part is close to what is found in pure catalysts^[115], however Co is more stable than Rh and Pd, suggesting that the stability of metal atoms in the catalyst surface are altered by the changes in the electronic distribution on the surface after a pure element is alloyed.

The dissolution of alloy metals from Group VIII was also investigated by Greeley and Norskov^[120], they found trends between metal dissolution potentials and surface segregation energies. The more strongly a metal segregates to the surface of a particular host, the more stable the metal will be in a given surface. The increase in the stability of the surface, translates into the increase resistance to the dissolution. This concept can not be applied when the heat of the dissociation of the metal solute in the bulk host is large. However it can be applied for Co, Ni, Pd, and Rh with anti-segregation energies^[108] in Pt host, which is translated into a tendency for the dissolution on Pt catalysts.

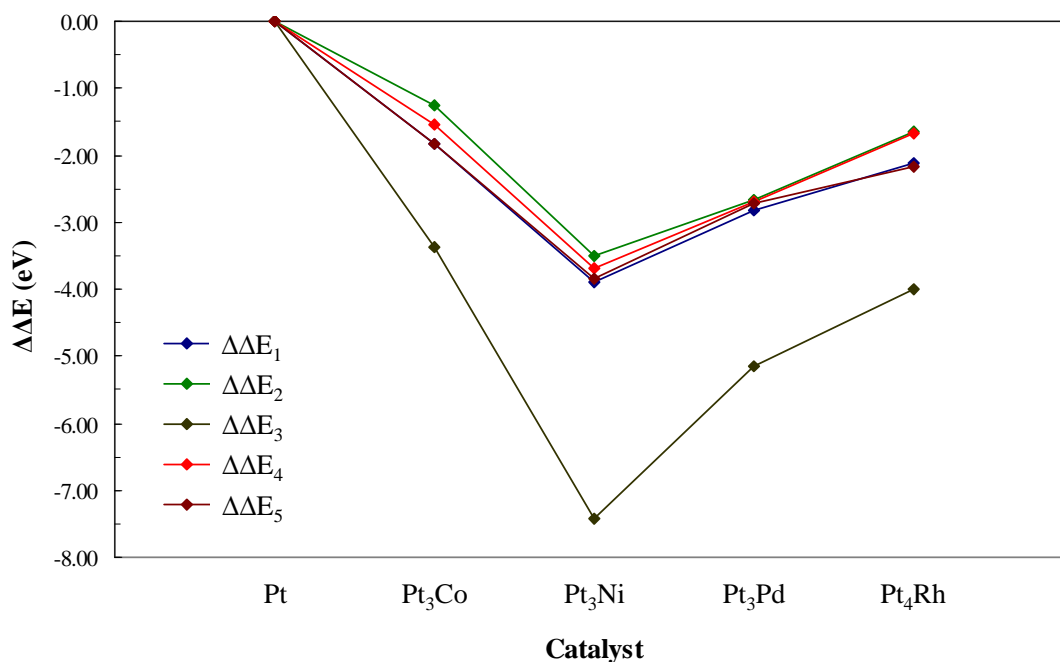


Figure 7.1. Relative free energies of reactions 7.1-7.5 with respect to Pt for the dissolution of Pt, Co, Ni, Pd, Rh atoms from the model catalyst surfaces of pure Pt, Pt₃Co, Pt₃Ni, Pt₃Pd, and Pt₄Rh.

Thermodynamic Trends of Pt Dissolution on Pt and Pt-X (X: Co, Ni, Pd, and Rh) Catalysts

In this section we study the tendency of Pt dissolution from catalysts with homogeneous surface distributions of Pt:X (3:1) (X: Pt, Co, Ni, Pd, and Rh). We explore the effect of the alloy metal on the stability of Pt atoms.

As in the previous case and also in agreement with Balbuena and Gu^[115] we found that all the electrochemical reactions for the dissolution of Pt atoms from the homogeneous catalyst surface are thermodynamically favorable. Table 7.2 lists the ΔE values for reactions 7.1-7.5 for Pt, Pt₃Co, Pt₃Ni, Pt₃Pd, and Pt₄Rh. From Table 7.2 it is noticed that among all the favorable dissolution reactions, reaction 7.4 has the highest negative value,

which indicates that the more electrons involved the higher equilibrium constant of the associated reaction. This fact is in agreement with a similar trend found in previous work [115].

Table 7.2

Free energy changes (eV) for Pt dissolution in Pt, Pt₃Co, Pt₃Ni, Pt₃Pd and Pt₄Rh catalysts for reactions 7.1-7.5

	Pt	Pt₃Co	Pt₃Ni	Pt₃Pd	Pt₄Rh
ΔE_1	-46.094	-46.023	-46.155	-46.214	-45.846
ΔE_2	-44.838	-44.422	-44.549	-44.714	-44.220
ΔE_3	-68.355	-67.879	-68.179	-68.450	-67.456
ΔE_4	-90.927	-90.559	-90.772	-90.914	-90.232
ΔE_5	-68.671	-68.302	-68.679	-68.691	-68.192

Figure 7.2 shows the relative free energy changes $\Delta\Delta E$ for Pt dissolution reactions 7.1-7.5 of Pt in Pt, Pt₃Co, Pt₃Ni, Pt₃Pd, and Pt₄Rh catalysts. We observe that all the $\Delta\Delta E$ values for Pt₃Co and Pt₃Rh are positive, which means that Co and Rh improve the Pt stability on the surface. On the other hand positive and negative $\Delta\Delta E$ values for Pt₃Ni were found for reactions 7.2-7.4 and 7.1 and 7.5 respectively. In a similar way for Pt₃Pd, reactions 7.2 and 7.4 have positive $\Delta\Delta E$ values and reactions 7.1, 7.3, and 7.5 have negative $\Delta\Delta E$ values. The small $\Delta\Delta E$ values for Pt₃Ni and Pt₃Pd, especially Pt₃Pd that has values close to zero, suggest that Pd and Ni atoms on the surface could barely affect the stability of Pt surface atoms.

On the other hand, the positive $\Delta\Delta E$ values for Pt₃Co, Pt₃Ni, and Pt₄Rh catalysts suggest that Co, Ni, and Rh (especially Rh) help to stabilize Pt atoms on the surface. In general, from all the catalyst surfaces studied in this section, Pt atoms are not likely dissolved by the presence of the electrolyte. And in terms of stability we can state that the stability of Pt is favored by the presence of the alloy metals in the following order: Rh > Co > Ni > Pd. This order follows the trend of the cohesive energies of the alloy metals as it has been reported both from experimental ^[121] and theoretical works ^[122; 123], suggesting a correlation between the stability of Pt atoms on the surface and the cohesive energy of the alloy metal surrounded by Pt atoms on the surface. This relationship can be understood intuitively. The stronger cohesive energy of the alloy metal, the more stability the catalyst surface acquires against dissolution. It is pointed out that although the presence of metal alloys on the surface stabilize the Pt atoms in the surface, the effect on them is not significant, and for some cases it could be negligible based on the small $\Delta\Delta E$ values which in most of the cases are around 0.5 eV.

In summary from the previous two sections, we can conclude that in all Pt-X homogeneous catalyst surfaces, the alloy metal most likely be dissolved from the surface forming a skin Pt monolayer as it was reported previously in experimental studies ^[9; 33; 42; 43] under practical operational conditions even in dilute acid solutions. In the next section we will explore the stability of skin Pt monolayer catalysts.

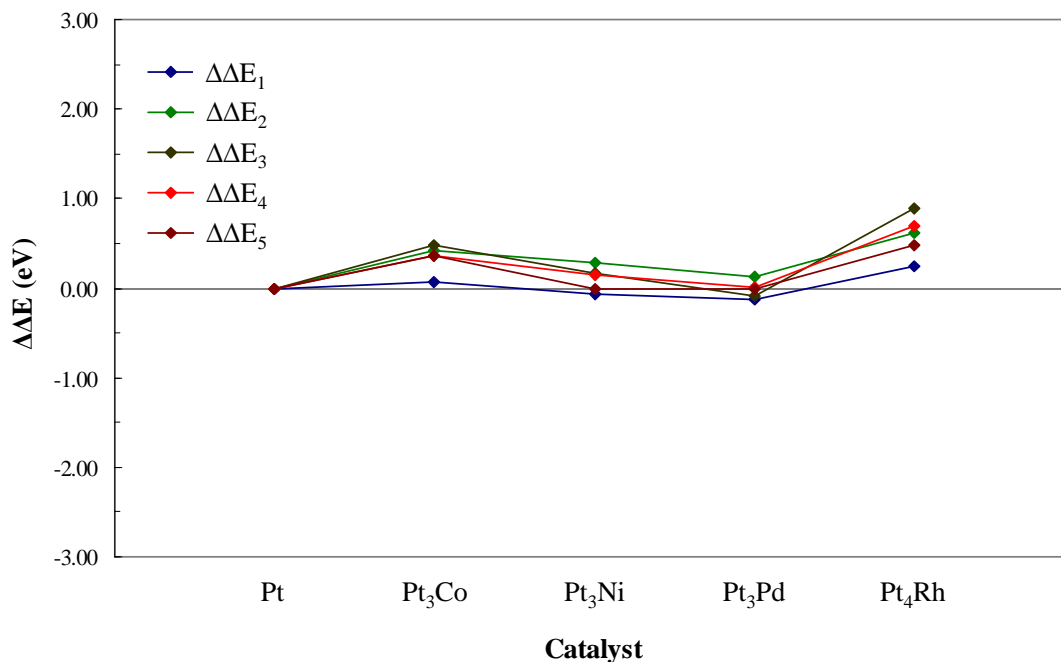


Figure 7.2. Relative free energies with respect to Pt for reactions 7.1-7.5 for the dissolution of Pt atoms from the catalyst surfaces of pure Pt and Pt monolayers of Pt₃Co, Pt₃Ni, Pt₃Pd, and Pt₄Rh.

Thermodynamic Trends of Pt Dissolution on Pt and Skin Pt Monolayers of Pt₃Co, Pt₃Ni, Pt₃Pd, and Pt₄Rh Catalysts

In this section we evaluate the dissolution of Pt atoms from skin Pt monolayer catalysts of Pt₃Co, Pt₃Ni, Pt₃Pd, and Pt₄Rh. As it was demonstrated in the two previous sections Pt atoms are very stable against the dissolution in acid medium compared with typical alloy metals such as Co, Ni, Pd, and Rh. And even if one of these metals is present on the catalyst surface, it is most likely dissolved by the acid media forming a skin monolayer of Pt. For that reason it results very interesting and necessary to explore how the skin Pt monolayer behaves against the dissolution having alloy metals in the substrate.

In the same way as the two previous cases all the electrochemical reactions for the dissolution of Pt atoms from the skin Pt monolayer catalysts are thermodynamically favorable. Table 7.3 listed the ΔE values for reactions 7.1-7.5 for Pt, skin Pt₃Co, skin Pt₃Ni, skin Pt₃Pd, and skin Pt₄Rh. From Table 7.3 it is noticed that among all the favorable dissolution reactions, reaction 7.4 has the highest negative ΔE value, which indicates that the more electrons involved the higher equilibrium constant of the associated reaction.

Table 7.3

Free energy changes (eV) for Pt dissolution in Pt, skin Pt₃Co, skin Pt/Pt₃Ni, skin Pt/Pt₃Pd, and skin Pt/Pt₄Rh catalysts for reactions 7.1-7.5

	Pt	Skin Pt₃Co	Skin Pt₃Ni	Skin Pt₃Pd	Skin Pt₄Rh
ΔE_1	-46.094	-46.193	-46.197	-46.069	-46.180
ΔE_2	-44.838	-45.340	-45.253	-44.644	-44.823
ΔE_3	-68.355	-68.798	-68.761	-68.154	-68.379
ΔE_4	-90.927	-91.530	-91.439	-90.847	-91.024
ΔE_5	-68.671	-68.928	-68.886	-68.627	-68.805

Figure 7.3 shows the relative free energy changes $\Delta\Delta E$ for Pt dissolution reactions 7.1-7.5 from skin Pt₃Co, skin Pt₃Ni, skin Pt₃Pd, and skin Pt₄Rh model catalyst surfaces. We observed that Co, Ni, Pd, and Rh affect the stability of the surface Pt atoms in a small degree for most of the dissolution reactions. It is found that the $\Delta\Delta E$ for Pt₃Co, Pt₃Ni, and Pt₃Rh are negative, which means that Co, Ni, and Rh reduce the stability of Pt atoms on the surface. On the other hand it is observed that Pd atoms in the substrate of skin Pt₃Pd improve the stability of Pt atoms in the surface by a small amount that might be considered negligible since for most of the reactions the $\Delta\Delta E$ are in the order of 0.2 eV.

Pt₄Rh has positive $\Delta\Delta E$ values for all the dissolution reactions but reaction 7.2, and for all cases the $\Delta\Delta E$ values are close to zero. This is an indication that Rh atoms in the substrate of the skin Pt₄Rh barely affect the stability of Pt surface atoms. In terms of stability we found that skin Pt monolayer catalysts are favored by elements of the fifth row of the periodic table (Pd and Rh) in a different degree. The presence of Pd atoms in the substrate barely changes the stability of Pt atoms in the surface. On the other hand the elements of the fourth row (Co and Ni) reduce the stability of Pt atoms on the surface. These results provide insights about how the presence of alloy metal in the substrate may alter the electronic structure of the catalyst surface.

It is pointed out that although the stability of Pt atoms in the surface is affected by the presence of Co, Ni, Pd, and Rh atoms in the substrate, based on the order of magnitude of $\Delta\Delta E$ ($-0.60 \text{ eV} < \Delta\Delta E < 0.20 \text{ eV}$), their effect may be relatively small.

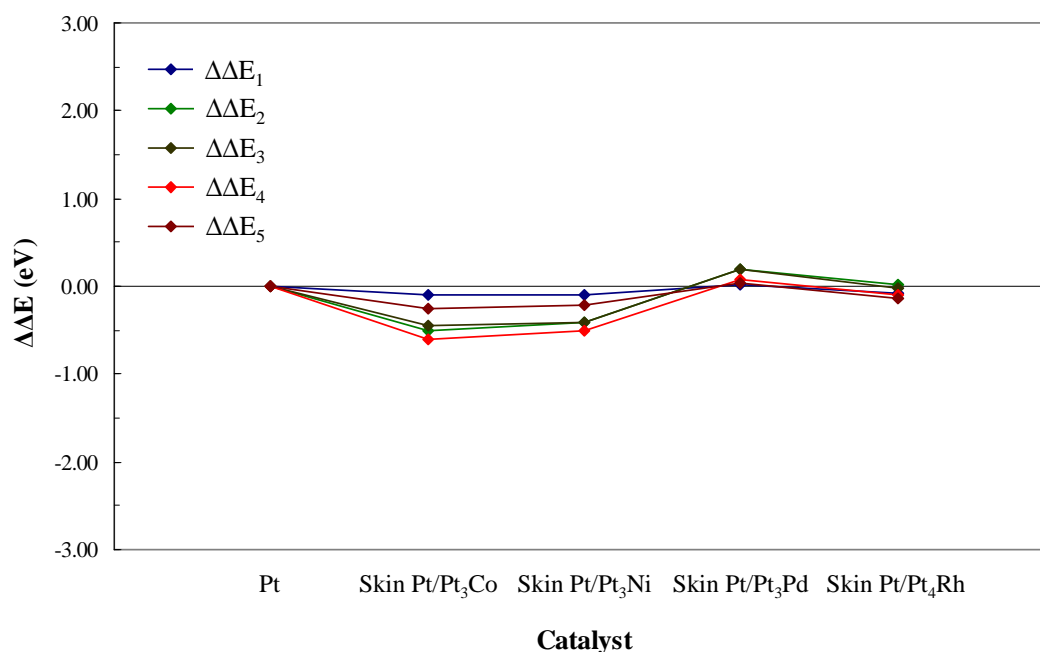


Figure 7.3. Relative free energies changes for reactions 7.1-7.5 for the dissolution of Pt atoms from the catalyst surface with respect to Pt in pure Pt and Pt skin monolayer of Pt₃Co, Pt₃Ni, Pt₃Pd, and Pt₄Rh model catalyst surfaces.

Composition and Atomic Distribution Effects on Catalyst Surface Stability

In order to analyze the stability of the metal surface atom as a function of composition we added an additional case of PtPd surfaces. An overall catalyst composition of Pt:Pd ratio 1:1 is used for this case in each of the four layers of the periodic slab. After computing the relative ΔE for reactions 7.1-7.5, it is found that there is no significance difference between the ΔE values for Pt₃Pd and PtPd catalysts, suggesting that the Pd atoms on the surface might dissolve at the same rate, but twice the amount of Pd atoms would be dissolved in the PtPd catalyst surface. Similar results were reported for PtNi, Pt₃Ni, PtCo, and Pt₃Co catalysts^[42]. In those cases both Co and Ni are dissolved at the same dissolution rate but clearly PtNi and PtCo dissolve more Ni and Co atoms from the catalyst surfaces.

Another interesting point to explore is the effect that the internal distribution in the substrate catalyst has over the stability of the catalyst surface. We have studied the skin Pt monolayer of Pt₄Rh model catalyst surfaces using two different layer by layer distributions. First, we used the original case of skin Pt₄Rh, which has a layer by layer distribution (from top to bottom) Pt:Rh 4:0 3:1 3:1 3:1. Then we used an additional Pt:Rh layer by layer distribution of 4:0 2:2 4:0 3:1. From the results it was noticed (not shown) that the ΔE values for the dissolution reactions 7.1-7.5 are almost the same. The difference between these cases is in the order of 0.1 eV. It is suggested that the internal distribution in the catalyst substrate does not alter significantly the electronic structure of the surface. Therefore, we should not expect a significant change in the dissolution characteristics of such catalyst surface.

Summary

In this chapter, periodic DFT methods have been applied to study the stability of Pt, Co, Ni, Pd, and Rh on Pt, Pt₃Co, Pt₃Ni, Pt₃Pd, and Pt₄Rh and their respective Pt monolayer catalysts. We evaluate the free energy changes using five different favorable electrochemical dissolution reactions. We found that the order of stability of Pt, Co, Ni, Pd, and Rh atoms in Pt₃Co, Pt₄Rh, Pt₃Pd, and Pt₃Ni catalyst is: Pt > Co > Rh > Pd > Ni

respectively. The trend found in this section is close to what is found in pure catalysts^[115], however Co is more stable than Rh and Pd, suggesting that the stability of metal atoms in the catalyst surface are altered by the changes in the electronic distribution on the surface after alloying. And in terms of stability surface Pt atoms are favored by the presence of surface alloy metals in the following order: Rh > Co > Ni > Pd. The positive $\Delta\Delta E$ values for Pt₃Co, Pt₃Ni, and Pt₄Rh catalysts suggest that Co, Ni, and Rh (especially Rh) promote the stabilization Pt atoms in the surface.

Based on the first two sections in this chapter, it was concluded that the most suitable catalysts in terms of stability against the dissolution for the ORR are the skin Pt monolayer catalysts. And the order of stability of skin Pt monolayer catalysts is: skin Pt₃Pd > Pt > skin Pt₄Rh > skin Pt₃Ni > skin Pt₃Co.

In addition we analyzed the effect of the overall composition of the catalyst toward the dissolution for Pt₃Pd and PtPd catalysts. We concluded that based on the negligible difference between the ΔE s values for Pt₃Pd and PtPd catalysts, Pd atoms on the surface should dissolve at a similar rate, but twice the amount of Pd atoms should be dissolved in the PtPd catalyst surfaces. Finally we study the substrate distribution effect on the stability of the atoms in the catalyst surface. The small ΔE s difference found for the dissolution reactions suggests little influence of the substrate composition on the dissolution of atoms from the first layer.

CHAPTER VIII

CONCLUSIONS AND RECOMMENDATIONS

The use of computational methods as a tool to analyze and compute important properties of chemical systems have experienced a fast development in recent years, among other reasons due to the development of fast and more efficient computer hardware, which can be extended from personal computers, through workstations and mainframe machines to supercomputers and massive parallel devices. Areas involved in experimental research started to consider this tool as an efficient way to handle problems considering the advantages and limitations in this field. It allows the explanation of some concepts hardly explained experimentally. Currently the development of computer hardware and that of quantum mechanical software allows a detailed description of molecular systems. There are on the other hand obvious limitations related to the accuracy for describing weak interactions (van der Waals) especially in complex biological material systems. Other limitations are related to the size of the molecule and the number of molecules involved in the system (up to 1000 atoms) compared to molecular dynamic (MD) and Ab initio MD simulations.

In this dissertation we have addressed two of the three main technical barriers needed to be overcome for the commercialization of low-temperature fuel cells; the electrocatalytic reactivity and the durability of the catalysts, but only indirectly we have examined the third barrier that is related to the high cost of some of the cell components. DFT calculations are used to analyze surface thermodynamic properties in order to get insights about the reactivity and stability of Pt and Pt alloys. The effect of the overall composition and atomic distribution over the electrocatalytic activity of the oxygen reduction reaction is studied. It must be noted that these calculations explore the not completely understood mechanism of the ORR using a solid – gas interphase instead of a real solid – electrolyte environment; however it is expected that important insights must follow qualitative agreement with a real environment under real operating conditions.

In terms of reactivity and stability we found that skin Pt monolayer surfaces are the most suitable catalysts for the ORR among the group of Pt-alloys in this study. Nevertheless these catalysts are not able to handle in the same efficient way than Pt the first electron and proton transfer due to less strong interaction between the OOH intermediate and the catalyst Pt, some of them can adsorb OOH with a reasonable strength close to that on Pt, that are the cases of skin Pt/Pd₃Pd and skin Pt/Pt₄Rh. On the other hand skin Pt monolayer catalysts have demonstrated good qualities to adsorb hydroxyl and atomic oxygen with a moderate strength in such a way that they can easily be reduced to water. Considering the overall reaction steps on the ORR, the electrocatalytic activity of all the studied skin Pt monolayer catalysts can be ordered as follow: Pt₃V (skin Pt) > Pt₃Co (skin Pt) > Pt₃Ni (skin Pt) > Pt > PtPd (skin) > Pt₄Rh (skin Pt) > PtPd₃ (skin). The d-population analysis indicates that the separation of the Pt skin monolayer with respect the catalyst substrate causes a rearrangement of the electronic density in the surface; the average electronic d-population on the surface is higher than that in the slab while the d-band correlation shows a clear correlation between the surface d-band center and the skin Pt monolayer catalysts; for these cases the d-band is shifted to negative energy values as a indication of their moderate interaction with all the ORR intermediates (hydroperoxo radical, hydroxyl, and atomic oxygen).

The dissolution of the catalyst in fuel cell operation plays an important role in the destabilization and the deactivation of the ORR. In this dissertation we have analyzed the stability of Pt, Co, Ni, Pd, and Rh on Pt, Pt₃Co, Pt₃Ni, Pt₃Pd, and Pt₄Rh and their respective Pt monolayer catalysts. We found that the order of stability of Pt, Co, Ni, Pd, and Rh atoms in Pt₃Co, Pt₄Rh, Pt₃Pd, and Pt₃Ni catalyst is: Pt > Co > Rh > Pd > Ni respectively. Similar trend is reported in literature for pure elements. It was also found that the stability of Pt atoms in skin Pt monolayer catalysts is favored by the presence of surface alloy metals in the following order: Rh > Co > Ni > Pd. Co, Ni, and especially Rh improves the stability of Pt atoms in the surface.

We also analyzed stepped surfaces to measure the reactivity in terms of adsorption energies. It was found that the strong OOH adsorption on the catalyst surface favors the first electron and proton transfer, however the strong interaction between the OH and O intermediates and the catalyst surface makes difficult the further reduction of these species to water. The strength of the ORR intermediates interactions was attributed to the reduced coordination on the catalyst surface.

As it was stated previously, the nature of the interphase of the systems in this study is solid-gas, and this should be improved to be able to approximate the behavior of them to a realistic solid-electrolyte interphase. It will obviously require future investigations. We would like to point out the necessity to incorporate in our simulations an additional component related to the presence of the electrolyte in the system. Although the formation of the OOH intermediate after the first electron and proton transfer indirectly involved the effect of the protonated acid medium and in the same way the hydrated protons are modeled as $\text{H}_3\text{O}^+(\text{H}_2\text{O})_3$ associating the effect of water molecules in the system for the characterization of the dissolution reactions, it would be important to address the effect of the degree of hydration of protons on the various steps of the reaction of oxygen molecules and their intermediates. In the same way the presence of the polymeric membranes such as Nafion, which is usually modeled as $\text{CF}_3\text{SO}_3\text{H}$, $\text{CH}_3\text{C}_6\text{H}_4\text{SO}_3\text{H}$ or $\text{CF}_3\text{OCF}_2\text{CF}_2\text{SO}_3\text{H}$ can affect the proton transfer due to the sulfonic acid functional groups^[124; 125]. Another interesting point to be considered is the electrode potential dependence of the reduction steps that can be manifested as changes in the activation barrier of the ORR reactions. This effect is not only associated to the ORR reactivity but also to the catalyst dissolution under potential cycling regimes. These contributions would help for a better understanding of a real system under normal operating conditions.

REFERENCES

- [1] V.S. Murthi, R.C. Urian, S. Mukerjee, *J. Phys. Chem. B* 108 (2004) 11011-11023.
- [2] V. Stamenkovic, T.J. Schmidt, P.N. Ross, N.M. Markovic, *J. Phys. Chem. B* 106 (2002) 11970-11979.
- [3] U.A. Paulus, A. Vokaun, G.G. Scherer, T.J. Schmidt, V. Stamenkovic, N.M. Markovic, P.N. Ross, *Electrochim. Acta* 47 (2002) 3787-3798.
- [4] U.A. Paulus, A. Vokaun, G.G. Scherer, T.J. Schmidt, V. Stamenkovic, V. Radmilovic, N.M. Markovic, P.N. Ross, *J. Phys. Chem. B* 106 (2002) 4181-4191.
- [5] S. Mukerjee, S. Srinivasan, M.P. Soriaga, *J. Phys. Chem.* 99 (1995) 4577 - 4589.
- [6] J.L. Fernandez, D.A. Walsh, A.J. Bard, *J. Am Chem. Soc.* 127 (2005) 357-365.
- [7] A. Winkler, X. Guo, H.R. Siddiqui, P.L. Hagans, *Surf. Sci.* 201 (1988) 419-443.
- [8] S. Mukerjee, S. Srinivasan, M.P. Soriaga, J. McBreen, *J. Electrochem. Soc.* 142 (1995) 1409.2, 104.
- [9] T. Toda, H. Igarashi, H. Uchida, M. Watanabe, *J. Electrochem. Soc.* 146 (1999) 3750-3756.
- [10] K. Sasaki, Y. Mo, J.X. Wang, M. Balasubramanian, F. Uribe, J. McBreen, R.R. Adzic, *Electrochimica Acta* 48 (2003) 3841-3849.
- [11] P.B. Balbuena, D. Altomare, L.A. Agapito, J.M. Seminario, *J. Phys. Chem. B* 107 (2003) 13671-13680.
- [12] Y. Wang, P.B. Balbuena, *J. Phys. Chem. B* 109 (2005) 18902-18906.
- [13] R.A. Sidik, A.B. Anderson, *J. Electroanal. Chem.* 528 (2002) 69-76.
- [14] G.S. Karlberg, *Phys. Rev. B* 74 (2006) 153414.
- [15] M.H. Shao, T. Huang, P. Liu, J. Zhang, K. Sasaki, M.B. Vukmirovic, R.R. Adzic, *Langmuir* 22 (2006) 10409-10415.
- [16] J. Zhang, Y. Mo, M.B. Vukmirovic, R. Klie, K. Sasaki, R.R. Adzic, *J. Phys. Chem. B* 108 (2004) 10955-10964.

- [17] T. Li, P.B. Balbuena, *Chem. Phys. Lett.* 367 (2003) 439.
- [18] Y. Xu, A.V. Ruban, M. Mavrikakis, *J. Am. Chem. Soc.* 126 (2004) 4717-4725.
- [19] V. Stamenkovic, T.J. Schmidt, P.N. Ross, N.M. Markovic, *J. Electroanal. Chem.* 554-555 (2003) 191-199.
- [20] M.H. Shao, K. Sasaki, R.R. Adzic, *J. Am. Chem. Soc.* 128 (2006) 3526-3527.
- [21] V.R. Stamenkovic, B. Fowler, B.S. Mun, G. Wang, P.N. Ross, C.A. Lucas, N.M. Markovic, *Science* 315 (2007) 493-497.
- [22] V.R. Stamenkovic, B.S. Mun, K.J. Mayrhofer, P.N. Ross, N.M. Markovic, *J. Am. Chem. Soc.* 128 (2006) 8813-8819.
- [23] V. Stamenkovic, T.J. Schmidt, P.N. Ross, N.M. Markovic, *J. Phys. Chem. B* 106 (2002) 11970-11979.
- [24] M.-H. Shao, K. Sasaki, R.R. Adzic, *J. Am. Chem. Soc.* 128 (2006) 3526-3527.
- [25] R. Adzic, in: *DOE Hydrogen and Fuel Cell Review Meeting*, Elsevier, Philadelphia, 2004, pp. 1-23.
- [26] J.L. Fernandez, D.A. Walsh, A.J. Bard, *J. Amer. Chem. Soc.* 127 (2005) 357-365.
- [27] M. Min, J. Cho, K. Cho, H. Kim, *Electrochimica Acta* 45 (2000) 4211 - 4217.
- [28] C.A. Lucas, N.M. Markovic, P.N. Ross, *Phys. Rev. B* 55 (1997) 7964-7971.
- [29] B. Beard, P.N. Ross, *J. Electrochem. Soc.* 137 (1990) 3368.
- [30] J.T. Glass, G.L. Cahen, G.E. Stoner, *J. Electrochem. Soc.* 134 (1987) 58.
- [31] S. Mukerjee, S. Srinivasan, *J. Electroanal. Chem.* 357 (1993) 201-224.
- [32] T. Toda, H. Igarashi, H. Uchida, M. Watanabe, *J. Electrochem. Soc.* 141 (1999) 968.
- [33] T. Toda, H. Igarashi, M. Watanabe, *J. Electroanal. Chem.* 460 (1999) 258-262.
- [34] V. Jalan, E.J. Taylor, *J. Electrochem. Soc.* 130 (1983) 2299-2302.
- [35] J. Appleby, *Energy* 11 (1986) 13.
- [36] S.J. Clouser, J.C. Huang, E. Yeager, *J. Appl. Electrochem.* 23 (1993) 597.
- [37] A.J. Bard, R. Parsons, J. Jordan, in: *Standard Potentials in Aqueous Solutions*, M. Dekker, New York, 1985, pp. 49.

- [38] A.J. Bard, Ed., in: *Encyclopedia of Electrochemistry of the Elements*, M. Dekker, New York, 1973, pp 155 - 233.
- [39] H. Yang, W. Vogel, C. Lamy, N. Alonso-Vante, *J. Phys. Chem. B* 108 (2004) 11024-11034.
- [40] M. Shao, P. Liu, J. Zhang, R. Adzic, *J. Phys. Chem. B* 111 (2007) 6772.
- [41] M. Watanabe, K. Tsurumi, T. Mizukami, T. Nakamura, P. Stonehart, *J. Electrochem. Soc.* 141 (1994) 2659.
- [42] H.R. Colon-Mercado, B.N. Popov, *Journal of Power Sources* 155 (2006) 253-263.
- [43] L.J. Wan, T. Moriyama, M. Ito, H. Uchida, M. Watanabe, *Chem. Commun.* (2002) 58-59.
- [44] R. Adzic, in: J. Lipkowski, P.N. Ross (Eds.), *Electrocatalysis*, Wiley VCH, New York, 1998, pp. 197-242.
- [45] E.B. Yeager, *Electrochim. Acta* 29 (1984) 1527-1537.
- [46] Y. Wang, P.B. Balbuena, *J. Phys. Chem. B* (2005) 14896-14907.
- [47] A. Damjanovic, D.B. Sepa, M.V. Vojnovic, *Electrochim. Acta* 24 (1979) 887-889.
- [48] R.A. Sidik, A.B. Anderson, *J. Electroanal. Chem.* 528 (2002) 69-76.
- [49] A.B. Anderson, T.V. Albu, *J. Electrochem. Soc.* 147 (2000) 4229-4238.
- [50] S.J. Paddison, *J. New Mater. Electrochem. Syst.* 4 (2001) 197.
- [51] S.J. Paddison, R. Paul, *Phys. Chem. Chem. Phys.* 4 (2002) 1158-1163.
- [52] M. Eikerling, S.J. Paddison, L.R. Pratt, T.A. Zawodzinski, *Chem. Phys. Lett.* 368 (2003) 108.
- [53] S. Tanimura, T. Matsuoka, *J. Polym. Sci., Part B* 42 (2004) 1905.
- [54] M. Tsuda, W.A. Diño, H. Kasai, *Solid State Commun.* 134 (2005) 601.
- [55] M. Tsuda, N.B. Arboleda, H. Kasai, *Chem. Phys.* 324 (2006) 393.
- [56] J.L. Gland, B.A. Sexton, G.B. Fisher, *Surf. Sci.* 95 (1980) 587.
- [57] A. Eichler, J. Hafner, *Phys. Rev. Lett.* 79 (1997) 4481.

- [58] S. Yotsuhashi, Y. Yamada, W.A. Diño, H. Nakanishi, H. Kasai, *Phys. Rev. B* 72 (2005) 033415.
- [59] Y. Wang, P. Balbuena, *J. Phys. Chem. B* 109 (2005) 18902-18906.
- [60] L.L. Wang, S.V. Khare, V. Chirita, D.D. Johnson, A.A. Rockett, A.I. Frenkel, N.H. Mack, R.G. Nuzzo, *J. Am. Chem. Soc.* 128 (2006) 131-142.
- [61] P.B. Balbuena, D. Altomare, L. Agapito, J.M. Seminario, *J. Phys. Chem. B* 107 (2003) 13671-13680.
- [62] B. T. Sutcliffe, in: G. H. F. Diercksen, B. T. Sutcliffe, and A. Veillard, (Eds), *Computational Techniques in Quantum Chemistry and Molecular Physics*, Springer, 1975, pp. 1.
- [63] D.B. Cook, *Handbook of Computational Quantum Chemistry*, Oxford University Press, Oxford, 1998.
- [64] I.N. Levine, *Quantum Chemistry*, Prentice Hall, New Jersey, 1983.
- [65] J.M. Thijssen, *Computational Physics*, Cambridge University Press, New York, 1999.
- [66] P. Hohenberg, W. Kohn, *Phys. Rev. B* 136 (1964) B864-871.
- [67] W. Kohn, L.J. Sham, *Phys. Rev. A* 140 (1965) 1133.
- [68] J.P. Perdew, K. Burke, M. Ernzerhof, *Phys. Rev. Lett.* 77 (1996) 3865.
- [69] R. Car, *Quant. Struct.-Act. Relat.* 21 (2002) 97-104.
- [70] D.R. Hamann, M. Schluter, C. Chiang, *Phys. Rev. Lett.* 43 (1979) 1494.
- [71] P. Blochl, *Phys. Rev. B* 50 (1994) 17953.
- [72] X. Gonze, F. Finocchi, *Physica Scripta T109* (2004) 40-47.
- [73] N.W. Ashcroft, N.D. Mermin, *Solid States*, Holt-Saunders, Philadelphia, 1976.
- [74] G. Kresse, J. Furthmuller, *Phys. Rev. B* 54 (1996) 11169-11186.
- [75] G. Kresse, J. Furthmuller, *Comput. Mater. Sci.* 6 (1996) 15-50.
- [76] G. Kresse, J. Hafner, *Phys. Rev. B: Condensed Matter and Materials Physics* 48 (1993) 13115-18.
- [77] G. Kresse, J. Hafner, *Phys. Rev. B: Condensed Matter and Materials Physics* 47 (1993) 558-61.

- [78] P.E. Blochl, Phys. Rev. B 50 (1994) 17953-17979.
- [79] J.D. Lawrence, H. Li, T.B. Rauchfuss, M. Benard, M.-M. Rohmer, *Angewandte Chemie, International Edition* 40 (2001) 1768-1771.
- [80] H.J. Monkhorst, J.D. Pack, Phys. Rev. B 13 (1976) 5188-5192.
- [81] M. Methfessel, A.T. Paxton, Phys. Rev. B 40 (1989) 3616-3621.
- [82] V. Kumar, Y. Kawasoe, Phys. Rev. Lett. 90 (2003) 055502.
- [83] G. Makov, M.C. Payne, Phys. Rev. B 51 (1995) 4014.
- [84] Neugebauer, Scheffler, Phys. Rev. B 46 (1992) 16967.
- [85] D. Balamurugan, R. Prasad, Phys. Rev. B 73 (2006) 235415.
- [86] M.J. Frisch, et al., Gaussian 03, Revision C.02 ed., Wallingford, CT, Gaussian, Inc., 2004.
- [87] A.J. Appleby, J. Electroanal. Chem. 357 (1993) 117-179.
- [88] B.E. Conway, in: *Modern Aspects of Electrochemistry*, J.O.M. Bockris and B.E. Conway (Eds.), Butterworth, London, 1964, pp. 43.
- [89] A. Kokalj, *Comp. Mat. Sci.* 28 (2003) 155-168.
- [90] A. Kokalj, *Journal of Mol. Grap. and Mod.* 17 (1999) 176-179.
- [91] G. Henkelman, B.P. Uberuaga, H. Jonsson, *J. Chem. Phys.* 113 (2000) 9901.
- [92] G. Henkelman, H. Jónsson, *J. Chem. Phys.* 113 (2000) 9978.
- [93] H. Jónsson, G. Mills, K.W. Jacobsen, in: *Classical and Quantum Dynamics in Condensed Phase Simulations*, (Eds.) B. J. Berne, G. Ciccotti and D. F. Coker, World Scientific Publishing, Singapore, 1998, pp. 385.
- [94] U.A. Paulus, A. Wokaun, G.G. Scherer, T.J. Schmidt, V. Stamenkovic, N.M. Markovic, P.N. Ross, *Electrochimica Acta* 47 (2002) 3787.
- [95] U.A. Paulus, A. Wokaun, G.G. Scherer, T.J. Schmidt, V. Stamenkovic, V. Radmilovic, N.M. Markovic, P.N. Ross, *J. Phys. Chem. B* 106 (2002) 4181-4191.
- [96] V. Stamenkovic, T.J. Schmidt, P.N. Ross, N.M. Markovic, *J. Electroanal. Chem.* 554-555 (2003) 191-199.

- [97] J.K. Norskov, J. Rossmeisl, A. Logadottir, L. Lindqvist, J.R. Kitchin, T. Bligaard, H. Jónsson, *J. Phys. Chem. B* 108 (2004) 17886-17892.
- [98] N.M. Markovic, P.N. Ross, *CATTECH* 4 (2000) 110.
- [99] G. Hoogers, D. Thompsett, *CATTECH* 3 (1999) 106.
- [100] S.R. Calvo, P.B. Balbuena, *Surf. Sci.* 601 (2007) 165-171.
- [101] D.R. Lide (Ed.) *Handbook of Chemistry and Physics*, Boca Raton, Florida, CRC Press, 1997.
- [102] C.T. Campbell, G. Ertl, H. Kuipers, J. Segner, *Surf. Sci.* 107 (1981) 220.
- [103] J.L. Gland, *Surf. Sci.* 93 (1980) 487-514.
- [104] A. Panchenko, M.T.M. Koper, T.E. Shubina, S.J. Mitchell, E. Roduner, *J. Electrochem. Soc.* 151 (2004) A2016-A2027.
- [105] A. Michaelides, P. Hu, *J. Am. Chem. Soc.* 123 (2001) 4235-4242.
- [106] H. Ye, R.M. Crooks, *J. Am. Chem. Soc.* 129 (2007) 3627-3633.
- [107] V. Stamenkovic, B.S. Mun, K.J.J. Mayrhofer, P.N. Ross, M.N. Markovic, J. Rossmeisel, J. Greeley, J.K. Norskov, *Angew. Chem. Int. Ed.* 45 (2006) 2897.
- [108] A.B. Ruban, H.L. Skriver, J.K. Norskov, *Phys. Rev. B* 59 (1998) 15990-16000.
- [109] A. Kootte, C. Haas, R.A.d. Groot, *J. Phys. Condens. Matter* 3 (1991) 1133.
- [110] R.W.G. Wyckoff, in: *Crystal Structures* (Eds.), Wiley, New York, 1963, pp.1.
- [111] A. Pachenco, M.T.M. Koper, T.E. Shubina, S.J. Michell, E. Roduner, *J. Electrochem. Soc.* 151 (2004) A2016-A-2027.
- [112] G.S. Karlberg, *Phys. Rev. B* 74 (2006) 153414.
- [113] C.T. Campbell, G. Ertl, H. Kuipers, J. Segner, *J. Surf. Sci.* 107 (1981) 120.
- [114] A. Kuzume, E. Herrero, J.M. Feliu, *J. Electroanal. Chem.* 599 (2007) 333-343.
- [115] Z. Gu, P.B. Balbuena, *J. Phys. Chem. A Letters* 110 (2006) 9783-9787.
- [116] F.A. Cotton, G. Wilkinson, C.A. Murillo, M. Bochmann, in: *Advance Inorganic Chemistry*, John Wiley & Sons, New York, 1999, pp.1044.
- [117] M. Lukaszewski, A. Czerwinski, *J. Electroanal. Chem.* 589 (2006) 38-45.
- [118] K. Juodkazis, J. Juodkazyte, B. Sebek, G. Stalnionis, A. Lukinskas, *Russian J. Electrochem.* 39 (2003) 954.

- [119] K. Juodkazis, G. Stalnionis, B. Sebek, V. Sukiene, I. Savickaja, *Russian J. Electrochem.* 38 (2002) 1157.
- [120] J. Greeley, J.K. Norskov, *Electrochimica Acta* 52 (2007) 5829-5836.
- [121] C. Kittel, in: *Introduction to Solid State Physics*, Wiley, New York, 1985, pp. 429.
- [122] M. Korling, J. Haglund, *Phys. Rev. B* 45 (1992) 13293.
- [123] T. Nautiyal, T.H. Rho, K.S. Kim, *Phys. Rev. B* 69 (2004) 193404.
- [124] T.D. Gierke, W.Y. Hsu, Eisenberg, A., Yeager, H. L., in: *Perfluoronated Ionomer Membranes* (Eds.) American Chemical Society, Washington DC, 1982, pp. 283-307.
- [125] K.-D. Kreuer, S.J. Paddison, E. Spohr, M. Schuster, *Chem. Rev.* 2004 104 (2004) 4637-4678.

VITA

Sergio Rafael Calvo was born in Lima, Peru, in March 1977. After finishing his high school studies he entered the Universidad Nacional de Ingenieria, where he received his bachelor's degree in Chemical Engineering in 1999. In 2000 he participated in an internship at Texas Petroleum Company (TEXACO) for a year and a half. In fall 2002 he started his Ph.D. program at the University of South Carolina and later transferred the summer of 2004 to Texas A&M University where he got his Ph.D. degree in Chemical Engineering in 2007. His dissertation focused on studying the reactivity and stability of Pt and Pt alloys catalysts toward oxygen reduction reaction.

Permanent address: JEB 620, 3122 TAMU, College Station, TX 77843.

Email address: sergio.r.calvo@gmail.com